Author:
Li, Yuan

Title:
Optimal Design Methodologies for Passive Vibration Suppression

Optimal Design Methodologies for Passive Vibration Suppression

Yuan Li

Department of Mechanical Engineering
University of Bristol

A dissertation submitted to the University of Bristol in accordance with the requirements for award of the degree of Doctor of Philosophy in the Faculty of Engineering.

October 2018

Word count: 51,000 (approx.)

Abstract

Suppression of undesirable vibrations is critical to ensure good dynamic performance of engineering structures. Vibration suppression problems can be categorised in terms of vibration behaviour, such as transient, self-excited or steady-state vibrations. Passive vibration suppression methods are widely adopted due to their inherent advantages, such as simplicity and reliability. Additionally, the introduction of the inerter has fundamentally expanded the achievable performance of passive vibration suppressors. Appropriate methodologies for the design of optimal passive vibration suppressors are needed to tackle particular problems.

This thesis develops systematic methodologies to design both configurations and physical arrangements of passive vibration suppression devices, solving a variety of vibration problems. Also, this work demonstrates the effectiveness of inerter-based devices in each case.

A transient vibration suppression problem is studied first, and considers stable shimmy oscillations in an aircraft main landing gear (MLG). Both frequency-domain and time-domain approaches are adopted with the frequency-domain method considered less effective since the system mode shapes vary significantly when certain devices are added. Several beneficial inerter-based configurations are identified with the proposed time-domain methodology.

A second example of a transient vibration problem includes an initial impact excitation; here the aircraft landing touch-down process. Following the approach established, beneficial shock strut configurations have been identified. However, it has been found that the amount of energy dissipated is unsatisfactory. To address this, an additional constraint on energy dissipation is considered, leading to an absorber with double-stage stiffness being proposed.

The instability of self-excited vibrations can be avoided with suitable vibration suppressors. To this end, a design methodology of selecting the device parameter values is proposed. The nonlinear MLG shimmy phenomenon is studied here. A bifurcation study is performed to investigate the effects of the shimmy-suppression devices on the MLG dynamics. It shows that the utilisation of a specific proposed spring-damper configuration results in improved robustness against varying aircraft operation conditions over a traditional shimmy damper. The benefits of two inerter-based configurations are also demonstrated by enhanced device robustness.

The steady-state vibration suppression of a hydraulic engine mount has also been analysed, and a design approach for determining the optimal physical device arrangement has been developed. It enables optimisations of all possible networks with predetermined number and types of fluid passageways, through which the fluid can pass between two chambers in the engine mount. To improve the performances over a wide range of frequencies, linear optimal designs are identified whilst the manufacturing limitations are also considered. Furthermore, optimal parametric design is conducted considering nonlinear behaviour in fluid passageways.

To my loving parents

Acknowledgements

I wish to take this opportunity to thank all the people who have helped and supported me immensely, to make my PhD journey so enjoyable and fruitful.

Firstly, I would like to express my sincere gratitude to my supervisor, Dr Jason Zheng Jiang who gave me the opportunity to study at the University of Bristol. Thanks for his continuous guidance, encouragement and faith to me, not only for my research work, but also for my personal life. I also want to thank my co-supervisor, Prof Simon Neild for his motivation, insightful suggestions and patience throughout my project. These work will not be possible without their valuable and continuous support.

I would also like to acknowledge the studentship awarded by China Scholarship Council, which gave me the opportunity to pursue my PhD at the University of Bristol.

The last four years at Bristol are unforgettable in my entire life. It has been my great honour to work with so many brilliant and lovely colleagues and friends in the ACTLab. Thanks to Prof David Stoten who welcomed me warmly when I first came to the lab and the daily coffee time. I extend my special thanks to my colleague and also my flatmate, Ying, for her academic discussions and the company from Carolina House to Bond Street. I also want to thank Xiaofu and Jiannan for their support and suggestions, good luck with your theses as well. Many thanks also to Tim, Hui, Yiyuan and Ming in the lab for their help and valuable discussions.

Last, but by no means least, my unmeasurable thanks to my parents who always trust and encourage me for my entire life, and also my friends in China. Love you and miss you! I would also like to thank my boyfriend, Kaiqiang, for his love, support and understanding to me, as well as his valuable suggestions for this thesis.

Author's declaration

I declare that the work in this dissertation was carried out in accordance with the requirements of the University's Regulations and Code of Practice for Research Degree Programmes and that it has not been submitted for any other academic award. Except where indicated by specific reference in the text, the work is the candidate's own work. Work done in collaboration with, or with the assistance of, others, is indicated as such. Any views expressed in the dissertation are those of the author.

SIGNED:

DATE:

Publications

Journal Publications

Y. Li, J. Z. Jiang, and S. A. Neild, "Inerter-based configurations for main-landing-gear shimmy suppression," *Journal of Aircraft*, vol. 54, no. 2, pp. 684–693, 2016.

Y. Li, J. Z. Jiang, S. A. Neild, and H. L. Wang, "Optimal inerter-based shock–strut configurations for landing-gear touchdown performance," *Journal of Aircraft*, vol. 54, no. 5, pp. 1–9, 2017.

Y. Li, C. Howcroft, S. A. Neild, and J. Z. Jiang, "Using continuation analysis to identify shimmy-suppression devices for an aircraft main landing gear," *Journal of Sound and Vibration*, vol. 408, pp. 234–251, 2017.

Conference Publications

Y. Li, J. Z. Jiang, and S. A. Neild, "Optimisation of shimmy-suppression device in an aircraft main landing gear," in 13th International Conference on Motion and Vibration Control, MOVIC 2016, *Journal of Physics: Conference Series*, vol. 744, no. 1, IOP Publishing, 2016.

Y. Li, J. Z. Jiang, P. Sartor, S. A. Neild, and H. L. Wang, "Including inerters in aircraft landing gear shock strut to improve the touch-down performance," in X International Conference on Structural Dynamics, EURODYN 2017, *Procedia Engineering*, vol. 199, pp. 1689–1694, 2017.

Contents

List of figures

List of figures

List of tables

Nomenclature

General notations

F	Applied force
Δv	Relative velocity between two terminals
b	Inertance
c	Damping
g	Gravitational constant
k	Stiffness
s	Laplace variable
ρ	Fluid density
ΔP	Pressure difference
Q	Flow rate
$Y(s)$	System immittance
t	Time variable
(X, Y, Z)	Global coordinate system
$\tilde{}$	Laplace domain variable
L	Mechanical network layout
C	Configuration which represent the optimised layout with optimised values
ρ	Mass density of the fluid

Chapter 2

A_1	Piston area of the fluid-based inerter
A_2	Channel cross-section area of the fluid-based inerter
C	Capacitance
i	Electrical current
l	Channel length of the fluid-based inerter
L	Inductance
R	Resistance
V	Electrical voltage

Chapter 3

c_ψ	MLG torsional-yaw damping
c_ϕ	MLG torsional-roll damping
d	Tyre deflection
e	Length of the mechanical trail bar
$f(z)$	Approximate mode shape for the first mode of the freely hanging MLG
f_η	First natural frequency of hanging MLG
F_y	Tyre lateral force
$F_y{}'$	Initial side force
I_{yb}	Polar moment of inertia of the wheels, axle and brake
I_ψ	Moment of inertia of the wheels, axle and brake assembly
$I_{\psi tot}$	Total torsional-yaw moment of inertia
k_v	Tyre vertical stiffness
k_ψ	MLG overall torsional-yaw structural stiffness
k_ϕ	MLG torsional-roll structural stiffness
l	Wheel distance
m_1	Unsprung mass
m_2	Main fitting mass
m_f	Modal mass for the lateral mode
M_z	Tyre self-aligning moment
r	Tyre loaded radius
R	Tyre unloaded radius
R_e	Effective radius of the tyre
t_{settle}	Settling time of the torsional-yaw motion
T_d	Equivalent torque generated by the shimmy-suppression device
T_ψ	Equivalent torque generated by torsional damping, torque link stiffnesses and shimmy-suppression device
v_1	Lateral displacement of the leading point of contact edge
V	Aircraft forward speed
y	MLG lateral displacement
y_a	Lateral deflection at the shock strut bottom point
$y_a{}'$	Lateral slope at the shock strut bottom point
α	Tyre slip angle
α'	Lateral deflection angle of the leading point of tyre-ground contact edge
δ	Roll stroke at the ground level

ε	Equivalent torsional motion of the shimmy-suppression device
ζ_{min}	The least damping ratio among all the modes
ζ_n	First relative damping coefficient for the lateral mode
η	MLG lateral modal DOF
σ	Tyre relaxation length
ϕ	MLG torsional-roll DOF
$\phi^{'}$	Roll deflection angle at the shock strut bottom point
ψ	MLG torsional-yaw DOF
ψ_{peak}	Peak amplitude of torsional-yaw motion
Ω	Angular velocity of the wheel

Chapter 4

A_a	Pneumatic area
A_d	Damping factor
A_h	Hydraulic area
A_n	Net orifice area
C_d	Orifice discharge coefficient
E_{pt}	The potential energy stored in the tyres
E_{ps}	The potential energy stored in the shock struts
F_a	Air spring force
F_h	Hydraulic damping force
F_t	Tyre force
F_s	Strut force along the strut axis
F_{smax}	The maximum strut load
k_s	Static stiffness
k_t	Linear tyre stiffness in vertical direction
L	Aerodynamic lifting force
M_1	The sum of the upper gear mass and the fuselage mass acting on the gear
M_2	Lower gear mass
n	Effective polytropic exponent
p_{a_0}	Initial strut air pressure
s_s	Deflection of the shock strut
s_{smax}	The maximum strut stroke
t_{end}	The end of the compression stroke
v_0	Initial air volume
V_0	Descent velocity
V_{end}	Aircraft vertical velocity at the end of touch-down process

W_d	The work done by the damper(s) of the strut
W_L	The work done by the lifting force
z_1	Vertical deflection of mass M_1
z_2	Vertical deflection of mass M_2
ΔE_k	Change of the kinetic energy
ΔE_p	Change of the potential energy
η_s	Shock-strut efficiency
ϕ	Rake angle of the strut

Chapter 5

a	Track width
c_d	Device damping
c_δ	Lateral damping of the strut
c_ψ	Torsional damping of the wheel assembly
e	Caster length
$\boldsymbol{F_X}$	Force vectors
h	Half of contact patch length
$J^b_{D\xi\xi}$	Moment of inertia at D with respect to ξ axis
$J^b_{D\eta\eta}$	Moment of inertia at D with respect to η axis
$J^b_{D\zeta\zeta}$	Moment of inertia at D with respect to ζ axis
$\boldsymbol{J_X}$	Moment of inertia matrix
k_d	Device stiffness
k_s	Additional stiffness of device
k_t	Tyre vertical stiffness
k_α	Tyre self-aligning coefficient
k_δ	Lateral stiffness of the strut
k_λ	Tyre restoring coefficient
k_ψ	Effective torsional stiffness of the torque links
l	Relaxation length
l_D	Distance from B to D
l_δ	Radius of lateral bending motion
m_D	Mass of the MLG bending part
M	Mass of the fuselage and the upper MLG
$\boldsymbol{M_X}$	Moment vectors

$\boldsymbol{r_X}$	Position vectors
R	Tyre unloaded radius
T_d	Torque generated by the shimmy-suppression device
T_ψ	Equivalent torque generated by torsional damping, torque link stiffnesses and shimmy-suppression device
$\boldsymbol{v_X}$	Vector vectors
V	Aircraft forward speed
z_B	Vertical displacement of point B
α_m	Maximum slip angle
δ	MLG lateral DOF
δ^*	Lateral bending motion
ε	Equivalent torsional motion of the shimmy-suppression device
λ	Tyre deflection
(ξ, η, ζ)	MLG body frame
ϕ	MLG rake angle
ψ	MLG torsional DOF
$\boldsymbol{\omega_X}$	Angular velocity vectors

Chapter 6

A_d	Effective decoupler area
A_i	Inertia track cross-section area
A_o	Effective orifice area
A_p	Effective piston area
c_r	Upper chamber damping
C_1	Upper chamber compliance
C_2	Lower chamber compliance
f	Excitation frequency
F_h	Force generated by fluid motion
F_T	Transmitted force
I_d	Fluid inertia in decoupler
I_i	Fluid inertia in inertia track
k_r	Upper chamber stiffness
K_{dyn}	Dynamic stiffness
L_i	Inertia track length
m_e	Engine mass
P_0	Pressure normalised constant

Q_d	Fluid flow rate through the decoupler
Q_i	Fluid flow rate through the inertia track
Q_o	Fluid flow rate through the orifice
Q_0	Flow normalised constant
R_d	Total fluid resistance in decoupler
$R_d^{'}$	Linear fluid resistance in decoupler
R_i	Fluid resistance in inertia track
R_0	Nonlinear resistance constant in decoupler
Re_{D1}	Pipe Reynolds number
T_d	Displacement transmissibility
V_d	Fluid flow volume through the decoupler
V_i	Fluid flow volume through the inertia track
x_e	High-frequency engine excitation
x_s	Low-frequency base excitation
X_d	Decoupler position
X_{dmax}	Half decoupler cage height
X_0	Decoupler position control constant
X_1	Decoupler switching function shape control constant
α_k	Variation of dynamic stiffness
δ_i	Variations of design parameters
μ	Fluid dynamic viscosity
ρ	Fluid density

Abbreviations

MLG	Main landing gear
DOF	Degree of freedom
LCO	Limit cycle oscillation
TMD	Tuned mass damper
TVMD	Tuned viscous mass damper
TID	Tuned inerter damper
TMDI	Tuned mass damper inerter

Chapter 1

Introduction

The problems of suppressing unwanted vibrations has attracted considerable attention across engineering fields such as aerospace, automotive and civil engineering. Due to the current drive for high-performance and lightweight structures, they become more flexible and potentially prone to vibrations. Therefore the design of satisfactory vibration suppression mechanisms is increasingly becoming an important task for engineers while the design requirements vary from application to application and are dependent upon the problem nature.

There are numerous vibration suppression problems and can be classified in terms of vibration behaviour, for example, transient, steady-state and self-excited vibrations. Transient vibrations caused by deterministic but aperiodic excitations are a typical type of vibration problems. Although such vibrations will die away after a period of time, the resulted damage to the structures, such as extreme loads due to large oscillation amplitude, will compromise the structure performance and operation life. One notable example of transient vibrations is that resulting from an initial impact, such as aircraft touch-down process. Effective suppression of landing impact will alleviate the damage to the aircraft frame and passenger/crew discomfort. Another typical problem is steady-state vibrations, which can lead to fatigue failure. It is critical to design suitable mechanisms with frequency-dependent behaviour to mitigate the steady-state vibrations over all operating regions. In addition, self-excited vibrations can occur in certain systems, such as shimmy of landing gear and aeroelastic flutter in aircraft wings. Periodic oscillations with bounded amplitudes, namely limit cycle oscillations (LCOs), are typically produced by self-excited systems. The onset and stability of such periodic oscillations are of practical importance with the need to protect the structures against dynamic instability. These three vibration suppression types are notable in engineering practice and can involve complex, sometimes conflicting design requirements. To design effective vibration

suppression mechanisms, appropriate optimum design methodologies must be adopted for dealing with different vibration problems.

A number of vibration suppression techniques have been adopted and the strategies can be divided into three categories: passive, active and semi-active. Extensive studies have shown that the active and semi-active methods can be superior to passive methods in terms of performance enhancement. However, passive methods are still widely used in engineering applications because they require no power input, hence are unconditional stable, low cost and have high durability. Structural modifications are the simplest passive way to mitigate vibrations but provide limited effectiveness. One of the most effective passive methods is to attach external vibration suppression devices to the primary structures, for example, using viscous damper or a tuned mass damper (TMD).

Whilst numerous efforts have been made in developing passive vibrations suppression, the devices are mainly designed based on conventional layouts or via a 'trail and error' approach. However, there are countless possible structures which have not been considered yet. Therefore, there is a need to establish a systematic optimum design methodology which can fully explore all possible passive structures. This can be constructed with electrical catalogue circuit designs which utilises network synthesis to devise the most effective circuits since 1950s. A comparison of the two has led to a newly-introduced passive mechanical element, the inerter.

The inerter was firstly proposed as a passive mechanical element in 2002 and completes the analogy between the mechanical and electrical systems. Before the introduction of inerter, the standard mechanical-electrical analogy mapped spring and damper to inductor and resistor, while mapping mass to grounded capacitor. This analogy has a shortcoming since the capacitor is a two-terminal element and so is not fully mapped to the mechanical domain. This shortcoming has been addressed by the mechanical inerter which possesses full analogous properties to a capacitor. With this all positive-real transfer functions can be realised by a passive mechanical network consisting of springs, dampers and inerters. Therefore, the range of dynamic behaviour achieved by linear passive absorbers, e.g. to enhance vibration suppression performance, can be fundamentally enlarged. The applications of inerters start in the field of automotive engineering, in designing a superior suspension strut, which has been used in Formula One racing. Performance advantages have also been identified for various engineering structures, such as on railway vehicles, motocycle, tall building and suspension bridge. The studies of exploring new applications of inerters and implementing inerters to real industry use are being developed recently.

Not limited to mechanical and electrical fields, the analogy can be extended to other systems, such as the hydraulics. Via the mechanical-electrical-hydraulic analogy, a unifying means to model and design both single-disciplinary and interdisciplinary systems, such as a rubber-hydraulic engine mount, is possible. This is of particular importance for forming a systematic approach to identify the optimum physical device arrangement.

This thesis aims to develop systematic optimal design methodologies for passive vibration suppression devices, in order to tackle different types of vibration problems. The design approaches will focus on two levels, one is to identify the ideal optimal configuration consisting of springs, dampers and inerters while the other one to look into the physical realisations of the device. These approaches will be developed using a series of case studies and are applicable to many other suppression problems. Using these case studies, this thesis also provides preliminary results of applying inerter-based vibration suppression methods to new application areas, such as to aircraft landing gear, and by doing so forming a basis for further academic and industrial exploration.

Chapter 2

Literature review and thesis outline

Suppressing unwanted vibrations is crucial to maintain and improve the performances of engineering systems, such as aerospace, automotive and civil structures. Currently, the increasing trend toward lighter and more flexible structures gives rise to more vibration issues. Hence, the need of enhancing the capability of vibration suppression systems is becoming more pressing.

Previous research efforts have been made on design of various vibration suppression systems for different applications. This section begins a review of several notable vibration suppression problems in terms of vibration behaviour and suppression techniques. Subsequently, we highlight inerter-based vibration suppression in the context of passive field. The research motivations and objectives of this thesis are then introduced and the thesis outline is presented.

2.1 Applications for vibration suppression

Vibrations in general are oscillatory motions of an object or a set of objects relative to a stationary frame of reference or an equilibrium point [9]. Vibration phenomenon occurs in a wide range of engineering structures and can be desirable and undesirable. It is of significance to reduce the undesirable vibrations since they may deteriorate the system operation performances, produce fatigue load and extremely lead to structure failure. Design of vibration suppression mechanisms depends on the performance requirements for specific applications, which are determined by the nature of the problems [10]. In this section, we explore three notable types of vibration behaviour subject to different excitations, along with typical examples corresponding to each type. This will be followed, in Section 2.2, by considering the types of vibration suppression methods available to limit such undesirable responses.

2.1.1 Transient vibrations

Transient responses are normally referred to the motion of a system which is suddenly disturbed by a deterministic but aperiodic excitation [11]. Such excitations may have short or long durations and the generated transient responses are expected to vanish after a period of time [12]. The transient vibrations are normally measured by time-domain technique. Different time-domain criteria can be proposed to measure such motion, including the peak vibration amplitude and decay rate. The overload caused by large amplitude of oscillations may damage the structure, or extremely lead to failure.

The motion generated by the initial shock or impact is one typical type of transient vibrations, for example, during aircraft touch-down. During this process, the loads of the landing impact will most be lessened through the landing gear dynamics to avoid damage to the airframe structure, passenger/crew discomfort, and also damage to the runway [13]. Mulwitzky *et al.* investigated the dynamics of a given aircraft landing gear with a conventional oleo-pneumatic shock absorber in [7]. The authors analysed the effects of various factors, such as nonlinear hydraulic orifice resistance and tyre characteristics, on landing behaviour. In addition, they concluded that with a large landing velocity, the impact may result in the tyre bottoming leading to damage to tyre and wheel rim. So for landing gear design complex requirements need to be satisfied, and Currey [14] and Young [15] gave a detailed presentation of these requirements. Numerical studies of analysing landing behaviour can also be found in [16–18]. Machine vibrations caused by impact loads, such as forge hammer, punching, start-up and shut-down processes, are also typically transient vibrations. It is important to design a reliable machine foundation to reduce such disturbance to the device and the surrounding environment [19]. Rather than an initial shock or impact, transient responses can also be excited by an initial perturbation, such as a sudden disturbance to one DOF to cause a non-zero initial state condition.

Apart from the short period of initial excitations, transient responses can also be triggered by a duration of inputs. A notable example is the motion of vehicles travelling over road irregularities such as bumps, hollows and speed humps etc. The resulting peak acceleration of vehicle body needs to be sufficiently reduced considering passenger discomfort [20]. Another example is the airfoil vibrations caused by sudden wind gusts and the resulting severe loading may cause passenger discomfort and structural damage to the aircraft [21]. The aircraft needs to satisfy the gust load design criterion, for example, withstand the 'worst-case' gust loads which is identified in time domain based on discrete gust profiles (one-cosine) [22].

2.1.2 Steady-state vibrations

There are numerous engineering structures which are prone to steady-state forced vibrations, leading to fatigue failure [23]. In order to ensure the durability and safety of the structure, suppressing steady-state vibrations has also attracted great research attention [24]. For steady-state motion, although it can be simulated with time-domain method, it may be time consuming if the system needs a long time to achieve the steady state. Then frequency-domain method is always employed to analyse steady-state motion, which transfers the responses from time domain to frequency domain (e.g. by the Fourier Transformation) and present the motion state with respect to frequency.

One typical example of steady-state forced vibrations is that induced by internal forcing, such as in combustion engines [25]. In [26], the authors summarised two typical types of engine disturbances, including the firing pulse and engine inertia force and torque. These internal excitations are periodic [25] and generally refer to two specific types of inputs over different frequency ranges. For modern passenger vehicles, the design and implementation of engine mounting system is vital to improve the performance in terms of ride comfort, vibration isolation and noise reduction. Due to the strong trend toward lighter and more flexible car bodies and the fuel efficiency requirement, engines that are smaller and lighter but do not compromise its power are required, as stated in [27]. This gives rise to more vibration and noise issues so enhancing the capability of engine mounts becomes even more important.

Base excitation, such as harmonic uneven road inputs, is also a source of disturbances generating steady-state forced vibrations. Many research studies have dealt with the vehicle vibrations induced by harmonic road profile, see [28] as an example. Another typical type of steady-state responses are excited by periodic external forcing. For example, Van der Tempel [29] analysed the fatigue damage of a monopile offshore wind turbine due to regular wave loading. The support structure needs to be carefully designed to withstand such loading.

2.1.3 Self-excited vibrations

In Sections 2.1.1 and 2.1.2, the transient and steady-state vibrations are explored, along with some typical examples. Self-excited oscillations are regarded as a special class of vibrations frequently occurred in a broad class of engineering structures, also known as self-oscillations or self-sustained oscillations. As introduced by Den Hartog [25], the self-excited systems are sustained by the *alternating force* or *feedback mechanism* which is dependent on the system motion (displacement, velocity or acceleration) and will

disappear once the motion cease. Den Hartog also presented that for a linear system, the self-excited vibrations can be described as free vibrations with negative damping. In contrast with the conventional positive damping, the negative damping amplifies the vibration amplitude without any bound. For a nonlinear dissipative system, the equilibrium between the input and dissipated energy will produce periodic oscillations with bounded amplitudes, which typically results in a LCO [30]. The local stability of LCOs, which depends on the interaction between the input and dissipated energy, is of significance for self-excited vibration analysis and suppression. For example, the stability of LCOs determines the extent to which the structures are damaged: catastrophic failure can be caused by unstable LCOs and structural fatigue by stable LCOs [31]. Quasi-periodic oscillations are also treated as a typical type of self-excited oscillations, which corresponds to limit torus surface in the phase plane [32].

Wing flutter is one typical example of self-excited vibrations in aerospace systems. When this phenomenon occurs, the wings experience excessive oscillations, which may lead to fatigue or catastrophic failure of the structure [31]. The source energy feeding into the system is from the air flow over the wing surface and is transferred to vibration modes [25]. In the classical linear flutter analysis, the flutter instability boundary is identified using eigenvalue analysis [33]. Above this boundary, the system becomes unstable and the amplitude increases exponentially with respect to time. In [34], Dowell presented that aeroelastic systems experience inherent nonlinearities, from both structural and aerodynamic mechanisms, such as freeplay and shock wave motion. The associated nonlinearities affect the flutter boundary but also result in LCOs, i.e., the response is bounded due to the presence of the nonlinearities. The nonlinear structural effects on wing flutter were investigated firstly by Woolston *et al.* in [35]. Numerical research efforts have been made to identify the nonlinear flutter speed, analyse the stability and predict the amplitudes of LCOs, see [36, 37] as examples. Outside the aerospace systems, the flutter phenomenon is also noticed in other structures; for example in suspension bridges [38], turbo machines [39] and flexible pipes [40].

Another notable example of self-excited vibrations is wheel shimmy. The earliest work on shimmy phenomenon was conducted on automotive industry by Broulhiet [41] who included the tyre dynamics in shimmy analysis. He also argued that the energy source is the forward kinetic energy and the self-excited mechanism is caused by the energy transfer from the lateral tyre-ground contact force to the vibration modes of the structures. The similarities between shimmy in cars and aircraft were observed by Fromm [42], who investigated shimmy analysis in the aerospace field. Aircraft landing gear shimmy may take place during take-off, landing or taxiing, leading to undesirable discomfort and annoyance to crew and passengers or even catastrophic failure of the gear and/or the

attachment structure [43]. Even though shimmy oscillations are more oftenly observed on nose landing gears [44], the main landing gears (MLGs) of some types of aircraft, such as Douglas DC-9, Fokker 28, BAC 1-11 and Boeing 737, still suffered from shimmy oscillations [13]. Examples of shimmy events in MLGs can also be found in [43, 6].

Machining chatter, an instability during the machine cutting process, is also regarded as a common type of self-excited oscillations [45]. Initially triggered by cutting forces, chatter vibrations may lead to excessive vibrations of the workpiece and tool. Consequently, this will deteriorate the product surface finish, reduce the machine's service life and operation reliability and safety [46]. The most common type of machining chatter is regenerative chatter, which was firstly analysed by Tobias [47] and Tlusty [48] in the late 1950s. The method of producing stability lobes to predict the free cutting depth and speed was firstly presented in [47] and still widely accepted in this field. A review of other types of chatter, such as frictional chatter, and the research about predicting, analysing and controlling chatter is given by Quintana *et al.* [49].

2.2 Vibration suppression methods

Several suppression strategies, which are broadly classified into three types: passive, active and semi-active, have been proposed and employed for vibration suppression. Each technique has a reasonable range of applications. Rather than to provide a comprehensive review, this section will present a brief introduction of these techniques, along with some notable applications.

2.2.1 Passive vibration suppression

The simplest passive way to suppress vibrations is structural modifications, such as choosing proper structure mass, stiffness and damping [10]. However, the effectiveness of structural modifications are often limited because complex performance criteria can not be all satisfied and practical constraints of structure parameters need to be considered. A common alternative approach is to add passive vibration suppression devices, such as absorbers or isolators, to the primary oscillatory structures.

A common device is the resonant absorber. An undamped resonant absorber was firstly introduced by Frahm [50] as a spring-mass system. The essential function of this device is to avoid resonance vibrations of the primary system, via tuning the frequency of the device to match that of the primary resonance frequency of the main structure. Detailed theoretical study of tuned resonant absorbers was attributed to Den Hartog, who

introduced damping to resonant absorber to give the TMD, and provided an analytical optimum design criterion, see [25]. TMDs have been successfully proposed for structural vibration suppression in civil engineering, such as buildings [51, 52] and chimneys [53]. A review of these civil engineering applications is given in [54].

Another notable type of passive vibration suppression devices is a parallel spring-damper system, such as suspension system for road vehicle and shock absorber of aircraft landing gear. For example, for aircraft system, the shock absorber unit is often regarded as the critical component in the aircraft landing gear [55]. Among all the design operation conditions, such as landing and taxiing, the landing touch-down case determines the greatest energy dissipation requirement for the shock absorber and governs its general performance accordingly [56]. At present, most aircraft uses a passive oleo-pneumatic shock absorber due to its high strut efficiency compared to other shock absorbers, alongside considerable energy dissipation ability and good rebound control [14]. A conventional shimmy damper [6] also has a parallel spring-damper arrangement and has shown its effectiveness in stabilising shimmy-prone gears [6].

A conventional hydraulic engine mount is also regarded as a passive vibration suppression device. Typically two fluid channels, the inertia track and the decoupler, are configured between the upper and lower chambers and govern the dynamic behaviour under low-frequency and high-frequency excitations, respectively. Work on optimum tuning of a passive engine mount has been progressed [57–59]. For example, Ahn *et al.* [58] reported the work to improve the mount transmissibility, i.e., to deepen the notch and shorten the peak height of mount dynamic stiffness, optimising over the rubber stiffness, piston area, fluid inertia, volumetric stiffness and damping. However, most efforts on designing interior fluid passageways in a mount were via a 'trial and error' approach. The improvement is limited due to the fact that there are countless possible designs that have not been covered by these studies.

2.2.2 Active vibration suppression

Active method is also a popular way to suppress vibrations, with significant research starting in the 1970s. Different from passive suppression technique, active method reduces vibrations using an active force in the form of an actuator. Such system requires an added power supply to the system to generate a motion, rather than absorbing power to resist a motion as does the case in passive devices. These active forces will vary with respect to the current states of the system, which are normally measured by sensors, and are designed to operate for a wide range of excitation and operation conditions. A control law is used to determine the appropriate actuator force based on sensor signals.

If control laws are carefully designed, such a system outperforms passive devices, see [60] as an example comparison using a multi-storey building model. However, more expensive hardware and power requirements lead to a high cost. In addition, active vibration suppression carries a risk of instability due to the injection of activation power [10]. Therefore, active vibration suppression techniques are often avoided if possible in most industrial applications [61].

Active suspension system designs have drawn great attention in recent years with numerous demonstrations of their performance superiority over passive systems in different applications. For example, active control methods have also been proposed for aircraft shock absorbers. Theoretical analysis and experimental validations have been carried out to investigate the advantages of the actively controlled landing gears, such as in [62, 63]. Active methods are also employed to sustain the system stability. For example, studies have proposed active shimmy-suppression strategies, such as using fuzzy adaptive control [64] and sliding mode control [65]. To suppress steady-state vibrations, for example, in combustion engines, active engine mounts have also been proposed, see [66] as an example.

2.2.3 Semi-active vibration suppression

An alternative to passive and active suppression techniques is semi-active suppression, which combine some of the features of both passive and active ones. Basically semi-active techniques incorporate adjustable passive devices which incorporate the tunable parameters that are dependent on system motion [61]. Generally semi-active suppression systems only require a low level of external power. They does not generate a motion, but resist a motion as passive devices hence facilitate the system stability [67].

The study of semi-active vibration suppression was firstly carried out by Karnopp *et al.* in [68], which proposed a 'skyhook' damper system for automotive suspension systems and similar performance advantages were achieved as fully active systems. After [68], many research efforts have been made on semi-active suppression for engineering applications. For example, Krüger [69] investigated a semi-active landing gear to improve passenger ride quality during taxiing and landing with the consideration of rough runway models. Choi *et al.* [70] analysed the feasibility and effectiveness of smart fluids, electrorheological and magnetorheological fluids, in landing gear systems to attenuate the landing load to aircraft and vibration due to landing impact. In [71], the superiority of semi-active magnetorheological dampers on suppressing landing gear shimmy instability was demonstrated, when compared with a conventional passive shimmy damper. It is also potentially advantageous to adjust the interior design of suppression device using

semi-active ways; for example, controllable cross-section area [72] and length [73] of inertia track of hydraulic engine mount are achieved via semi-active means, as well as improved performance.

In summary, although active or semi-active vibration suppressions outperform passive ones in terms of performance enhancement, passive devices do have some advantages. They are typically simpler, more reliable, requiring no power source, and are unconditionally stable. For example, active systems require build-up power generation, however, under some circumstance such as earthquake, the device is needed while the power often fails. Hence, this thesis will focus on passive devices.

Generally, conventional passive devices are normally identified via a 'trail and error' approach hence their dynamic performance is not maximised. This is due to lack of symmetric approach to fully explore all possible designs. This can be potentially addressed with the help of a newly-introduced passive mechanical element, named 'inerter', as discussed in Section 2.3.

2.3 Passive inerter-based vibration suppression

The inerter is a commercially-available component, firstly introduced by Smith [74]. Recently, significant performance advantages of passive inerter-based vibration suppression have been successfully identified for multiple engineering structures. In this section, the concept and physical realisations of inerter are reviewed, along with a mechanical-electrical-hydraulic analogy. We also explore three available design approaches for passive vibration absorbers and a number of notable example applications.

2.3.1 The inerter

The Concept

The inerter was firstly proposed as a passive mechanical circuit element by Smith [74], to achieve a complete analogy between mechanical and electrical systems. The standard mechanical-electrical force-current analogy introduced by Firestone [75], and sets the mechanical force F analogous to electrical current i and mechanical velocity difference Δv to electrical voltage V. With the force-current analogy, the electrical inductor and resistor can be mapped to the mechanical spring and damper, respectively. Since the mass must have one terminal fixed to earth [75] due to the applied Newton's second law,

it is analogous to the capacitor with one terminal as electrical ground. This analogy is obviously incomplete as the capacitor is not necessarily to have a grounded terminal.

Given the ideal property of a capacitor that the current through the element is proportional to the derivative of voltage, it can be expressed as

$$i = C\dot{V}, \tag{2.1}$$

where C is capacitance. Equivalent to a capacitor, the proposed inerter, which is a two-terminal device and neither terminal needs to be grounded, has the property that the reaction force is proportional to the relative acceleration between its terminals. The property of an ideal inerter can be expressed as

$$F = b(\dot{v}_1 - \dot{v}_2), \tag{2.2}$$

where b is called 'inertance' and has the unit as mass, $(\dot{v}_1 - \dot{v}_2)$ is the relative accelerations. Thus the electrical circuits will be directly analogous to mechanical elements, which are typically springs, dampers and inerters for vibration suppression field, details as given in Section 2.3.2.

In [74], Smith proposed four conditions to be satisfied as a useful inerter , which are, namely, that the device should have a small mass without reference to the required inertance and there is no need to have a grounded terminal, should have a designable but limited size, and be able to work regardless of the spatial orientation and motion. These conditions also work for spring and damper elements. Built on these, more mechanical networks consisting of springs, dampers and inerters are achievable, and more importantly any one-port mechanical positive-real impedances can be synthesised passively using the classical electrical network synthesis theory [74]. For the purpose of vibration suppression, a wide range of passive structures with enhancing vibration suppression performance can be realised by mechanical networks.

Physical realisations

Inerter realisations can be classified into two typical types: flywheel-based and fluid-based.

Flywheel-based inerter mainly refer to rack-and-pinion [74, 1] and ball-screw inerters [1], both of which satisfy all the four conditions Smith proposed in [74] and are illustrated schematically in Figs. 2.1 (a) and (b), respectively. For the rack-and-pinion inerter, a sufficiently large inertance comparing with the device mass is realisable by adjusting the gear ratios or introducing extra gearing. Investigations have been made to model

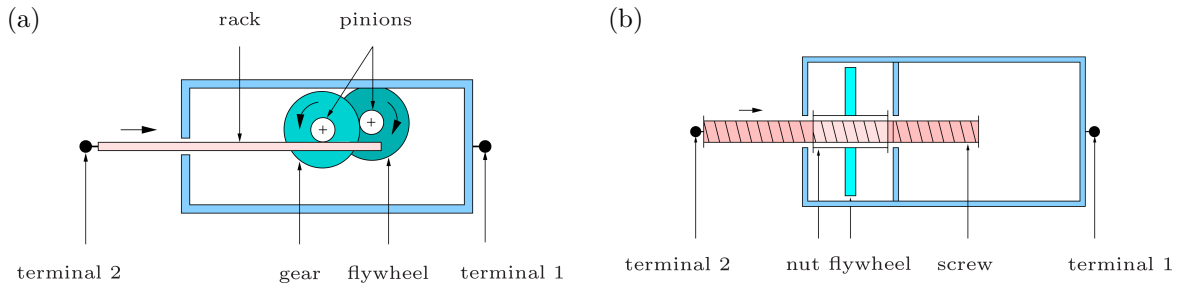

Fig. 2.1 Schematic views of (a) rack-and-pinion inerter; (b) ball-screw inerter. The figures are reproduced from [1].

the dynamics of rack-and-pinion inerter and the effects of nonlinearities, such as the backlash in the device and friction [1, 76]. Due to these effects, deficiencies inevitably exist, including the excessive wear of the gear mechanism caused by high friction and the phase lag due to the backlash [77]. To overcome these issues, the ball-screw inerter was proposed and currently commercially-available. The inertance is determined by the ratio between the flywheel inertia and the pitch of the screw. For example, Gonzalez-Buelga *et al.* reported a commercially available ball-screw inerter, which weighs 2 kg and has 75 kg of inertance [78]. The experimental testing of ball-screw inerter [79] demonstrated that the backlash can be eliminated in the ball-screw device due to the preloading in the manufacturing process, while the friction and elastic effects of the gear still influence significantly the ideal inerter properties, see [1, 79]. Therefore, for both rack-and-pinion and ball-screw devices, excessive wear of the mechanisms may not be avoided after certain number of operation cycles and to maintain the precise functions, high manufacture and maintenance cost is required. The industrial applications of inerter-based vibration absorbers incorporating flywheel-based inerter realisations are limited [2].

Fluid-based inerter has been shown as an attractive alternative of a flywheel-based one, using low-cost, more durable and simple designs [2, 80, 81]. From the application point of view, it is also beneficial because the damping effects are easily to be integrated via incorporating flow restrictions. For the hydraulic inerter proposed in [80], the device consists of a hydraulic cylinder, a piston with a shaft configured inside the cylinder and a hydraulic motor connected to the cylinder with pipes. The piston separates the cylinder into two parts, one of which is connected to the inlet or outlet of the hydraulic motor. During operation, the translational motion of the piston pushes the fluid in the cylinder and generates the pressure difference between the the inlet and outlet of the hydraulic motor. Such pressure difference will push the fluid flowing through the motor to generate an inertia force. The dynamics and model of such inerter were also verified experimentally in [80]. Different from the fluid-based inerter proposed in [80],

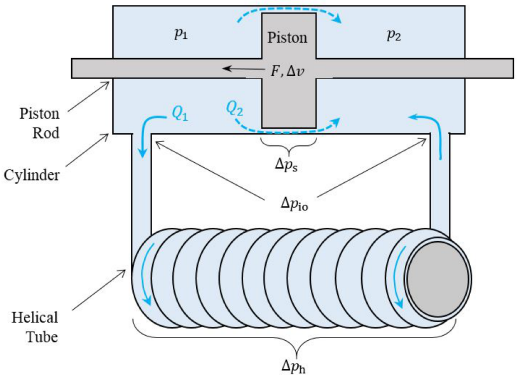

Fig. 2.2 Schematic view of a typical helical-tube fluid-based inerter, reproduced from [2].

of which the inertance makes use of hydraulic motor inertia, the helical-tube inerter introduced in [2, 81] provides the inertia in terms of the fluid itself. As illustrated in Fig. 2.2 [2], in operation, the piston rod moves to push the working fluid and the mass of fluid flowing through the channel gives rise to an inertia force. The device inertance can be approximately calculated by

$$b = \rho l \frac{A_1^2}{A_2}, \tag{2.3}$$

where ρ is the fluid density, l is the channel length, and A_1 and A_2 are the piston area and the channel cross-section area, respectively. The inherent damping encountered in the device is studied and modelled in [2, 81] and in particular [2] proposed a lumped parameter hydraulic model in both hydraulic and mechanical domains, which considered the damping, inertance and stiffness effects.

Except the aforementioned inerter realisations which always incorporate a translational travel, rotational inerter which is ideal for torsional vibration suppression is also proposed. A planetary-gear inerter [82] is a typical example and during the operation the relative rotation between two terminals drives the rotations of both the sun and planetary gears, generating the inertia force.

2.3.2 A mechanical-electrical-hydraulic analogy

An analogy between the electrical and other systems, such as mechanical, hydraulic, acoustic and thermal systems, allows the well-developed circuit theory in electrical field to be applied directly to the other fields [75]. There are several analogies between mechanical and electrical systems, among which the force-current analogy is more practically useful and widely accepted comparing with others. This analogy is based on the concepts of *through-* and *across-variables* to achieve a perfect correspondence of connection types

	Electrical	Mechanical	Hydraulic
$Y(s)$	$\frac{\widetilde{i}}{\widetilde{V}} = \frac{\widetilde{i}}{\widetilde{U_1}-\widetilde{U_2}}$	$\frac{\widetilde{F}}{\widetilde{\Delta v}} = \frac{\widetilde{F}}{\widetilde{v_1}-\widetilde{v_2}}$	$\frac{\widetilde{\Delta P}}{\widetilde{Q}} = \frac{\widetilde{P_1}-\widetilde{P_2}}{\widetilde{Q}}$
Basic elements	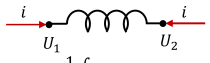 Inductor $i = \frac{1}{L}\int (U_1 - U_2)dt$ $Y(s) = \frac{1}{Ls}$	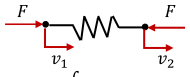 Spring $F = k\int (v_1 - v_2)dt$ $Y(s) = \frac{k}{s}$	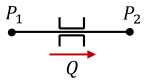 Compliance $P_1 - P_2 = \frac{1}{C}\int Q dt$ $Y(s) = \frac{1}{Cs}$
	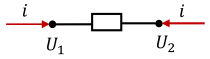 Resistor $i = \frac{1}{R}(U_1 - U_2)$ $Y(s) = \frac{1}{R}$	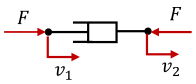 Damper $F = c(v_1 - v_2)$ $Y(s) = c$	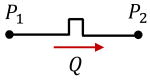 Resistor $P_1 - P_2 = RQ$ $Y(s) = \frac{1}{R}$
	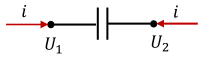 Capacitor $i = C\frac{d(U_1 - U_2)}{dt}$ $Y(s) = Cs$	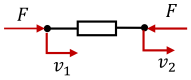 Inerter $F = b\frac{d(v_1 - v_2)}{dt}$ $Y(s) = bs$	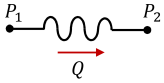 Inertance $P_1 - P_2 = M\frac{dQ}{dt}$ $Y(s) = Ms$

Fig. 2.3 A mechanical-electrical-hydraulic analogy. The notation ~ represents the variable in Laplace domain.

(series or parallel). A through-variable is, by definition, one that has the same value at both terminals of the element, and an across-variable represents the relative property across the element [83]. Force (or torque) and current are regarded as through-variables, and velocity (translational or angular) difference and voltage as across-variables for mechanical and electrical systems, respectively [75].

Apart from mechanical, electrical or the combined devices, hydraulic vibration suppression devices are also commonly employed into various mechanical structures, such as rubber-hydraulic engine mounts [84] and bushings [85]. Such hydraulic vibration suppression device typically incorporates one (equivalent) piston mechanism, of which the pressure difference ΔP within the device will balance the mechanical force F and the relative velocity Δv is proportional to the flow rate Q. This allows the translation from hydraulic to mechanical domains.

Fig. 2.3 summarises the force-current mechanical-electrical analogy and the translation from hydraulic impedances to mechanical ones for basic elements. Via the mechanical-electrical-hydraulic analogy, a linear physical system can be represented by a network as an electrical circuit then the electrical network analysis and synthesis can be applied to explore the dynamic characteristics systematically. Furthermore, it provides a unifying means to model and analyse an interdisciplinary system, such as a rubber-hydraulic engine mount system [84] or a mechatronic device [86]. Modelling of the fluid-based

inerter also takes advantages of such an analogy [2]. A review of employing network analysis and synthesis to passive vibration absorber design is given in Section 2.3.3.

2.3.3 Passive vibration absorber design approaches

In Section 2.3.1, it was shown that the introduction of inerter completes the mechanical-electrical-hydraulic analogy. Consequently, the range of passive vibration absorbers, which can be realised by passive networks, is fundamentally enlarged to provide enhanced dynamic performances. To identify the beneficial passive vibration absorber configurations depends on the way the candidate layouts are proposed and optimal parameter tuning is carried out via either analytical analysis or optimisation algorithms. Note that here the term *configuration* represents the network topological arrangement (layout) of components that are ideal passive springs, dampers and inerters, as well as their parameter values. Two approaches, which are *structure-based* and *immittance-based*, are commonly used to design the optimal passive vibration absorber configurations. A notable design approach, namely *structure-immitance based* approach, is newly introduced in [87]. This section provides an overview of these three approaches. Note that optimisation algorithms themselves are not discussed here as standard optimisation techniques are applied here.

Structure-based approach

With the structure-based approach, candidate passive networks are proposed using predetermined components with fixed network topology. Element values of the candidate layouts are selected through the optimisation, using the performance criteria as the cost function and considering sensible element constraints .

A number of passive vibration absorber layouts, which manifest their benefits for different applications, can be proposed as structure-based candidates. For example, before the introduction of inerter, passive vibration absorber normally consists of spring, damper and mass elements, such as TMD for building suspension. Alternatively, beneficial inerter-based vibration absorbers are proposed with structure-based approach for building suspensions. In [3], three structures were investigated, which are the parallel spring-damper, parallel spring-damper-inerter and a spring in parallel with a series damper-inerter layouts (the latter two are illustrated in Figs. 2.4 (a) and (b)). Tuned viscous mass damper (TVMD), which incorporates an inertia-like component, was proposed and analysed for building seismic vibration control by Ikago *et al.* [4]. A new configuration in which the mass of TMD is replaced by inerter was introduced by Lazar *et al.* [5], named as tuned inerter damper (TID). Schematic views of TVMD and TID layouts are

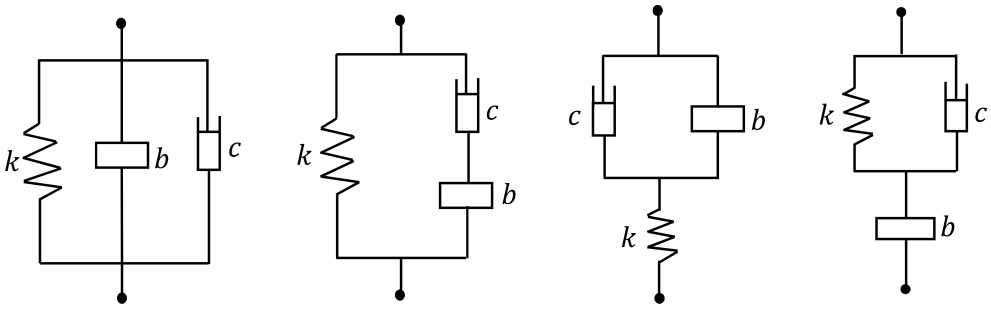

Fig. 2.4 Schematic views of four typical inerter-based vibration absorbers, (a) parallel spring-damper-inerter layout [3], (b) a spring in parallel with a series damper-inerter layout [3], (c) TVMD [4], (d) TID [5].

illustrated in Figs. 2.4 (c) and (d). All these proposed devices function as suspension systems, which have two terminals connected to two points on the structures. The applications of the aforementioned layouts are introduced in detail in Section 2.3.4.

The structure-based approach allows an investigation of the potential performance advantages of layouts with the lowest complexity, with the additional benefits of setting parameter constraints to components directly. This is crucial in terms of weight and space limit, manufacture and cost. However, the achieved improvement is limited due to the fact that there are many possible designs that have not been covered by this approach. In contrast, the immittance-based approach can systematically consider more complex mechanical structures with a wide range of possibilities.

Immittance-based approach

The immittance-based approach is associated with network synthesis of positive-real system immittance (or impedance) $Y(s)$, which can be defined as

$$Y(s) = \frac{\widetilde{F}}{\widetilde{\Delta v}}, \tag{2.4}$$

where $\widetilde{F}$ and $\widetilde{\Delta v}$ represent the force and the relative velocity in the Laplace domain, respectively. The expressions of $Y(s)$ for basic components are summarised in Fig. 2.3. To be specific, a positive-real $Y(s)$ will be employed and then its parameters be optimised to achieve the optimum performances. Then network synthesis theory can then be used to identify the specific layout which can realise the optimised $Y(s)$ [88, 89].

In the context of electrical network synthesis, Bott and Duffin [90] introduced a theorem that any positive-real immittance function can be realised by a network layout only consisting of inductors, resistors and capacitors. With the analogy introduced in Section 2.3.2, this theorem can be extended to other contexts, such as mechanical and hydraulic systems. To ensure relatively less complexity, the immittance $Y(s)$ can be set to be a bilinear or biquadratic function, in which the numerator and denominator are first-order or second-order functions of the Laplace variable, respectively. The benefits of using such transfer functions have been identified for various mechanical structures, such as automotive [86], motorcycle [91] and building [92]. Higher-order immittance functions are also investigated using linear matrix inequality approaches for vehicle suspension in [93, 94] and has been shown to be more beneficial than bilinear and biquadratic functions. For vibration absorbers of mechanical structures, minimising network complexity is crucial due to space and weight limit, so minimal realisations of the optimal immittance functions draw the researchers' attention. A series of network synthesis results have recently been obtained on efficient realisations of the positive-real biquadratic impedances [95–97], for example, by networks consisting of three resistive and two reactive elements [95].

A wide range of positive-real immittance functions are allowed to be explored using the immittance-based approach. However, in this approach, it is not possible to predetermine the number and types of elements and the network topology. There are still some positive-real immittances which need to be realised with a large number of elements, such as nine elements for biquadratic functions with Bott-Duffin realisations [90]. Considering the difficulty of manufacture and space and weight limit, the network with a large number of elements or complex topology is not preferable. Also regarding such physical considerations, another drawback of immittance-based approach, comparing with structure-based one, is that the element values can not be restricted in advance.

Structure-immittance approach

As previously discussed, both the commonly-used design approaches for passive vibration absorbers, structure-based and immittance-based, have their own advantages and inherent disadvantages. To retain the advantages associated with both approaches while avoid their limitations, a newly-introduced design approach, namely, the structure-immittance approach was proposed in [87]. The transfer functions proposed by this approach not only cover all networks with a predetermined number of each element but also contain explicit information of network topology and element values. Based on the series-parallel

network theory, a general procedure to formulate the structural immittance with any arbitrary number and type of elements is introduced, see [87] in detail.

In [87], two case studies regarding vibration suppression for vehicle and building structures are carried out to demonstrate the feasibility of this approach. Considering the structures with specified complexity in terms of the numbers of each element used, optimisation results with this approach outperform the ones obtained with structure and immittance based approaches. The applicability of such technique is not limited to the context of mechanical device while can be extended to hydraulic, electrical or the compound systems.

2.3.4 Inerter applications

In [74], Smith introduced three initial ideas for inerter applications, to function as an enhanced vibration absorber, help design a superior suspension strut and replace a mass element. These ideas have been developed and extended to a wide range of engineering structures by extensive studies, with identified significant performance improvements.

Vehicle systems

The inerter, codenamed the 'J-damper', was initially applied for the suspension of Formula One racing by McLaren Mercedes since 2005, where a parallel spring-damper-inerter layout, as illustrated in Fig. 2.4 (a), is used [98] to retain a better handling and grip. McLaren invented the name of 'J-damper' for the inerter to protect the technology from its rivals, while until 2008, the secret was disclosed and the inerter was becoming commercially available [99].

Although the advantages of the 'J-damper' on Formula One were hidden, studies of inerter-based suspension for road vehicle are still developed in the open literature. In [100], Smith and Wang introduced eight simple inerter-based suspension layouts which only contain no more than one inerter and one damper. For both quarter- and full-car models, around 10% or greater improvements were identified for the performances of ride comfort, type grip and dynamic load carrying, individually, comparing with the conventional strut. Multi-objective optimisation considering both ride comfort and dynamic load carrying was also carried out to demonstrate the benefits. The optimisation results obtained in [100] were consolidated by [93] and [101]. In [93] the authors proposed a procedure to allow the optimisation over any positive-real admittances. By allowing high-order immittances to be optimised, better improvements in vehicle dynamic performances were identified in [93]. In [101], the global optima of ride comfort and tyre grip performances measures

were determined analytically for six simple layouts, several of which are proposed in [100]. The effects of inerter-based vehicle suspensions on the trade-off between different vehicle performance criteria were investigated in [102] and the benefits were highlighted. In [86], a mechatronic strut was proposed to realise an optimal high-order system immittance, which was demonstrated to enhance system performance. Optimisations of inerter-based vehicle suspensions have also been demonstrated in [103, 104]. Experimental efforts were made to present the dynamics of the inerter-based struts in [100, 93, 101, 104]. The effects of nonlinearities encountered in ball-screw and fluid-based inerter devices on vehicle suspension performance were investigated in [79] and [105], respectively.

Research into the use of inerters in railway vehicle suspension systems is ongoing. The first significant contribution towards this topic were made by Wang *et al.* in [94, 106]. In [94], the improvements of two simple inerter-based layouts in passenger comfort and system damping ratio along vertical deflection were achieved, in comparison with the conventional layout. Further benefits of inerter-based railway suspensions were identified with high-order immittances. The experimental testing illustrated that while the performance advantages are lessened due to inerter nonlinearties, they are still significant. The inerter was also shown to be effective to increase the critical speed to maintain the lateral stability [107]. Such studies were extended to improve the ride comfort performance in [108]. Jiang *et al.* [108] demonstrated the benefits of the inerter inclusion in the secondary vertical and lateral suspensions to improve ride comfort. The effects of track irregularities were emphasised in [109]. For a more thorough review of this topic, see [110].

Moreover, applications of the inerter have been also explored in the steering compensator of the high-performance motorcycles [91, 111], to improve the stability of the 'wobble' and 'weave' modes.

Civil engineering systems

Applications of inerter-based suspension have been extended to civil engineering systems with extensive research, most of which are focused on buildings. The earliest work on inerter-based building suspension was conducted by Wang *et al.* with the publications [3, 112]. In [3], two simple inerter-based layouts which are shown in Figs. 2.4 (a) and (b) were proposed to locate between the primary structure base and the ground. Comparing with the conventional passive suspension, the benefits due to the inclusion of inerter were investigated in suppressing the traffic- and earthquake-induced vibrations, with different building models. Built on these results, a more comprehensive study was presented in [112] with an additional more complex inerter-based suspension layout

considered. Experimental verification was conducted with a ball-screw inerter prototype. Subsequently, significant contributions to this field were made in Japan, which were motivated mostly by earthquake engineering. In [113], an inerer-like device, named as 'inertia mass damper' (or dynamic mass in [114]), was proposed to function as a negative stiffness in parallel with the conventional suspension. The aforementioned TVMD device was another application using the inerter concept [4] and took advantage of the mass amplification effect through a ball-screw mechanism with a suitable gearing. Comparing with other damper devices, the effectiveness of TVMD to suppress ground-excited vibrations was illustrated theoretically and experimentally using a building model with single DOF. Extended work using a multiple degree-of-freedom (DOF) building model was reported in [115] to demonstrate the effectiveness of TVMD in enhancing the building modal responses. Further, Lazar *et al.* [5] suggested the TID as an attractive alternative to a conventional TMD. Contrast to the TMD which only acts on one single storey, the two-terminal TID can be connected between two storeys or the storey and the ground. Lazar *et al.* suggested that the TID can provide an enhanced seismic control responses with a much smaller device mass added to the primary structure. Considering a single TID, authors concluded the best position of the TID was at the bottom level connected to the ground, and offers the potential to suppress both the targeted mode and the responses at higher frequencies. Another notable inerter-based building suspension that also utilizes the mass amplification effect is tuned mass-damper-inerter (TMDI) described in [116, 117], of which [117] focused on the wind-induced vibrations. Employing the network synthesis method, Zhang *et al.* proposed a series layouts with fixed sized inerter and four beneficial configurations were identified with respect to the inertance and brace stiffness. More published work related with this topic are also presented in [118, 119].

Other applications of using inerter for structural control are also developed, such as for structural cables [120–122], wind turbines [123, 124] and historical objects [125], etc. In [120], the authors demonstrated the beneficial use of TID for suppressing cable vibrations, with greater modal damping ratios over the traditional dampers for the first model. Luo *et al.* [121] proposed two beneficial inerter-based layouts to multi-mode cable vibration suppression.

Aerospace engineering structures

Inerter application to aerospace structures is a relatively new topic. Given the nature of the inerter that the inertance can be much smaller than the device's own mass, inerter-based devices potentially have inherent advantages when applied to aerospace structures

[126]. The application of inerters to landing gear shimmy was investigated in [127]. Xin *et al.* concluded that the application of inerter may destabilise the system if the gear geometry parameters were not chosen appropriately. Furthermore, they also investigated the effects of inerter on the shimmy performance considering different linear landing gear models. This work was expanded by Liu *et al.* [128]. They studied the influence of inerter on the responses of the nonlinear and its linearised models under different initial conditions. Szczyglowski *et al.* studied the effectiveness of TID in a truss-braced wing to reduce gust loading. In comparison with a pure damper, 25% and 5% reduction of root bending moment and root torque were obtained by TID, respectively.

Note that the aforementioned review of inerter applications is within the context of passive vibration suppression. Semi-active and active inerter-based vibration suppression are also being studied while it's not within the scope of this thesis. Interesting results can be found in [129–133].

2.4 Research motivations and objectives

In Section 2.1, three different types of undesirable vibration behaviour were explored: transient, steady-state and self-excited vibrations. A number of typical examples were reviewed. It is crucial to design effective suppression mechanisms to mitigate these types of vibrations. However, in most cases, it is a difficult task to satisfy complex, and sometimes conflicting, design requirements, which are determined by the problem nature.

To suppress the unwanted vibrations of engineering systems, three strategies, passive, active and semi-active, were employed in vibration suppression, as discussed in Section 2.2. It was discussed that active and semi-active methods were extensively studied and the promising performance enhancement has been obtained. Passive vibration suppression devices are still widely adopted by industry due to their inherent advantages, such as simple design, low cost, unconditional stability and high reliability. Additionally due to the introduction of inerters, the range of the dynamic behaviour that can be realised by passive absorbers is fundamentally enlarged. Thus, this thesis focuses on passive devices design, for application to industrial problems.

The conventional design of the passive devices commonly uses a few simple traditional structures. However, the potential performance of the devices, employing each fixed structure, is determined by physical constraints of the elements. To achieve more enhanced vibration suppression performance, it is essential to explore more complex structures and identify optimal configurations consisting of springs, dampers and inerters

in a systematic manner with respect to different criterion. This is the primary motivation of this thesis.

Additionally, a mechanical (or hydraulic or electrical) structure, which is not actively controlled, can be regarded as a passive device. Thus, a systematic optimisation methodology for passive devices might contribute to mechanical design, such as the physical device arrangement, in certain circumstances. The possibility of a systematic methodology is beneficial for mechanical optimum design procedure, which is currently significantly based on practical experience or trial-and-error approaches.

In Section 2.3.3, a single inerter shows an improved vibration suppression performance comparing with a conventional TMD design. Additionally, it was shown that with the help of inerters, a wide range of passive structures with enhanced performances can be realised. Thus, it is valuable to explore the potential benefits of exploiting inerters for suppressing the three types of vibration problems discussed in Section 2.1.

Motivated by the aforementioned observations, there are three objectives in this thesis. The first one is to propose systematic design approaches to identify the optimal configurations consisting of linear passive elements for vibration suppressors. The second objective is to apply a systematic optimum design approach on optimising the mechanical/hydraulic/electrical design, e.g. physical device arrangement. A particular example is the hydraulic engine mount design in this thesis. Typical vibration problems are considered with three examples, each representing one of these problems, investigated. These are landing gear shimmy, aircraft landing impact and combustion engine vibrations. With respect to these three example problems, the third objective is to exploit the potential benefits of passive inerter-based suppression.

2.5 Thesis outline

Chapter 3 concentrates on suppressing transient oscillation using a linear passive suppression device. Landing gear shimmy problem of a Fokker 100 aircraft MLG is examined in this chapter. A linear model of the MLG equipped with a default shimmy-suppression device, i.e. shimmy damper, is presented. Apart from such default device layout, two additional layouts incorporating inerter are proposed for optimum design. Eigenvalue optimisation is carried out while the results demonstrate the limitation of frequency-domain analysis for this problem. Then time-domain optimisation is proposed, using cost functions of the maximum amplitude and the settling time of torsional-yaw motion. Applying two types of excitations which trigger the shimmy oscillations, performance

advantages of inerter-based configurations for suppressing MLG shimmy, together with corresponding parameter values, are identified.

Suppressing the transient vibrations caused by an initial impact is investigated in Chapter 4, which explores the aircraft touch-down process. A simplified landing gear model is presented and the baseline performance of a conventional oleo-pneumatic shock absorber is established. Candidate layouts with linear mechanical components, which are springs, dampers and inerters, are considered. Guaranteeing that the optimum shock struts absorb at least the same level of kinetic energy as the baseline system, the optimisations are carried out using three different objective functions, i.e. the strut efficiency, the maximum strut load and the maximum strut stroke. It is demonstrated that improved touch-down performance can be achieved with a linear inerter-based configuration. However it is also observed that the potential energy stored in the gear at the end of the first compression stroke exceeds that of the baseline nonlinear system. This suggests a poorer elongation stage might be observed. To address this, an additional constraint on energy dissipation is then implemented in the optimisation process to maximise the strut efficiency and minimise the maximum strut load. To achieve a reduced potential energy, the absorber with a double-stage compression spring is introduced. Then inerter-based configurations that provide improvements for the performance indices of interest are identified and presented.

In Chapter 5, it is shown that passive devices are capable to prevent the instability of self-excited oscillations, correspondingly a method of selecting the device parameter values is proposed. This is demonstrated with the application of MLG shimmy problem via continuation analysis. A nonlinear mathematical model for a dual-wheel MLG is developed to represent the gear dynamics. The effects of the shimmy-suppression devices on the MLG system are investigated with a bifurcation study using the continuation software AUTO. The aircraft forward velocity and the device damping are used as continuation parameters, allowing us to identify the device parameter region in which no sustained shimmy oscillations occur over the entire operating speed range. It is found that, such parameter region for the conventional shimmy damper is narrow and hence a tight tolerance. It needs to be enlarged to provide a larger parametric operating range for the damping device, then increased device robustness. By adding an additional spring in series with the shimmy damper layout, a spring-damper layout is proposed and its ability in expanding the zero-shimmy region are assessed. Based on this layout, two inerter-combined devices are then proposed. Their effects on the bifurcation diagrams are then studied and and yield further benefits on expanding the zero-shimmy regions in the two-parameter bifurcation diagrams.

The optimal design approaches proposed in Chapters 3, 4 and 5 focus on the device configurations with ideal springs, dampers and inerters while do not take their physical realisations into consideration. In Chapter 6, a study of optimising the mechanical/hydraulic design, e.g. the physical device arrangements, is presented with a systematic design approach. It is demonstrated by improving the performance of a hydraulic engine mount through interior fluid passageway design. A systematic design approach to identify optimal fluid passageway configurations is proposed. The nonlinear mathematical model of a conventional hydraulic mount for a full range of concerned frequency is presented. The low-frequency maximum displacement transmissibility is used as the cost function to be minimised. Two types of fluid passageways, the inertia track and the flow restriction, are considered. First a linearised low-frequency model which does not consider the effects of decoupler is used. By optimising over all possible networks with up to four fluid passageways while considering geometry constraints, linear beneficial configurations are identified. It is then shown that the low-frequency responses obtained with linearly optimised solutions are affected notably by the decoupler mechanism and the high-frequency performances deteriorate slightly comparing with the default system. To address these, optimisations are extended using a nonlinear model, and by limiting high-frequency dynamic stiffness. From the results it is shown that the improvement in terms of low-frequency cost function is reduced if the high-frequency constraint is applied. A sensitivity analysis of low-frequency performances to high-frequency constraint is then carried out and it is shown that if the high-frequency constraint is relaxed slightly, the maximum low-frequency displacement transmissibility can be improved significantly. One notable configuration, in which an inertia track and a restriction flow meter are configured in parallel, is able to provide considerable improvement for low frequency and also significantly reduced high-frequency dynamic stiffness.

Finally, in Chapter 7, the conclusions in this thesis are summarised, along with some potential future research directions.

Chapter 3

Time-domain optimisation of damper for shimmy transient performance

3.1 Introduction

The work reported in this chapter concentrates on suppressing transient vibrations triggered by initial perturbations using linear passive suppression devices and the optimal configurations are obtained. Landing gear shimmy transient vibration is chosen as an example problem here. Time-domain optimisations are carried out using cost functions of the maximum amplitude and the settling time of the gear torsional-yaw motion. Performance advantages of inerter-based configurations for suppressing MLG shimmy transient vibration, together with corresponding parameter values, are identified.

When an aircraft is operating on the ground, the landing gear may experience oscillatory motion, which is well known as shimmy. As discussed in Section 2.1.3, shimmy is often regarded as self-excited oscillations. We note that in the literature shimmy often refers to instability phenomenon, which will be discussed in Chapter 5. While here the shimmy transient vibrations for the system that will not suffer from any instability are explored. In this case, severe transient response can still cause component degradation or passenger discomfort. Such vibrations are termed as 'stable shimmy transient vibrations' here and are the main interest of this chapter.

In the design process, the demand for suppressing shimmy may impose several design constraints on the structural stiffness and geometry of landing gear [134]. However, if modifications to geometry, stiffness or weight are infeasible or undesirable, a shimmy damper is often introduced to alter the response [13]. Normally passive dampers are used, however, alternatives have been proposed in the literature. For example, it has been proposed that that the control orifice, present in some nose-gear hydraulic steering

actuators, can be used to suppress shimmy [135]. Typically the shimmy damper, which is modelled as a damping coefficient in parallel with the gear torsional stiffness [136], is used to suppress shimmy oscillations [6, 137–139]. In [6], it has been shown that a torque link apex shimmy damper can increase the yaw damping to avoid shimmy instability. The damping effect is shown to be of particular significance in the shimmy damper design [138, 139]. Recently, studies have proposed semi-active or active shimmy-suppression strategies, such as using fuzzy adaptive control [64], sliding mode control [65], and magnetorheological damping [140]. However, while such semi-active or active controllers outperform passive ones, passive devices do have some advantages as introduced in Section 2.2. So current shimmy-suppression methods are typically still passive shimmy dampers [65].

For landing gear shimmy analysis, although the real landing gear systems exhibit many nonlinear characteristics, there are still some linear or quasilinear methods, especially efficient on small amplitude of shimmy case. In [6], Van der Valk *et al.* carried out an eigenvalue analysis to predict the shimmy dynamics of the Fokker 100 MLG. Such examples can also be found in [141, 142]. However, Somieski still pointed out that the importance of nonlinearities in shimmy vibration analysis should be emphasised [142]. In this Chapter, linear shimmy analysis is carried out to explore the gear dynamics, while it will be extended to nonlinear field in Chapter 5.

In this chapter, we first review a linearised model of the Fokker 100 MLG equipped with a shimmy-suppression device in Section 3.2, which is used to capture the the effects of suppression devices on MLG dynamics. In addition, three low-complexity layouts of shimmy-suppression devices are proposed, one of which is the layout of conventional shimmy damper while the rest two incorporate inerters. In Section 3.3, eigenvalue optimisation is carried out to maximise the least damping ratio. It is shown that the frequency domain analysis is limited for this problem. Then time-domain analysis is performed in Section 3.4. In order to determine the effectiveness of shimmy-suppression device, the case in which the MLG operates over a rough runway is considered. Two types of tyre perturbations are considered to trigger the shimmy oscillations. Using two cost functions of the maximum amplitude and the settling time of torsional-yaw motion, time-domain optimisation is carried out. It is shown that the performance advantages achieved with the beneficial shimmy-suppression devices exceed those obtained by making significant changes to the gear geometry. The benefits due to the inclusion of an inerter are also discussed. It is examined that the two beneficial configurations also provide performance advantages when the other non-optimised input is applied. Furthermore, it is shown that these beneficial devices will not influence the tyre motion significantly.

Publications resulting from this work

Y. Li, J. Z. Jiang, and S. A. Neild, "Inerter-based configurations for main-landing-gear shimmy suppression," *Journal of Aircraft*, vol. 54, no. 2, pp. 684–693, 2016.

Y. Li, J. Z. Jiang, and S. A. Neild, "Optimisation of shimmy-suppression device in an aircraft main landing gear," in 13th International Conference on Motion and Vibration Control, MOVIC 2016, *Journal of Physics: Conference Series*, vol. 744, no. 1, IOP Publishing, 2016.

3.2 Main-landing-gear model and optimisation procedure

In this section, a model of the Fokker 100 MLG equipped with a shimmy-suppression device is presented based on the work by Van der Valk and Pacejka [6]. The model characterises the motion of the system in terms of several oscillatory DOFs of MLG, shimmy-suppression device and tyre dynamics. Moreover, three candidate layouts of shimmy-suppression devices are also introduced.

3.2.1 Description of the dynamic system

The geometry of the Fokker 100 MLG is illustrated in Fig. 3.1 through different views. The structure consists of a main fitting, side-stay, sliding member, axle assembly, etc. The side-stay laterally supports the main fitting and is fixed on the pintle. The sliding member allows both translational and rotational motions with respect to the main fitting. The two wheels are connected by the wheel axle which is offset from the main fitting axis via a mechanical trail bar of length e. The shimmy-suppression device, conventionally the shimmy damper, is installed at the torque link apex point, as shown in Fig. 3.1(b). A global coordinate frame (XYZ) is considered and its origin is fixed to the pintle axle. The X axis points in the direction of aircraft forward direction, the Z axis vertically downwards, and the Y axis completes the right-handed coordinate system. The wheel axle of the MLG is allowed to rotate torsionally about the centre line of the main fitting by the angle ψ (torsional-yaw DOF) and to deflect laterally by the displacement y. Modal coordinate η is used to indicate the MLG lateral DOF and will be discussed later. In addition, the wheel axle is allowed to rotate about an axis fixed along the trail bar by the angle ϕ (torsional-roll DOF). These three DOFs represent the MLG motions and are coupled via the tyre lateral deformation. Figure 3.2 illustrates the sign conventions of these DOFs and the tyre lateral deformation. In Fig. 3.2(a) the two wheels are collapsed into one plane with respect to the point A. Note that in this model, the fuselage dynamics

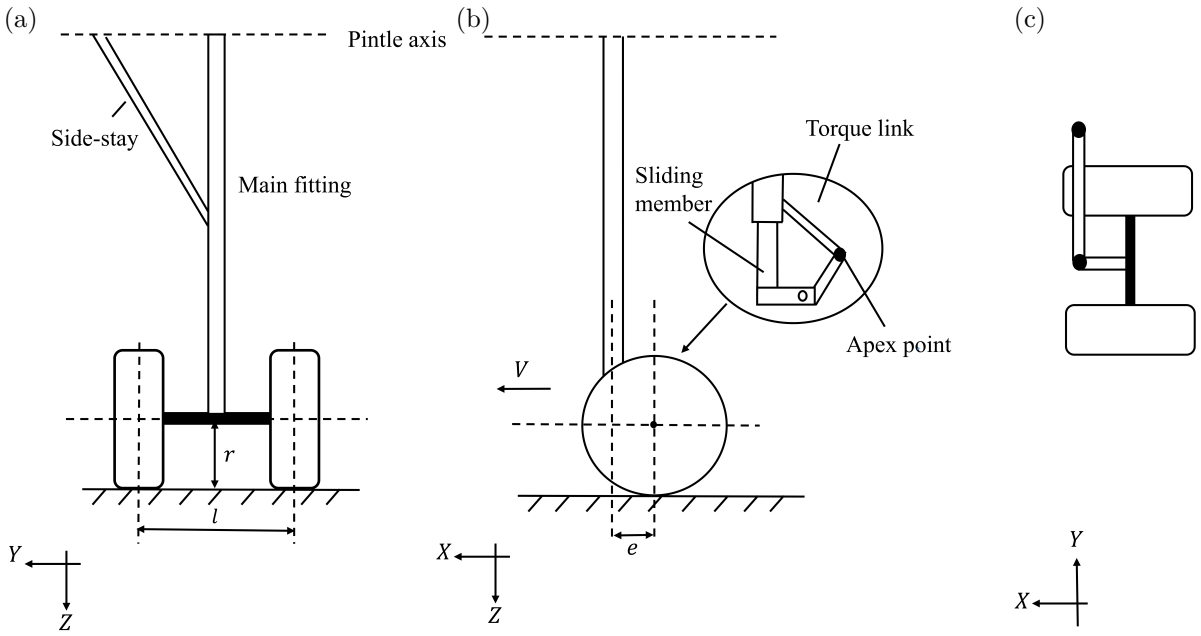

Fig. 3.1 Schematic view of the dual-wheel Fokker 100 MLG geometry.

are ignored and a tyre-ground contact constraint is assumed. The interaction between the landing gear shimmy modes and the fuselage dynamics is considered in [143]. Moreover, no axial compression of the strut is considered in this analysis.

In this model, $c_{\psi,\phi}$, $k_{\psi,\phi}$ are introduced to represent the damping and stiffness of the ψ and ϕ DOFs. Note that here we use the conventional notification k for spring and c for damper, different from the ones used in [6] (c for spring and k for damper). The total effective torsional-yaw moment of inertia of the landing gear around the strut axis is

$$I_{\psi tot} = I_{\psi} + m_1 e^2 + \frac{1}{2} I_{yb} \left(\frac{l}{r}\right)^2, \tag{3.1}$$

where the lengths of l and r are defined in Fig. 3.1, I_{ψ} is the moment of inertia of the wheels, axle and brake assembly about Z axis passing through their centre of gravity, m_1 the unsprung mass and the contribution of the term $m_1 e^2$ is due to the offset between the strut axis and the wheel axle. I_{yb} is the polar moment of inertia of the wheels, axle and brake and the gyroscopic effects caused by the rolling wheels also add the extra term $\frac{1}{2} I_{yb} \left(\frac{l}{r}\right)^2$ to the total effective torsional-yaw moment of inertia.

As for the MLG lateral motion, the gear lateral bending deflection is expressed by

$$y(z,t) = f(z)\eta(t), \tag{3.2}$$

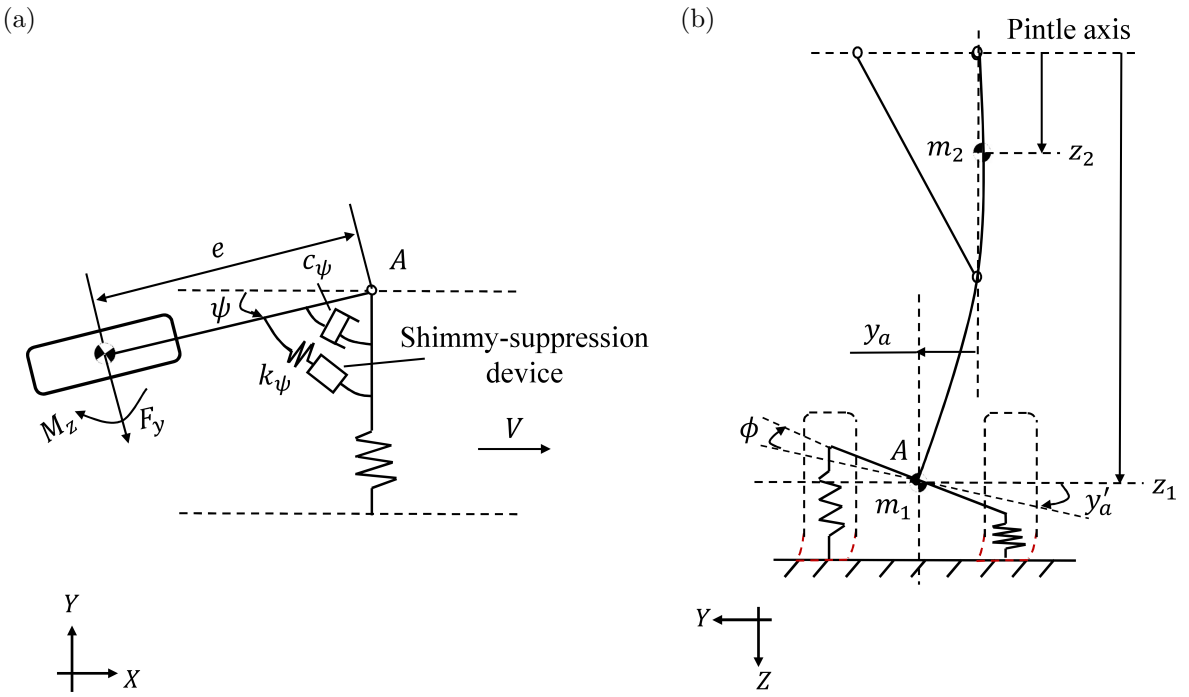

Fig. 3.2 (a) Torsional-yaw ψ DOF, (b) lateral deflection of A y_a and roll ϕ DOF (a modified version of Figs. 2 and 3 in [6]).

where $f(z)$ denotes the approximate mode shape belonging to the first mode of the freely hanging landing gear. The landing gear is regarded as a beam with two concentrated masses: unsprung mass m_1 and the main fitting m_2, see Fig. 3.2(b) with their mode shapes, $f(z_1)$ and $f(z_2)$, respectively. Thus from Rayleigh's method, the energy terms representing the lateral mode can be expressed in terms of the corresponding modal mass m_f, which can be written as

$$m_f = m_1 f^2(z_1) + m_2 f^2(z_2). \tag{3.3}$$

The lateral deflection and slope at the shock strut bottom point A, y_a and $y_a{}'$, are specified by the following equations:

$$y_a = f(z_1)\eta, \tag{3.4}$$

$$y_a{}' = f'(z_1)\eta, \tag{3.5}$$

where $f'(z_1)$ is the modal slope of A. For the purpose of comparison, it is convenient to consider y_a to represent the MLG physical lateral deflection, instead of η DOF. Moreover, as shown in Fig. 3.2(b), both ϕ and $y_a{}'$ contribute to the overall roll deflection angle of A, ϕ', giving

$$\phi' = \phi + f'(z_1)\eta. \tag{3.6}$$

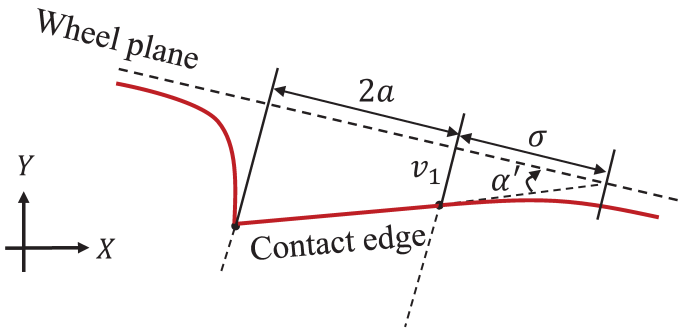

Fig. 3.3 Schematic of the straight tangent tyre model where a represents half of the contact patch length.

To illustrate the physical effects of this angle, the roll stroke δ at the ground level is considered, as given by

$$\delta = r\,tan\phi^{'}. \tag{3.7}$$

The wheel rolling effects are considered in this model. With the assumption of zero tyre longitudinal slip, the angular velocity of the wheel Ω is given by the expression

$$\Omega = \frac{V}{R_e}, \tag{3.8}$$

where R_e is the effective radius of the tyre and V is the aircraft forward speed. For the expression of R_e, the empirical equation

$$R_e = R - \frac{1}{3}d \tag{3.9}$$

can be used, where R is the tyre unloaded radius, $d = R - r$ is the tyre deflection, see Currey [14]. In this study, the straight tangent tyre model is used to describe the tyre-ground contact dynamics as shown in Fig. 3.3. The reaction forces produced by the tyres can be modelled by the tyre lateral deformation. These forces are the lateral force F_y and the tyre self-aligning moment M_z, as shown in Fig. 3.2(a), and may be expressed as

$$F_y = C_{F\alpha}\alpha^{'}, \tag{3.10}$$

$$M_z = -C_{M\alpha}\alpha^{'}, \tag{3.11}$$

where $\alpha^{'}$ is the lateral deflection angle of the leading point of tyre-ground contact edge. The lateral displacement of the leading point of contact edge, v_1, is considered to represent

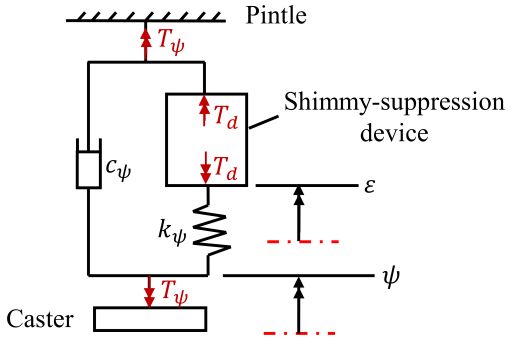

Fig. 3.4 View of ψ, ε DOFs and k_ψ, where at equilibrium, $\varepsilon = \psi = 0$ and $T_d = 0$ (inspired by [6]).

the tyre lateral deformation when investigating the physical shimmy motion. It can be expressed as

$$v_1 = \alpha^{'}\sigma, \tag{3.12}$$

where σ is the tyre relaxation length, as illustrated in Fig. 3.3. Note that if the MLG is in its undisturbed state, the tyre slip angle α is equal to $\alpha^{'}$.

The shimmy-suppression device is fitted in the apex location which is between the upper and lower torque link. To capture both the structural stiffness of these two parts, an effective torsional-yaw stiffness k_ψ is considered connecting the shimmy-suppression device and the unsprung mass as shown in Fig. 3.2(a). Note that the conventional shimmy damper is a translational device which generates force to control the relative movement of the two torque links. Such characteristics of the shimmy damper can be converted into equivalent torsional characteristics about the strut center line. All the following shimmy-suppression devices discussed have equivalent torsional properties. The DOF 'ε' across the device is introduced to represent the equivalent torsional motion of the shimmy-suppression device. The overall equivalent torque T_ψ generated by torsional damping, torque link stiffnesses and shimmy-suppression device is illustrated in Fig. 3.4. The torque generated by the shimmy-suppression device T_d is balanced by the torsional spring torque $k_\psi(\psi - \varepsilon)$. The expression for T_d is dependent on the device layout. It is the dynamics of the device, which are captured by the relationship between T_d and ε, and their effects on shimmy oscillations are of primary interest here.

3.2.2 Equations of motion

Similar to [6], using Lagrange's method, the corresponding equations of motion for the MLG can be written as

$$E^{\psi}_{11}\ddot{\psi} + E^{\psi}_{12}\ddot{\eta} + E^{\psi}_{21}\dot{\psi} + E^{\psi}_{22}\dot{\eta} + E^{\psi}_{23}\dot{\phi} + E^{\psi}_{31}\psi + E^{\psi}_{32}\alpha^{'} + E^{\psi}_{33}\varepsilon = 0, \tag{3.13}$$

$$E^{\eta}_{11}\ddot{\psi} + E^{\eta}_{12}\ddot{\eta} + E^{\eta}_{13}\ddot{\phi} + E^{\eta}_{21}\dot{\psi} + E^{\eta}_{22}\dot{\eta} + E^{\eta}_{31}\eta + E^{\eta}_{32}\phi + E^{\eta}_{33}\alpha^{'} = 0, \tag{3.14}$$

$$E^{\phi}_{11}\ddot{\eta} + E^{\phi}_{12}\ddot{\phi} + E^{\phi}_{21}\dot{\psi} + E^{\phi}_{22}\dot{\phi} + E^{\phi}_{31}\eta + E^{\phi}_{32}\phi + E^{\phi}_{33}\alpha^{'} = 0, \tag{3.15}$$

$$E^{\alpha^{'}}_{11}\dot{\psi} + E^{\alpha^{'}}_{12}\dot{\eta} + E^{\alpha^{'}}_{13}\dot{\phi} + E^{\alpha^{'}}_{14}\dot{\alpha}^{'} + E^{\alpha^{'}}_{21}\psi + E^{\alpha^{'}}_{22}\alpha^{'} = 0, \tag{3.16}$$

$$T_d - k_{\psi}(\psi - \varepsilon) = 0. \tag{3.17}$$

Here, Eqs. (3.13-3.15) govern the MLG dynamics and (3.16) the tyre dynamics. Eq. (3.17) represents the fact that the torque across k_{ψ} equals the torque across the shimmy-suppression device. The mathematical expression for T_d depends on the layout of shimmy-suppression device and will be presented in Section 3.2.3. The coefficients E^{b}_{aa} for the equations of motion are given as follows. For Eq. (3.13),

$$\begin{aligned}
&E^{\psi}_{11} = I_{\psi tot}, \quad E^{\psi}_{12} = -m_1 e f(z_1),\\
&E^{\psi}_{21} = c_{\psi}, \quad E^{\psi}_{22} = 2I_{yb}\Omega f^{'}(z_1), \quad E^{\psi}_{23} = 2I_{yb}\Omega,\\
&E^{\psi}_{31} = k_{\psi}, \quad E^{\psi}_{32} = -2(eC_{F\alpha} + C_{M\alpha}), \quad E^{\psi}_{33} = -k_{\psi}.
\end{aligned}$$

For Eq. (3.14),

$$\begin{aligned}
&E^{\eta}_{11} = -m_1 e f(z_1), \quad E^{\eta}_{12} = m_f + I_{\phi} f^{'2}(z_1), \quad E^{\eta}_{13} = I_{\phi} f^{'}(z_1),\\
&E^{\eta}_{21} = -2I_{yb}\Omega f^{'}(z_1), \quad E^{\eta}_{22} = 2m_f \zeta_n f_{\eta},\\
&E^{\eta}_{31} = {f_{\eta}}^2 m_f + \frac{1}{2}k_v l^2 f^{'2}(z_1), \quad E^{\eta}_{32} = \frac{1}{2}k_v l^2 f^{'}(z_1), \quad E^{\eta}_{33} = 2C_{F\alpha}(f(z_1) + r f^{'}(z_1)).
\end{aligned}$$

For Eq. (3.15),

$$\begin{aligned}
&E^{\phi}_{11} = I_{\phi} f^{'}(z_1), \quad E^{\phi}_{12} = I_{\phi},\\
&E^{\phi}_{21} = -2I_{yb}\Omega, \quad E^{\phi}_{22} = c_{\phi},\\
&E^{\phi}_{31} = \frac{1}{2}k_v l^2 f^{'}(z_1), \quad E^{\phi}_{32} = \frac{1}{2}k_v l^2 + k_{\phi}, \quad E^{\phi}_{33} = 2rC_{F\alpha}.
\end{aligned}$$

For Eq. (3.16),

$$E_{11}^{\alpha'} = e - a, \quad E_{12}^{\alpha'} = -(f(z_1) + rf'(z_1)), \quad E_{13}^{\alpha'} = -r, \quad E_{14}^{\alpha'} = \sigma,$$
$$E_{21}^{\alpha'} = V, \quad E_{22}^{\alpha'} = V.$$

Table 3.1 Some system parameter values used in the analysis

Parameter	Name	Value
c_ψ	Torsional-yaw damping for the gear	1.06×10^3 N·m·s/rad
c_ϕ	Torsional-roll damping for the gear	5.4×10^2 N·m·s/rad
k_v	Tyre vertical stiffness	8.64×10^5 N·m/rad
k_ψ	Overall torsional-yaw structural stiffness for the gear	6.45×10^5 N·m/rad
k_ϕ	Torsional-roll structural stiffness for the gear	2.15×10^6 N·m/rad
f_η	First natural frequency of hanging landing gear	72.0 Hz
ζ_n	First relative damping coefficient for the lateral mode	0.05

In summary, there are 5 DOFs in the equations of motion, which are ψ for the MLG torsional-yaw motion, η for the gear lateral motion, ϕ for the torsional-roll motion, α' for the tyre dynamics and ε for the shimmy-suppression device motion. The states we actually consider as physical shimmy motions are ψ, y_a, δ and v_1, which are the torsional-yaw deflection, the lateral bending deflection of the point A, the roll stroke of A on the ground and the tyre lateral deformation, respectively. The parameter values used in this study are consistent with [6] (with a 0.25 m shock absorber deflection). Several parameters that are not specified in [6] are summarised in Table 3.1. Note that the aircraft operation condition considered in this study is $V = 50$ m/s. The model presented here has been validated with [6], for example, the calculated system natural frequencies, the damping ratios and mode shapes are close to those presented in Table 5 of [6].

3.2.3 Optimisation procedure and candidate shimmy suppression layouts

As introduced in Section 2.3, the introduction of an inerter alongside the conventional spring and damper guarantees that any positive-real frequency transfer function can be realised by a network layout consisting of springs, dampers and inerters [90]. The dynamics of the candidate shimmy-suppression devices can be represented by general

positive-real functions, $Y(s)$, satisfying

$$\widetilde{T_d}(s) = sY(s)\widetilde{\varepsilon}(s), \tag{3.18}$$

where s is the Laplace variable and $\widetilde{T_d}(s)$ and $\widetilde{\varepsilon}(s)$ represent the torque and the relative deflection of the device in Laplace domain respectively. For example, the transfer function of the default shimmy damper in the Laplace domain may be written as

$$Y(s) = \frac{\widetilde{T_d}(s)}{s\widetilde{\varepsilon}(s)} = \frac{k}{s} + c. \tag{3.19}$$

First we use immittance-based approach to select $Y(s)$ as introduced in Section 2.3.3, i.e. to select a general transfer function then optimise its parameters. Network synthesis theory [88, 89] can then be used to identify the specific layout which can realise the optimised $Y(s)$.

Since low-complexity networks are more preferable due to the weight and space limit of the landing gear system, a biquadratic function (where both the numerator and denominator are second-order functions of the Laplace operator)

$$Y(s) = \frac{As^2 + Bs + C}{Ds^2 + Es + F} \tag{3.20}$$

is considered. For this biquadratic $Y(s)$, the positive-real condition is given by

$$\theta = BE - (\sqrt{AF} - \sqrt{CD})^2 \geq 0, \tag{3.21}$$

which needs to be satisfied [89]. Applying relevant network synthesis techniques, such as the results presented in [95, 96], beneficial layouts can be identified. In this way, we guarantee that a wide range of low-complexity layouts is considered. For most cases, the optimum parameter values (A, B, $\cdots$, F) do not equal zero. The corresponding network normally contains at least five elements. A simplification procedure is then used, to check whether reducing the number of elements results in significant deterioration of performance. A similar procedure can be found in, for example, [92]. A simpler hence more realistic structure can possibly be obtained through this process. A second round optimisation of the element values is then performed for the simplified network layout. Note that during the optimisation process, no restriction due to practical implementation consideration is placed on the parameter values. Instead we consider whether the parameter values are practical after the optimisation stage.

Based on the aforementioned optimisation procedure, three candidate layouts are proposed as illustrated in Fig. 3.5. Layout L1 in Fig. 3.5 represents the conventional shimmy damper layout. Layout L2 shown in Fig. 3.5 is capable of providing promising performance advantages which are demonstrated with the aforementioned optimisation. Even though other more complicated layouts can provide slightly better performances, we take the view that this does not justify the extra complexity of the device. Layout L3 is the layout obtained through the eigenvalue optimisation of Eq. (3.20), which will be discussed in Section 3.3. It will be shown that while this layout can significantly increase the least damping ratio, the overall physical response is not significantly improved. Consequently, discussions will focus on layout L2 in Section 3.4.

For all the optimisations carried out in the present work, we used the Matlab command `patternsearch` first and then `fminsearch` for fine-tuning of the parameters. In the following discussion, we use the notation 'L' to specify the mechanical network layout and 'C' to specify the configurations (*configuration* represents the network topological arrangement (layout) of components that are ideal passive springs, dampers and inerters, as well as their parameter values).

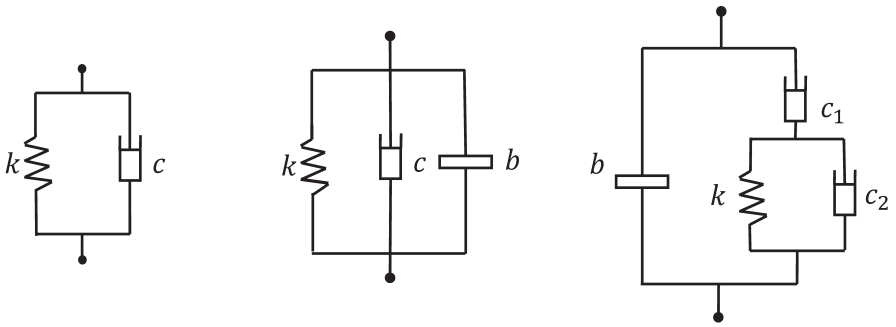

L1 L2 L3

Fig. 3.5 Three low-complexity layouts of the shimmy-suppression device: L1 is the conventional parallel spring-damper layout, L2 and L3 are obtained via the general biquadratic functions and the simplification procedure.

3.3 Limitation of eigenvalue optimisation

As the dynamic model is linear, eigenvalue analysis can be carried out. The equations of motion shown in Eqs. (3.13-3.17) can be expressed in the following state-space form,

$$\dot{X} = TX, \tag{3.22}$$

where $X = (\dot{\psi}\ \dot{\eta}\ \dot{\phi}\ \psi\ \eta\ \phi\ \alpha'\ \varepsilon)^T$ and T is a 8×8 matrix. Applying the Laplace transformation to Eq. (3.22), the system characteristic equation can be written in terms of the Laplace variable.

It can be checked that using the default shimmy damper parameters taken from [6], with $V = 50\,\text{m/s}$, the least damping ratio ζ_{min} amongst all the modes equals 4.4%. Optimisation is carried out to maximise the least damping ratio ζ_{min} with Eq. (3.20) representing the shimmy-suppression device. The optimisation results are given in Table 3.2. Configuration C3 in Fig. 3.5, with parameter values in row 2 of Table 3.2, is obtained via network synthesis to realise the specific biquadratic function identified by optimisation. It can be seen that that a 77.3% improvement on ζ_{min} can be achieved.

Table 3.2 Optimisation results for maximising ζ_{min}

Configurations	ζ_{min}, %	Improvement, %	Parameter values (N·m/rad, N·m·s/rad, kg)
Default	4.4	-	$k = 1.9 \times 10^5, c = 7.4 \times 10^3$
C3	7.8	77.3	$k = 1.5 \times 10^5, c_1 = 4.9 \times 10^3, c_2 = 1.0 \times 10^3$ $b = 13.3$

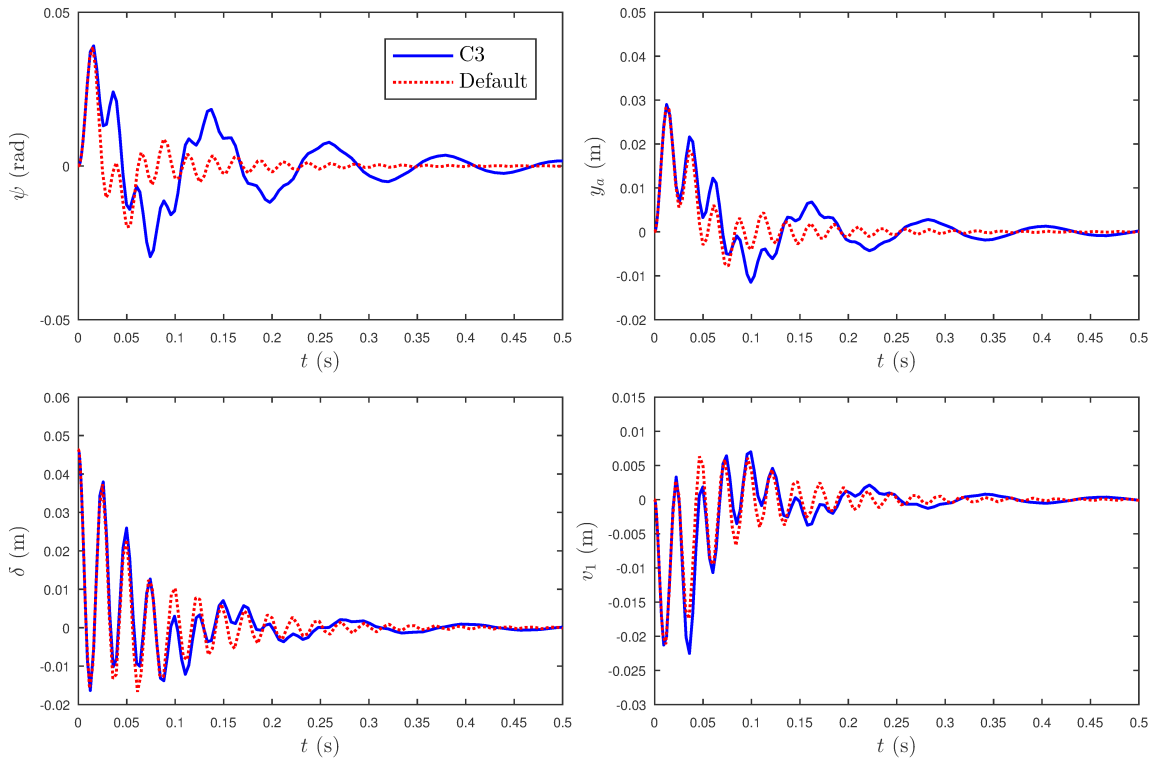

Fig. 3.6 Comparison of time-domain oscillations achieved by the default and C3 configurations ($\phi(t = 0) = 0.1\,\text{rad}$).

It is worth to check the physical behaviour employing the two configurations in Table 3.2. An initial perturbation to the torsional-roll DOF ($\phi(t=0) = 0.1\,\text{rad}$) is used to excite the transient response of the gear. Fig. 3.6 illustrates the response in torsional-yaw deflection ψ, lateral bending displacement y_a, torsional-roll deflection δ and tyre lateral deflection v_1. It can be observed that while the frequency-based optimisation suggests a significant improvement in the least damping ratio with C3, this does not result in an improved transient response due to a larger response to a lower-frequency mode. This suggests that the convenience of the frequency-domain analysis is limited for this problem, as the mode shapes are significantly altered when certain suppression devices are added.

3.4 Time-domain optimisation results

In this section, time-domain optimisation results relating to the performance benefits of shimmy-suppression devices incorporating inerters are presented. Two perturbations, which are applied to the tyre and can trigger shimmy oscillations, are used to excite the transient response. There are a wide range of cost functions that could be used in the optimisation. To demonstrate the potential of an inerter-based device we select the peak amplitude and settling time of the torsional-yaw response as the cost functions. However we recognise that for a full design study a more complex optimisation with multiple performance criteria would be used.

3.4.1 Initial operation conditions and time-domain performance criteria

Two types of initial conditions are considered in this study. Firstly, we assume the tyre travelling direction is disturbed suddenly, causing a corresponding initial input to the tyre slip angle α. As presented in Section 3.2, $\alpha = \alpha^{'}$ when the MLG is in undisturbed state. Hence, $\alpha(t=0) = \alpha^{'}(t=0) = 0.1\,\text{rad}$ is used as the first type of excitations to the system. This input will be referred to as the 'slip input'. The second input, the 'side force input', is an initial side force $F_y^{'} = 1.0 \times 10^7\,\text{N}$ applied in the Y direction to the wheel axle for 1 ms. Note that all the states, except for the excited one, are set to zero initially.

The torsional-yaw motion is oftenly regarded as of significant importance for the gear fatigue life [144]. Therefore, the time-domain optimisation focuses on investigating the effectiveness of the proposed device on the torsional-yaw motion. The performance measures are defined as i) the peak magnitude and ii) the settling time of the torsional-yaw motion. As the transient response to a perturbation is considered, the maximum

amplitude of the torsional-yaw response, ψ_{peak}, is an important measure of the response. Also the time during which the vibration is above a certain threshold, the settling time t_{settle}, gives a measure of the duration of undesirable behaviour following a perturbation. In this paper, t_{settle} is defined as the time duration spent when the amplitude of the response exceeds $\pm 10\%$ of ${\psi_{peak1,2}}^*$, where ${\psi_{peak1,2}}^*$ is the peak response amplitude for the system with the default shimmy damper under the initial tyre slip angle input and side force input, respectively. It can be calculated that ${\psi_{peak1}}^* = {\psi_{peak2}}^* = 1.5 \times 10^{-3}$ rad. Note there are a number of ways in which such performance could be addressed such as setting an acceptable threshold amplitude of vibration. However such a criterion would be perturbation amplitude dependent, giving rise to the challenge of selecting a "reasonable" size of perturbation. Instead we adopt the more general, and amplitude independent, settling time criterion which can be regarded as a measure of effective damping in the linear system analysis. Each of these two measures, peak amplitude and settling time, will be used as a cost function with the constraint that the other measure must be no worse than the value achieved with the default shimmy damper.

3.4.2 Baseline improvement by geometric modifications

From the existing literature, the gear geometry plays an important role in stabilising shimmy-prone gears (see [145] for example). In order to have a benchmark with which the improvement of inerter-based shimmy-suppression device can be compared, two key MLG geometry parameters, wheel distance l and mechanical trail e, are varied. Default shimmy-suppression device and its parameter values are used. The two geometry parameters are varied by $\pm 30\%$ from their nominal values.

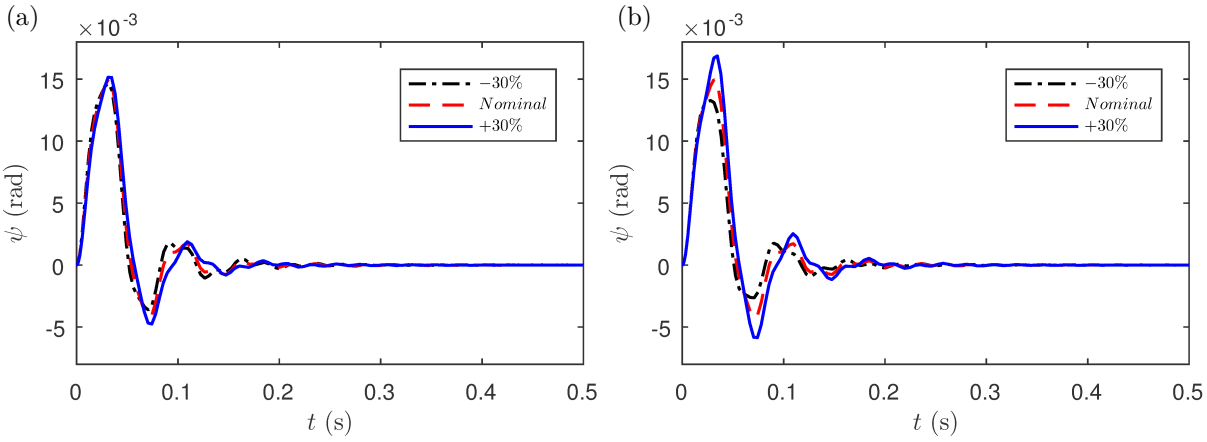

Fig. 3.7 Comparison of ψ time series varying (a) wheel distance l and (b) mechanical trail e for the system with a default shimmy damper configuration.

The slip input is considered. The time-histories of the torsional-yaw motion are plotted for the off-nominal wheel distance and mechanical trail cases in Fig. 3.7. It is observed that the variation of corresponding transient responses is very limited even when large changes in l are applied. Decreasing the wheel distance results in marginally smaller magnitudes of torsional-yaw motion and the response decays more quickly. The biggest improvements on ψ_{peak} and t_{settle} obtained are 2.0% and 14.5%, respectively. Similar trends can be observed for the case that the mechanical trail is varied. With a 30% reduction of e leading to improvements in both performance measures – 11.3% for ψ_{peak} and 14.4% for t_{settle}. This suggests that improvements obtained by modifying the shimmy-suppression device in the order of 10% or more for either performance measure may be thought of as significant.

3.4.3 Optimisation results and beneficial shimmy suppression configurations

By using the optimisation and simplification procedures discussed in Section 3.2.3, layout L2 has been identified as with promising benefits. For clarity, the subscripts α and F are used to specify the optimisation results obtained for the slip input and side force input, respectively. Also, the subscript p (s) is used to represent the optimisation results using the peak amplitude (the settling time) as cost function.

Slip input

Rows 2 and 3 of Table 3.3 summarise the optimal results for improving ψ_{peak}. It can be seen that taking the traditional layout L1, and optimising the spring and damper for this performance criteria results in a 16.7% reduction of ψ_{peak} over the default shimmy damper. With the layout L2, the improvement increases to 28.0%. This significant improvement can be observed from the time series responses illustrated in Fig. 3.8(a).

However, note that the second peak magnitude of the yaw response is increased significantly compared with the default response, especially with the $C2_{\alpha p}$. Hence, an extra restriction is included where the second peak amplitude should be no bigger than that for the default shimmy damper. Here a subscript p^* is used to denote this new optimisation. The p^* optimisation cases are presented in rows 4 and 5 of Table 3.3 and the improved responses are illustrated in Fig. 3.8(b). It can be seen that the second peak amplitude is noticeably smaller than that in Fig. 3.8(a). As expected, the trade-off between ψ_{peak} and the second peak amplitude leads to slightly smaller improvement in ψ_{peak}. However, the improvement by the inerter-based scheme $C2_{\alpha p^*}$, 26.7% over the default system, is still significant. Note again that the peak amplitude optimisation problem can be refined in

Table 3.3 Optimisation results and involved parameter values for the slip input case[§]

Configurations	Performance		Optimum parameter values		
	ψ_{peak} $\times 10^{-2}$ rad	t_{settle} $\times 10^{-1}$ s	k $\times 10^{5}$ N·m/rad	c $\times 10^{3}$ N·m·s/rad	b kg
Default	1.5	1.1	1.9	7.4	-
$C1_{\alpha p}$	1.25(16.7%)	1.08	1.1	14.4	-
$C2_{\alpha p}$	1.08(28.0%)	0.96	3.1	1.5	341
$C1_{\alpha p^*}$	1.3(13.3%)	1.01	1.4	11.8	-
$C2_{\alpha p^*}$	1.1(26.7%)	1.04	7.2	13.0	145
$C1_{\alpha s}$	1.5	0.93(15.5%)	1.1	8.2	-
$C2_{\alpha s}$	1.25	0.47(57.3%)	2.4	8.2	50

[§] % improvements are given in bracket for the criteria being optimised.

different ways, while maintaining the emphasis on minimising the peak amplitude. Here we choose to limit the second peak so that it is no larger than that for the default response, an alternative approach could be to look at the peak-to-peak amplitude, although this would not necessarily result in a maintained or reduced second peak.

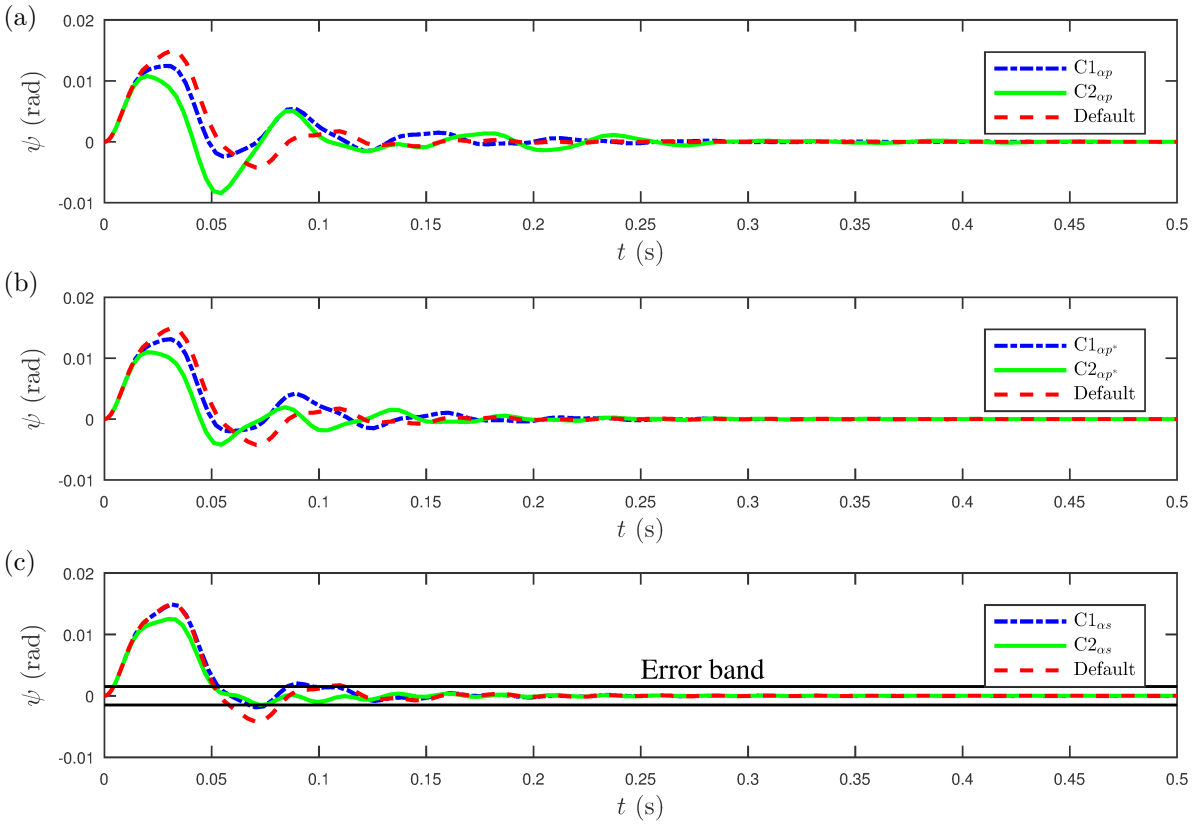

Fig. 3.8 Comparison of ψ time series for the default and beneficial schemes excited by the slip input.

Rows 6 and 7 of Table 3.3 present the settling time improvements provided by $C1_{\alpha s}$ and $C2_{\alpha s}$. A considerable improvement in t_{settle}, 57.3%, is achieved with $C2_{\alpha s}$ scheme while $C1_{\alpha s}$ can only achieve 15.5% improvement. The time series for the torsional-yaw response are shown in Fig. 3.8(c). Note that the response achieved with $C2_{\alpha s}$ decays more quickly and at the same time has a good ψ_{peak} performance. It can be noticed that $C2_{\alpha s}$ can lead to a 16.7% improvement of ψ_{peak}. Taking this into consideration, it could be argued that $C2_{\alpha s}$ is more beneficial over other schemes in Table 3.3.

Side force input

Similar to the slip input case, the optimisation will be performed for the two cost functions separately when the system is excited by an impulsive side force. The optimisation results when minimising ψ_{peak} are summarised in rows 2 and 3 of Table 3.4. Arguably the configuration with a parallel inerter-spring-damper layout is beneficial when compared with the optimal S1 configuration, with a 32.0% improvement over the default device. The responses provided by two optimised schemes are shown in Fig. 3.9(a). As before, an increased second peak is observed when optimising the layout L2. To address this, further optimisation is performed in which the second peak of the response is restricted to be no greater than that for the default system. The results have been shown in rows 4 and 5 of Table 3.4 and the torsional-yaw response is shown in Fig. 3.9(b). Here, by limiting the second peak of ψ response the improvement of ψ_{peak} is reduced, but still significant – 16.7% by $C2_{Fp^*}$.

Table 3.4 Optimisation results and involved parameter values for the side force input case¶

Configurations	Performance		Optimum parameter values		
	ψ_{peak} $\times 10^{-2}$ rad	t_{settle} $\times 10^{-1}$ s	k $\times 10^{5}$ N·m/rad	c $\times 10^{3}$ N·m·s/rad	b kg
Default	1.5	1.22	1.9	7.4	-
$C1_{Fp}$	1.4(6.7%)	1.22	3.5	8.6	-
$C2_{Fp}$	1.02(32.0%)	1.22	3.9	16.2	388
$C1_{Fp^*}$	1.4(6.7%)	1.22	2.5	9.4	-
$C2_{Fp^*}$	1.25(16.7%)	0.97	4.5	10.0	84
$C1_{Fs}$	1.4	1.22(0.2%)	1.2	10.3	-
$C2_{Fs}$	1.5	0.85(30.3%)	1.6	62.8	19

¶ % improvements are given in bracket for the criteria being optimised.

The improvements of t_{settle} achieved by $C1_{Fs}$ and $C2_{Fs}$ are summarised in rows 6 and 7 of Table 3.4, along with the optimised parameter values and the response illustrated in Fig. 3.9(c). It can be seen that the t_{settle} achieved using the optimal S1 is close to that for the default system with only 0.2% improvement. For the parallel inerter-spring-damper configuration, $C2_{Fs}$, a 30.3% improvement is obtained. On the other hand, it can be observed that $C2_{Fs}$ does not provide any improvement of ψ_{peak}, while both performance measures are improved with $C2_{Fp^*}$, 16.7% improvement on ψ_{peak} and 20.5% improvement on t_{settle}. Arguably, here the $C2_{Fp^*}$ is the most beneficial preferable suppression configuration in Table 3.4.

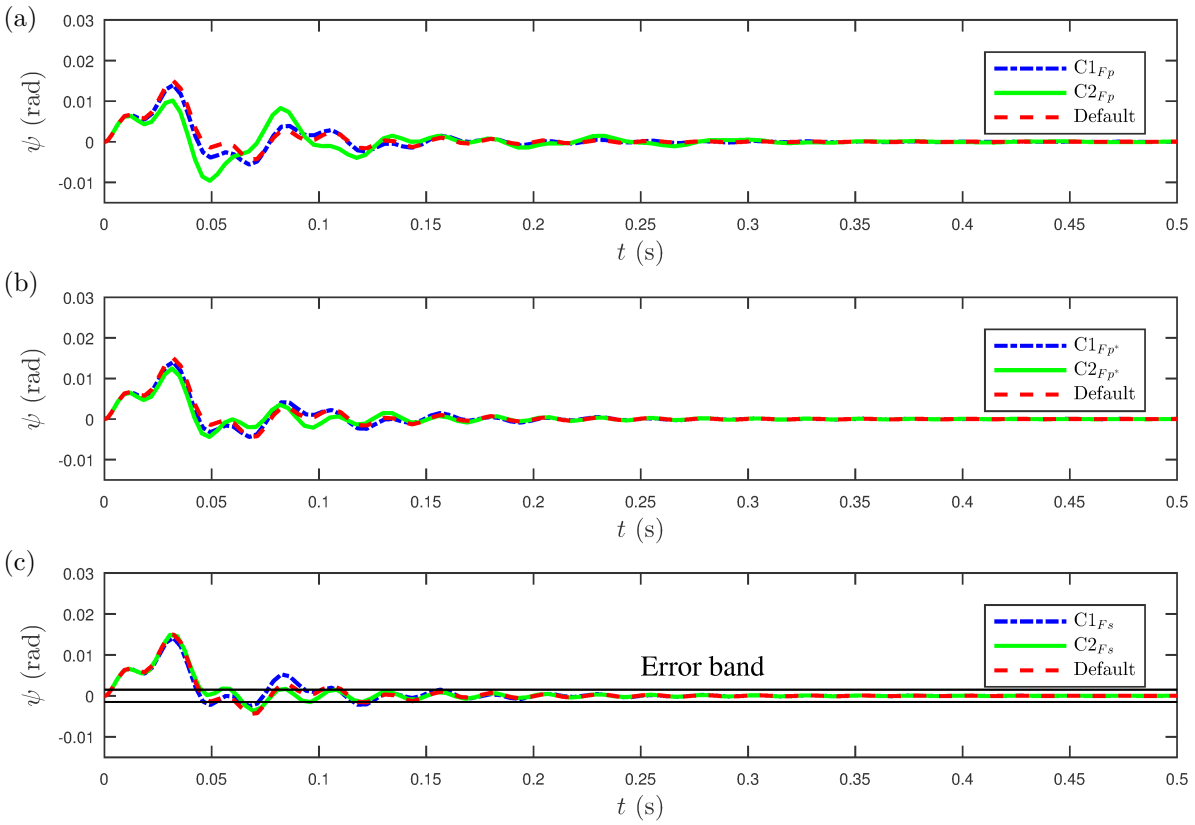

Fig. 3.9 Comparison of ψ time series for the default and beneficial schemes excited by the side force input

3.4.4 Overall beneficial configurations

Based on the results presented in Section 3.4.3, $C2_{\alpha s}$ and $C2_{Fp^*}$ are proposed as the beneficial configurations for the slip input and the side force input, respectively. It is still worth to check the performance with both inputs for $C2_{\alpha s}$ and $C2_{Fp^*}$, respectively.

Table 3.5 Improvement achieved by four optimal configurations under two initial inputs

Configurations	Slip input		Side force input	
	Impro. of ψ_{peak} (%)	Impro. of t_{settle} (%)	Impro. of ψ_{peak} (%)	Impro. of t_{settle} (%)
$C1_{\alpha s}$	0.7	14.9	0	0
$C2_{\alpha s}$	16.7	57.3	9.1	1.0
$C1_{Fp^*}$	8.7	0.36	6.7	0.08
$C2_{Fp^*}$	24.5	33.8	16.7	20.5

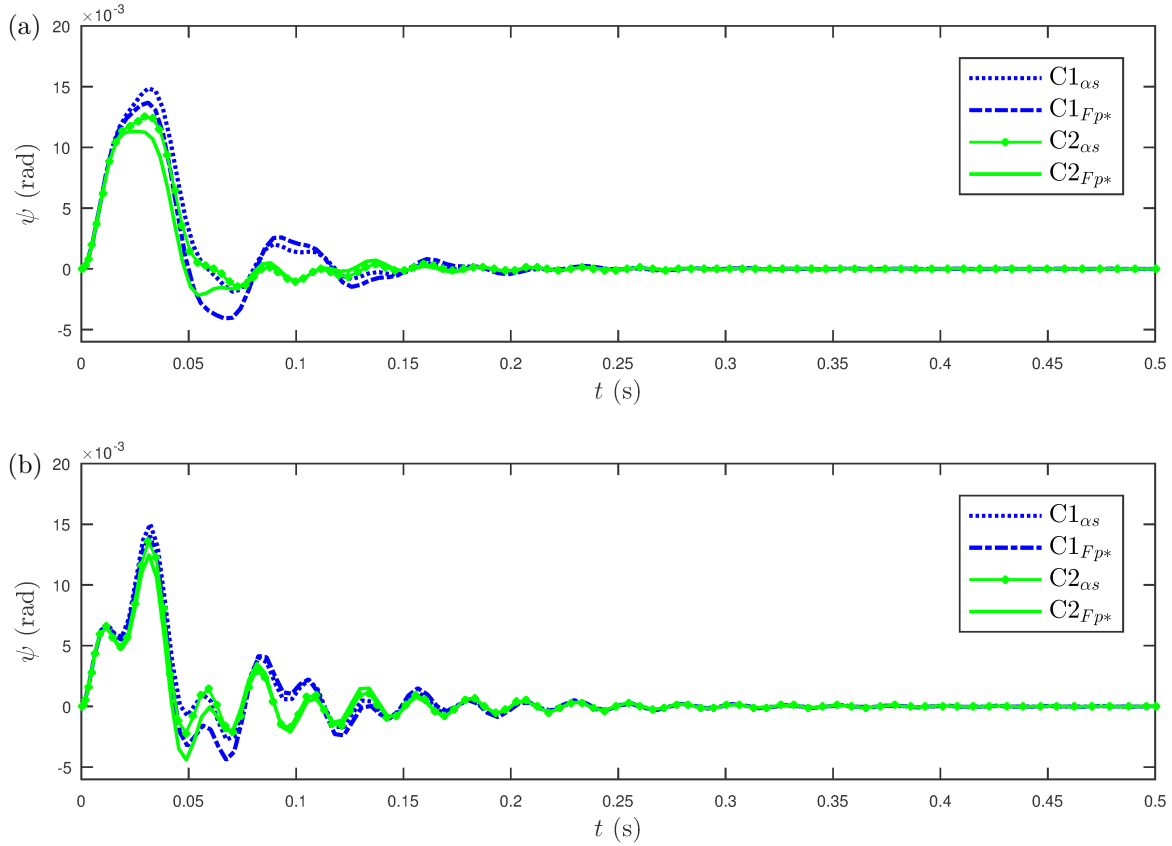

Fig. 3.10 Comparison of ψ time series excited by (a) the slip input and (b) the side force input.

Table 3.5 summarises the improvements of the two performance measures provided by $C2_{\alpha s}$ and $C2_{Fp^*}$ along with the two optimal spring-damper configurations, $C1_{\alpha s}$ and $C1_{Fp^*}$. The percentage improvements are compared with the default shimmy damper and both initial conditions are considered. The table shows that the inerter-based configurations provide larger benefits over the two optimal spring-damper configurations. Moreover, when applying the other input, both schemes still provide benefits using either

performance measure. Figure 3.10 illustrates the comparison of ψ time series produced by the four beneficial schemes when the system is excited by the slip input and the side force input. From the time-domain response, it can be seen that with both kinds of inputs, $C2_{\alpha s}$ and $C2_{Fp^*}$ are always capable of providing performance advantages: experiencing smaller peak amplitudes and quicker setting.

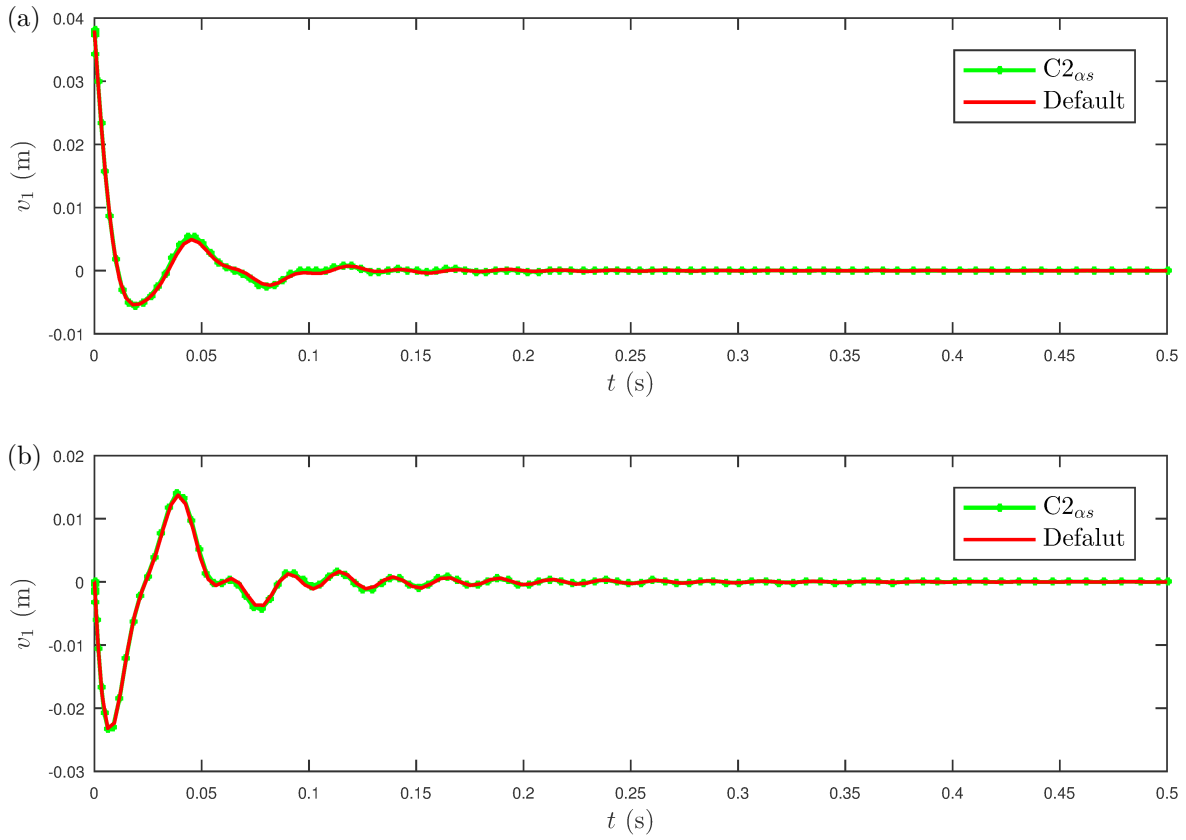

Fig. 3.11 Comparison of v_1 time series excited by (a) the slip input and (b) the side force input.

Since the tyre motion plays an importance role on tyre-ground contact dynamics, it is worth to check the effect of the proposed configuration on the tyre lateral motion. Figure 3.11 illustrates the comparison of the tyre lateral response v_1 for the default and the beneficial configuration (using $C2_{\alpha s}$ as an example). It can be seen that the responses are almost the same compared with the default shimmy damper, which reflects the fact that the torsional-yaw motion is to a large extent decoupled from the tyre lateral motion in this model. Hence, the modification of the shimmy-suppression device has minimal impact on this motion.

3.5 Concluding remarks

For an engineering structure disturbed by external perturbations, the transient responses are of significant interest to be suppressed. In this chapter, we concentrated on suppressing MLG stable shimmy transient oscillations using linear passive suppression devices and investigating the potential benefits of the obtained optimal configurations. Based on time-domain optimisations, it was seen that the identified inerter-based configurations were more beneficial than the geometric modification and the optimised traditional damper design.

Throughout this chapter we considered a linear model of a Fokker 100 aircraft MLG equipped with a shimmy-suppression device. The model characterised the motion of the system in terms of MLG three oscillatory DOFs, namely, the torsional-yaw ψ, lateral η and torsional-roll ϕ motions. The dynamics of the shimmy-suppression devices and elastic tyres were also captured using this model, in terms of ε and $\alpha^{'}$, respectively. It should be noted that this linear model works for small amplitude of shimmy motion. Three candidate layouts for a shimmy-suppression devices were also introduced. One was the conventional shimmy damper layout, i.e. parallel spring-damper layout, the other two layouts incorporated inerters. These two inerter-based layouts were obtained via immittance-based design approach as introduced in Section 2.3.3 and have been shown to be beneficial in this chapter.

Using the linear model, eigenvalue analysis was then carried out, along with the optimisation to maximise the least damping ratio. It was shown that the least damping ratio can be increased significantly with a beneficial inerter-based shimmy suppression device, i.e. 77.3%, comparing with the default shimmy damper. However, by applying an initial perturbation to the torsional-roll DOF, it was shown such beneficial device did not result in an improved transient response, due to a larger response to a lower-frequency mode. This suggested that the convenience of the frequency-domain analysis was limited for this problem, as the mode shapes were significantly altered when certain suppression devices were added.

Based on this observation, time-domain analysis was then adopted for the rest of the work. Since the torsional-yaw motion is oftenly regarded as of significant importance considering the gear fatigue life, the time-domain optimisation focused on investigating the effectiveness of the proposed device on limiting the torsional-yaw motion. Two perturbations, which were applied to the tyre, were used to excite the transient response, namely, the slip input and side force input. The maximum amplitude and the settling time of the torsional-yaw motion were chosen as the cost functions. It was shown that,

when the slip input was applied, a 16.7% improvement on the peak amplitude and 57.3% improvement on the settling time were obtained using a parallel inerter-spring-damper configuration, comparing with the default shimmy damper. If the system was excited by the side force input, the parallel inerter-spring-damper layout with optimised parameter values provided 16.7% improvement on the peak amplitude and 20.5% improvement on the settling time. These benefits exceeded those obtained by making significant changes to the gear geometry, and also optimised parallel spring-damper configurations. It needs to be emphasised that the two beneficial configurations also provided performance advantages when the other non-optimised input was applied. Moreover, these beneficial devices have been shown to have minimal effects on tyre dynamics.

In this chapter, the stable transient responses were investigated and the suppression device performance has been assessed in conjunction with a linear gear model. However, if the system is highly likely to be unstable, the two performance criteria proposed in this chapter will be no long applicable and it gives rise to a stability issue. In Chapter 5, we investigate the shimmy-suppression device configuration design considering MLG stability and extend the study to a nonlinear MLG system.

In general, the aim of this chapter was to show how to design a passive vibration suppression device configuration to suppress stable transient responses disturbed by a sudden perturbation. Another typical type of transient vibration is the one excited by an initial impact. As introduced in Section 2.1.1, such vibrations cause overload to the structure, which may damage the structure, or extremely lead to failure, and their suppression needs to be paid attention to. In the next chapter, we investigate the suppression of transient vibrations caused by an initial impact, with passive suspension designs.

Chapter 4

Optimisation of shock strut design with energy consideration

4.1 Introduction

This chapter focuses on suppressing transient vibrations excited by an initial impact and an optimal design methodology for the absorber configuration considering the energy dissipation requirements is proposed. The landing gear touch-down process is analysed. It is demonstrated that comparing with the conventional oleo-pneumatic shock strut, the inerter-based shock strut configurations can provide considerable benefits on touch-down performances, i.e. the strut efficiency, the maximum strut load and the maximum stroke. The energy distribution of each beneficial strut configuration is analysed and to achieve a reduced potential energy at the end of the compression stroke, a double-stage compression spring is introduced. With this, inerter-based suppression device configurations that provide improvements in the performance indices of interest are identified and presented.

The shock absorber unit, together with other parts of landing gear such as the tyres, is designed to absorb landing impacts and any immoderate shocks transmitted to the fuselage as the aircraft taxis over uneven surfaces [146]. As introduced in Section 2.2.1, the shock absorber performance is mostly governed by the landing touch-down process, which also poses the greatest energy dissipation requirement for the suspension [56]. Specifically, the design requirement is to dissipate all the impact energy without causing the aircraft to rebound, while considering the greatest energy absorption efficiency and the minimum gear load which represents passenger/crew comfort [13].

In practice, a passive oleo-pneumatic shock absorber is typically used, as introduced in Section 2.2. Apart from passive devices, active and semi-active control methods have also been proposed as aircraft shock absorbers [62, 63, 69, 70]. Despite the potential benefits

of actively or semi-actively controlled shock struts, potential issues remain regarding reliability and maintenance cost.

In this paper we consider improving aircraft touch-down performance using a passive shock strut consisting of linear spring, damper and inerter elements. In Section 4.2, we review a simplified landing gear touch-down model, together with a brief introduction of a conventional oleo-pneumatic shock absorber. Several landing touch-down performance criteria are then proposed, namely the strut efficiency, the maximum strut load, the maximum stroke and the reduction of aircraft kinetic energy. Baseline performances are identified by considering a landing gear with a conventional oleo-pneumatic shock absorber. In Section 4.3, four candidate shock-strut layouts are introduced. Optimisations are carried out using three different objective functions, the strut efficiency, the maximum strut load and the maximum stroke while setting the reduction of kinetic energy as a constraint. It is shown that improved touch-down performance can be achieved with a linear inerter-based configuration, comparing with the conventional strut. However it is also observed from an energy analysis that the potential energy stored in the gear at the end of the first compression stroke exceeds that of the baseline nonlinear system. This suggests a poorer elongation stage might be observed.

To address this, an additional constraint on energy dissipation is then implemented in the optimisation process in Section 4.4, to maximise the strut efficiency and minimise the maximum strut load. It is shown that the energy dissipated by a shock strut with a linear supporting spring is limited comparing with one with a nonlinear air spring. We therefore propose a double-stage supporting spring. It is demonstrated that the beneficial shock strut configuration with this spring can provide significant performance advantages and at the same time dissipate the same amount energy as the conventional shock strut.

Publications resulting from this work

Y. Li, J. Z. Jiang, S. A. Neild, and H. L. Wang, "Optimal inerter-based shock–strut configurations for landing-gear touchdown performance," *Journal of Aircraft*, vol. 54, no. 5, pp. 1–9, 2017.

Y. Li, J. Z. Jiang, P. Sartor, S. A. Neild, and H. L. Wang, "Including inerters in aircraft landing gear shock strut to improve the touch-down performance," in X International Conference on Structural Dynamics, EURODYN 2017, *Procedia Engineering*, vol. 199, pp. 1689–1694, 2017.

4.2 Landing gear touch-down model and performance criteria

In this section, a landing gear model and the dynamics of a conventional oleo-pneumatic shock absorber are summarised. In the modelling process, the assumptions regarding some factors are made for the purpose of simplification: the effects of wheel spin-up drag loads and flexibility of the aircraft structure are ignored; a constant damping orifice discharge coefficient and air-compression exponent are assumed in the nonlinear shock absorber model. Further, detailed analyses of such factors are available in the existing literature [16–18, 147]. The model validity was demonstrated via the comparison between the calculated results and drop-test data in [7]. Four performance criteria are then proposed according to the design requirements.

4.2.1 Landing gear model

To model the touch-down behaviour of the landing gear and aircraft, a 2DOF model shown in Fig. 4.1(a) (a modified version of Fig. 1(a) in [7]) is used. Note that this model is designed to capture the first compressive stroke of the shock strut, i.e., from initial contact with the ground to the first point at which the relative velocity of the shock strut is slowed to zero. We define this point as the end of the touch-down process. Angle ϕ represents the rake angle of the strut. The mass of the gear is split into that above the strut and that below it. M_1 denotes the total of the upper gear mass and the fuselage mass acting on the gear and M_2 represents the lower gear mass. The vertical deflections of the two masses are represented by the two DOFs z_1 and z_2, respectively. These deflections are zero just prior to contact being made with the runway. The strut stroke s_s measures the deflection of the shock strut and is expressed by

$$s_s = \frac{z_1 - z_2}{\cos\phi}. \tag{4.1}$$

Fig. 4.1(b) gives the free-body diagram of the touch-down model. The weight of masses M_1 and M_2 is denoted as W_1 and W_2. The aerodynamic lifting force L and the tyre force F_t are applied to the two masses respectively. Specifically, the total aircraft weight is assumed to be fully balanced by lifting force during the full touch-down process, i.e.

$$L = W_1 + W_2. \tag{4.2}$$

The constant lifting force assumption is based on the fact that the compression stroke is sufficiently quick that the aircraft speed and lift may be considered constant over its

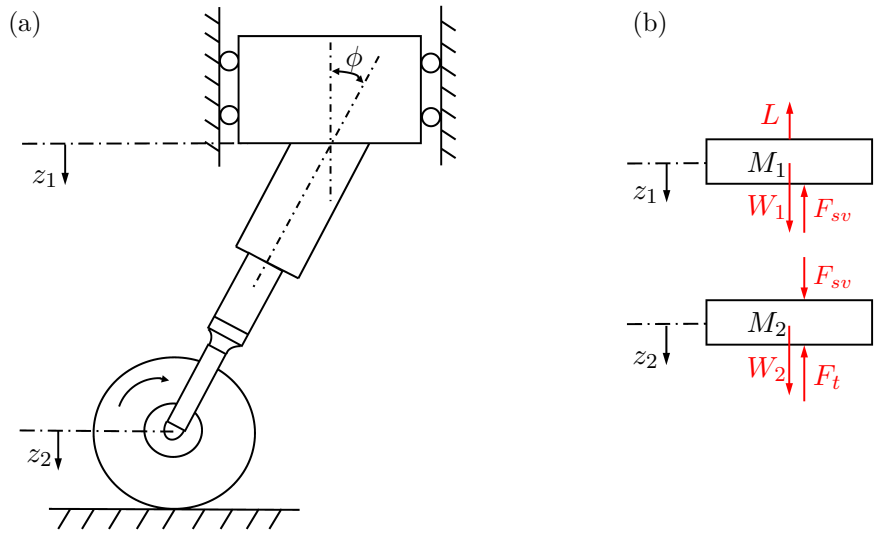

Fig. 4.1 View of (a) the dynamic system, (b) free-body diagram of the model.

duration. This assumption is also used in [14]. Linear force-deflection characteristic of the tyre is given by

$$F_t = k_t z_2, \tag{4.3}$$

where k_t is the linear tyre stiffness in vertical direction. The vertical force generated by the shock strut is represented by F_{sv}, which is

$$F_{sv} = F_s cos\phi, \tag{4.4}$$

where F_s is the strut force along the strut axis. The exact expression of F_s will be discussed in Section 4.2.2. Balancing the forces acting on the two masses, the equations of motion for this system are written as follows:

$$\frac{W_1}{g}\ddot{z}_1 + F_{sv} + L - W_1 = 0, \tag{4.5}$$

$$\frac{W_2}{g}\ddot{z}_2 - F_{sv} + F_t - W_2 = 0, \tag{4.6}$$

where g denotes the gravitational constant. Eliminating F_{sv} gives

$$\frac{W_1}{g}\ddot{z}_1 + \frac{W_2}{g}\ddot{z}_2 + F_t = W_1 + W_2 - L = 0, \tag{4.7}$$

where the right-hand side of the equality makes use of the assumption given in Eq. (4.2). Note that a normal impact condition is considered in this work and a descent velocity $V_0 = 8.86$ ft/s is used at the instant the wheels first touch the ground [7].

4.2.2 A conventional oleo-pneumatic shock absorber

Fig. 4.2 illustrates the schematic view of a conventional oleo-pneumatic shock absorber. The hydraulic fluid is within the lower chamber of the strut and the pressurised gas is contained in the upper chamber. When the strut is compressed, the fluid is forced through the orifice producing a damping force. Meanwhile, the air is compressed by the piston and provides a gas spring force [148]. The internal friction forces between the bearing and cylinder walls are ignored in this work. Then the total strut force can be expressed by

$$F_s = F_h + F_a, \tag{4.8}$$

where F_h and F_a denote the hydraulic damping force and air spring force, respectively.

The hydraulic resistance in the shock strut results from the pressure difference associated with flow through the orifice and provides a velocity-squared damping force, governed by

$$F_h = A_d \dot{s}_s |\dot{s}_s|, \tag{4.9}$$

where the damping factor A_d can be expressed as

$$A_d = \frac{\rho {A_h}^3}{2 C_d {A_n}^2}. \tag{4.10}$$

Here ρ is the mass density of the fluid, A_h is the hydraulic area, C_d is the orifice discharge coefficient and A_n is the net orifice area. According to the polytropic law for the compression of gas, the air spring force is expressed as

$$F_a = p_{a_0} A_a \left(\frac{v_0}{v_0 - A_a s_s}\right)^n, \tag{4.11}$$

where p_{a_0} is the initial strut air pressure, A_a is the pneumatic area, v_0 is the initial air volume and n is the effective polytropic exponent for the air-compression process. Further details of the shock absorber model can be found in [7].

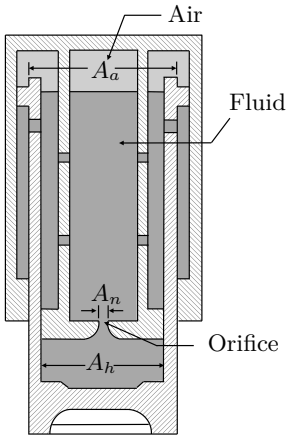

Fig. 4.2 Schematic view of the oleo-pneumatic shock strut (inspired by [7]).

The parameter values of the landing gear touch-down model and the conventional shock absorber used in [7] and in this paper are summarised in Table 4.1. By matching the responses shown in [7], for example, the load-stroke curve shown in Figure 4 of [7], the presented model used in this work has been validated. A few values (noted by *) were not given in [7] but have been provided in Table 4.1 by matching up.

Table 4.1 The parameter values used in the analysis

Parameter	Name	Value	Unit
A_a	Pneumatic area	0.05761	ft^2
$A_d{}^*$	Damping factor of oil damping	339.5	$\text{lb}_\text{F} \cdot \text{s}^2/\text{ft}^2$
g	Gravitational constant	32.18	ft/s^2
$k_t{}^*$	Vertical tyre stiffness	18500.0	$\text{lb}_\text{F}/\text{ft}$
n	Polytropic exponent for air-compression process	1.12	-
p_{a_0}	Initial air pressure	6264	$\text{lb}_\text{F}/\text{ft}^2$
v_0	Initial air volume	0.03545	ft^3
V_0	Descent velocity	8.86	ft/s
W_1	Weight of upper mass	2411	lb_F
W_2	Weight of lower mass	131	lb_F
ϕ^*	Rake angle	12.0	$^\circ$

4.2.3 Performance criteria

Based on the design requirements, namely, to dissipate all the impact energy with the greatest energy absorption efficiency while minimising gear load, four performance criteria are considered in this work. Firstly, the shock-strut efficiency, η_s, is of significant interest

because it indicates the energy absorption ability of the shock strut. Following [14], η_s is defined as

$$\eta_s = \frac{\int_0^{s_{smax}} F_s ds_s}{s_{smax} F_{smax}} \tag{4.12}$$

where F_{smax} and s_{smax} are the maximum strut load and stroke during the touch-down process, as shown in Fig. 4.3. The second criterion is the maximum load transmitted by the shock strut to the fuselage, F_{smax}. This is of significance when considering passenger discomfort and the potential for structural damage. Considering the space limit of a landing gear, the maximum strut stroke s_{smax} is used as the third criterion. In addition, the kinetic energy of the aircraft at the end of touch-down process is treated as the last performance criterion. Specifically, the absolute value of the aircraft vertical velocity at the end of touch-down process, $|V_{end}|$, is used to represent such criterion, which is given by

$$|V_{end}| = |\dot{z}_1(t_{end})|\,, \tag{4.13}$$

where t_{end} marks the end of the compression stroke, when $\dot{z}_1 - \dot{z}_2 = 0$ for the first time after the wheels touch the ground. Each of the first three performance criteria will be used as the optimisation objective function. Specifically, it is desirable for η_s to be maximised while F_{smax} and s_{smax} should be minimised.

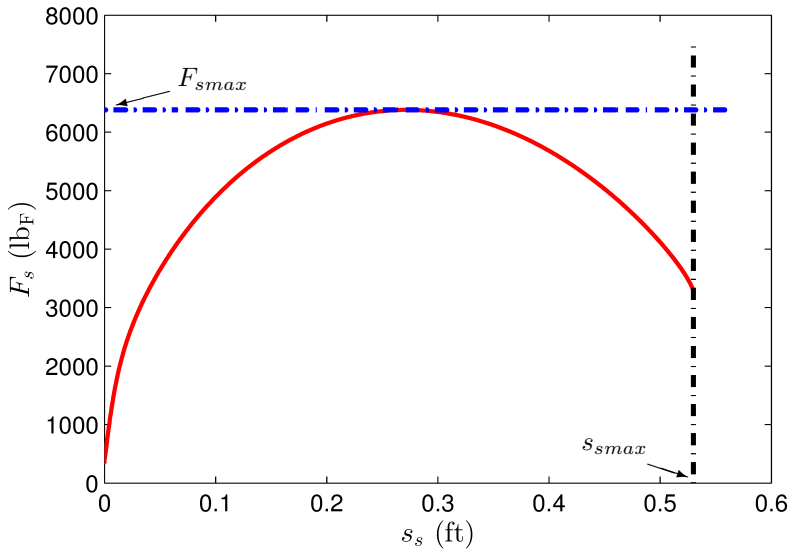

Fig. 4.3 Load-stroke curve obtained by the conventional oleo-pneumatic shock absorber.

4.3 Optimisation results and energy analysis

In this section, four candidate shock-strut layouts are proposed. The response of the landing gear with the conventional nonlinear oleo-pneumatic shock absorber is treated as the baseline. Optimisations are carried out using three different objective functions, the strut efficiency, the maximum strut load and the maximum stroke while the reduction of aircraft kinetic energy is set as a constraint. The beneficial shock-strut configurations and the corresponding performance benefits are identified. Similar with the previous chapter, we use the notation 'L' to specify the mechanical network layout and 'C' to specify the configurations.

4.3.1 Optimisation procedure and candidate layouts

For the default conventional nonlinear shock strut, using the values in Table 4.1, it can be calculated that $\eta_{sd} = 81.5\%$, $F_{smaxd} = 6380.3\,\mathrm{lb_F}$, $s_{smaxd} = 0.53\,\mathrm{ft}$ and $|V_{endd}| = 2.09\,\mathrm{ft/s}$ (the additional subscript 'd' stands for 'default'). Amongst the four performance criteria introduced in Section 4.2.3, η_s, F_{smax} and s_{smax} will each be used as the optimisation objective function with the constraint that the remaining three performance criteria must be no worse than that with the default configuration. For all the optimisations carried out in the present work, we used the Matlab command `patternsearch` first and then `fminsearch` for fine-tuning of the parameters. Note that during the optimisation process, no restriction due to practical implementation consideration is placed on the parameter values. Instead we consider whether the parameter values are practical after the optimisation stage.

Fig. 4.4 illustrates the four candidate shock-strut layouts: L1 is the conventional parallel spring-damper layout; L2 is a parallel spring-damper-inerter layout; L3 is the layout of a series inerter-damper arrangement in parallel with a spring; LY represents a general shock-strut layout with a spring in parallel. Note that for each layout, the spring in parallel, k_s, ensures that the landing gear is capable of supporting the aircraft at the rest position. The lower bound for the stiffness of this spring is set such that the deflection of the gear matches that of the default gear when statically supporting the aircraft ($s_s = 0.50$ ft for a force of $2464.9\,\mathrm{lb_F}$), giving

$$\overline{k}_s = 4884.2\,\mathrm{lb_F/ft}. \tag{4.14}$$

For each layout, optimisations will be conducted for the case where $k_s = \overline{k}_s$ and for $k_s > \overline{k}_s$.

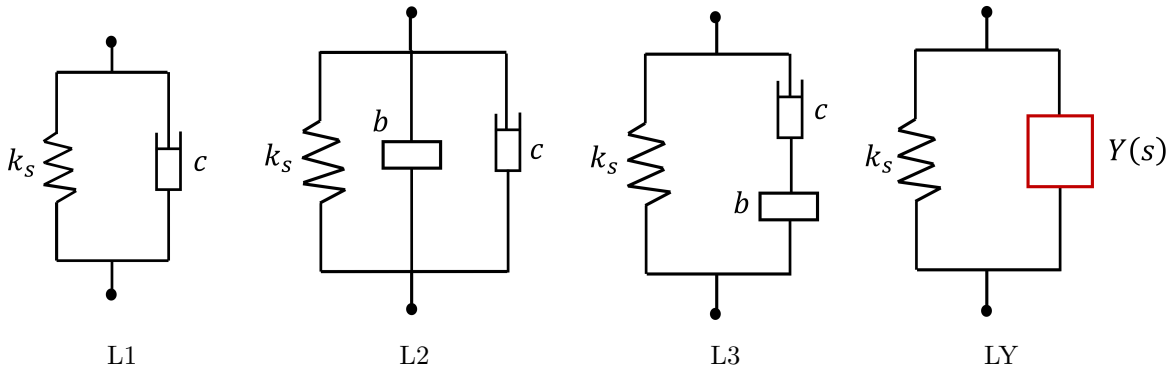

Fig. 4.4 Four candidate shock-strut layouts.

Amongst the four layouts, layouts L1–L3 are proposed based on a structure-based design approach (see Section 2.3.3) to allow an investigation of the potential performance advantages of layouts with the lowest complexity. Layout LY is proposed using the immittance-based approach, allowing for a more complex mechanical structure to be used for improving the touch-down performance. It is represented by a general positive-real frequency function $Y(s)$, which can be realised by a network consisting of springs, dampers and inerters using the network synthesis method [90]. The force-velocity relationship of this layout is given by

$$\widetilde{F_s}(s) = (Y(s)s + k_s)\widetilde{s_s}(s), \tag{4.15}$$

where s is the Laplace variable, $\widetilde{F_s}(s)$ and $\widetilde{s_s}(s)$ represent the force and the relative displacement of the strut in the Laplace domain, respectively. Similar to the approach used in Chapter 3, in order to obtain relatively low-complexity layouts while covering a reasonable range of possibilities, $Y(s)$ is set to be a biquadratic function, which is

$$Y(s) = \frac{As^2 + Bs + C}{Ds^2 + Es + F}. \tag{4.16}$$

The parameter values (A, B, $\cdots$, F) are selected through the optimisation with the condition that they are all non-negative and satisfy the positive-real conditions (Eq. (3.21) of Chapter 3). For the case where k_s is fixed to $\overline{k}_s$, the constraint $F > 0$ is included to ensure that $Y(s)$ does not require an additional parallel spring to supplement k_s. We use the same procedure as the one introduced in Section 3.2.3 to obtain the optimal configuration in this work.

4.3.2 Identified beneficial configurations

The optimisation results are summarised in Tables 4.2 and 4.4. Note that the subscripts η, F and s are used to indicate the results using η_s, F_{smax} and s_{smax} as the objective function, respectively; v is used to specify the case when k_s is allowed to be variable (the $k_s > \overline{k}_s$ case).

Considering layouts L1–L3, no improvement over the default system was identified for the case where $k_s = \overline{k}_s$. Hence Table 4.2 only summarised the results for the $k_s > \overline{k}_s$ case. The configuration $C1_{\eta v}$ can provide a 3.9% improvement in η_s, which is not significant compared with configurations $C2_{\eta v}$ and $C3_{\eta v}$, where up to 10.4% and 13.9% performance improvements can be obtained, respectively. The benefits of including an inerter can be seen by comparing the performance obtained with $C2_{\eta v}$ and $C3_{\eta v}$ to that of the inerter-free $C1_{\eta v}$. Improvements in η_s performance of 6.3% and 9.6%, respectively, are achieved, which can be attributed to the inclusion of an inerter. However, it should be noted that in $C3_{\eta v}$ a much higher damping value is required, which is likely to be impractical. Further optimisation has been carried out to investigate the sensitivity of the performance to reduced levels of damping in L3 and the results have been summarised in Table 4.3 shown below. It is shown that the benefits are still considerable if a reduced damping is used. However, comparing with configuration $C2_{\eta v}$ of Table 4.2, it can be found that the performance improvement obtained by the optimal $C3_{\eta v}$ will be reduced when the damping is constrained to a smaller value; to achieve the same level of improvement as $C2_{\eta v}$, i.e. 10% in η_s, the damping required for the optimal $C3_{\eta v}$ is nearly triple that of $C2_{\eta v}$ and the inertance is doubled. Therefore, we take the view that $C2_{\eta v}$ is more beneficial than $C3_{\eta v}$ from the design and manufacture perspective.

Results with F_{smax} as the objective function indicate that $C1_{Fv}$ can reduce F_{smax} by 12.5% compared with the default performance, and 21.4% and 20.7% improvements can be obtained respectively by the optimum configurations $C2_{Fv}$ and $C3_{Fv}$. Similar to the efficiency optimisation case, it can be seen that a large damping is required for $C3_{Fv}$ and a reduced damping leads to a reduced performance improvement. For the optimisation over s_{smax}, it can be seen that $C1_{sv}$ helps reduce s_{smax} by 18.9% compared with the default configuration. In addition, for $C2_{sv}$ and $C3_{sv}$, the percentage improvements compared with the default performance are 30.2% and 26.4%, respectively.

Table 4.2 Optimisation results using layouts L1–L3[†]

Configurations	Performance			Layouts	Optimum parameter values
	η_s	F_{smax}(lb$_\mathrm{F}$)	s_{smax}(ft)		(lb$_\mathrm{F}$/ft, lb$_\mathrm{F}\cdot$s/ft, lb$_\mathrm{m}$)
Default	81.5%	6380.3	0.53	-	-
C1$_{\eta v}$	84.7%(3.9%)	5787.4	0.53	L1	$k_s = 7126.2, c = 796.1$
C2$_{\eta v}$	90.0%(10.4%)	5353.4	0.53	L2	$k_s = 9159.8, c = 519.5, b = 9.4$
C3$_{\eta v}$	92.8%(13.9%)	5248.5	0.50	L3	$k_s = 19492, c = 40715, b = 9.4$
C1$_{Fv}$	81.9%	5581.0(12.5%)	0.53	L1	$k_s = 9043.9, c = 535.2$
C2$_{Fv}$	92.4%	5014.5(21.4%)	0.53	L2	$k_s = 16163, c = 60.21, b = 18.1$
C3$_{Fv}$	92.3%	5003.9(21.6%)	0.53	L3	$k_s = 16927, c = 12171, b = 19.2$
C1$_{sv}$	81.5%	6380.3	0.43(18.9%)	L1	$k_s = 12109.6, c = 772.6$
C2$_{sv}$	88.5%	6380.3	0.37(30.2%)	L2	$k_s = 22794, c = 374.3, b = 19.4$
C3$_{sv}$	83.2%	6380.3	0.39(26.4%)	L3	$k_s = 22755, c = 1471.8, b = 33.3$

[†] % improvements are given in bracket for the criteria being optimised. Same notations apply to other tables in this work.

Table 4.3 Optimisation results with the layout L3 for different damping considering the η_s performance

Layout	Performance			Optimum parameter values		
	η_s (Improvement)	F_{smax}(lb$_\mathrm{F}$)	s_{smax}(ft)	(k_s lb$_\mathrm{F}$/ft)	(c lb$_\mathrm{F}\cdot$s/ft)	(b lb$_\mathrm{m}$)
Default	81.5%(-)	6380.3	0.53	-	-	-
L3	92.8%(13.9%)	5248.5	0.50	19492	40715	9.4
L3	92.4%(13.4%)	5015.2	0.52	17134	10000	19.4
L3	92.0%(12.9%)	5026.8	0.52	16546	5000	20.1
L3	90.2%(10.7%)	5078.4	0.53	14445	1500	24.3
L3	88.6%(8.7%)	5146.0	0.53	13594	1000	28.5

The optimum results for layout LY are summarised in Table 4.4. In contrast to the simpler layouts L1–L3, when fixing k_s, a 14.0% improvement in strut efficiency can be obtained by CY_η. Using relevant network synthesis theory, its mechanical network is realised by a configuration consisting of three dampers, one inerter, one spring and k_s. However, two of the dampers can be removed since their values are small (when in parallel) or large (when in series) compared with the remaining ones. Thus the mechanical layout of CY_η, labelled L4, is a four-element network, as shown in Fig. 4.5. A further optimisation over L4 in which b is removed is carried out but no optimal solution is found. This suggests that the performance improvement obtained by CY_η using L4 requires the inclusion of the inerter. Configuration $\text{CY}_{\eta v}$ provides the maximum improvement in η_s, however a much more complex network, nine-element network excluding k_s, is required. The slight performance improvement compared with CY_η probably does not compensate for the difficulty in design and manufacture of this configuration, hence we disregard it. It can be seen from Table 4.4 that a 21.6% improvement in F_{smax} can be obtained by the configuration CY_F. The network realisation of this transfer function is identified and shown in Fig. 4.5 as layout L5. In this layout, an inerter is in parallel with the supporting stiffness, as well as a combination of two dampers and an internal spring. Note that layout L5 can be reduced to L2 if c_1 in L5 is set to infinity. The similarities of the parameter values between the two configurations, CY_F and $\text{C2}_{\eta v}$, are observed. The maximum performance advantage using F_{smax} as the objective function is obtained by CY_{Fv}, with up to 22.0% improvement. The resulting mechanical network, labelled L6, is illustrated in Fig. 4.5. Note that layouts L5 and L6 consist of five mechanical elements but in different arrangements. As for optimising over s_{smax}, the case with a fixed supporting stiffness, $k_s = \overline{k}_s$, a maximum improvement of only 5.7% is obtained. Allowing k_s to vary results in more complex layouts than L2 and L3 but with no improvements over them. Hence the s_{smax} objective function results are not listed in Table 4.4.

In summary, considering the performance improvements and practical parameter values, we treat $\text{C2}_{\eta v}$ and CY_η as the optimum configurations for the η_s performance, C2_{Fv}, CY_F and CY_{Fv} as the optimum configurations for F_{smax} performance, and C2_{sv} and C3_{sv} as the optimum configurations for s_{smax} performance. Also of interest are $\text{C1}_{\eta v}$, C1_{Fv} and C1_{sv}, as linear configurations in which no inerter is present. The load-stroke curves provided by these configurations, as well as the default one, are compared in Fig. 4.6. Note that the curves in Fig. 4.6 all finish at the end of the compression stroke. The shorter curves in Fig. 4.6(a) and (c) indicate that when the first compression process is finished, the maximum strokes the struts reach are smaller than the baseline system.

Table 4.4 Optimisation results using layout LY

Configurations	Performance			Layouts	Optimum parameter values
	η_s	$F_{smax}(\mathrm{lb_F})$	$s_{smax}(\mathrm{ft})$		$(\mathrm{lb_F/ft},\ \mathrm{lb_F \cdot s/ft},\ \mathrm{lb_m})$
Default	81.5%	6380.3	0.53	-	-
CY_η	92.9%(14.0%)	5187.0	0.50	L4	$k_s = 4884.2, c = 5362.9, k_1 = 15633,$ $b = 19.7$
$\mathrm{CY}_{\eta v}$	93.2%(14.4%)	5266.3	0.49	-	-
CY_F	91.2%	5004.9(21.6%)	0.53	L5	$k_s = 4884.2, c_1 = 3817.1, c_2 = 404.9,$ $b = 9.4, k_1 = 6874.1$
CY_{Fv}	92.0%	4976.5(22.0%)	0.53	L6	$k_s = 8049.2, c_1 = 8492.6, c_2 = 9089.1,$ $b = 20.6, k_1 = 9031.3$

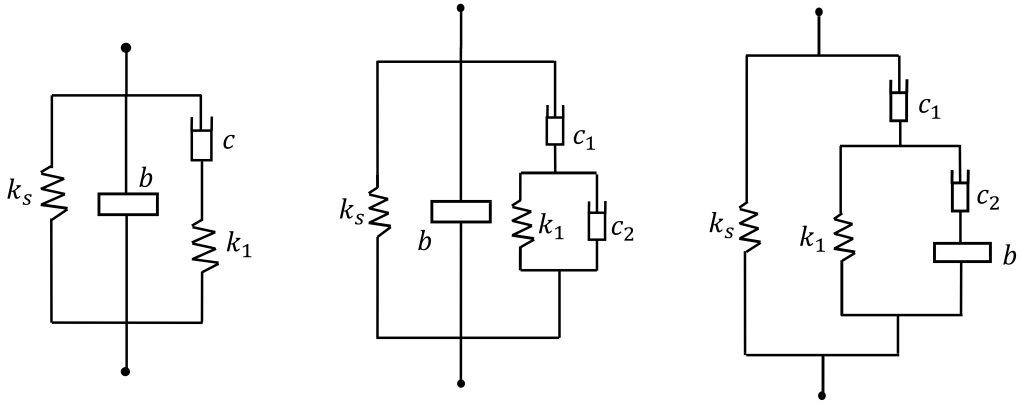

L4 L5 L6

Fig. 4.5 Layouts L4–L6, which corresponds to configurations CY_η, CY_F and CY_{Fv}.

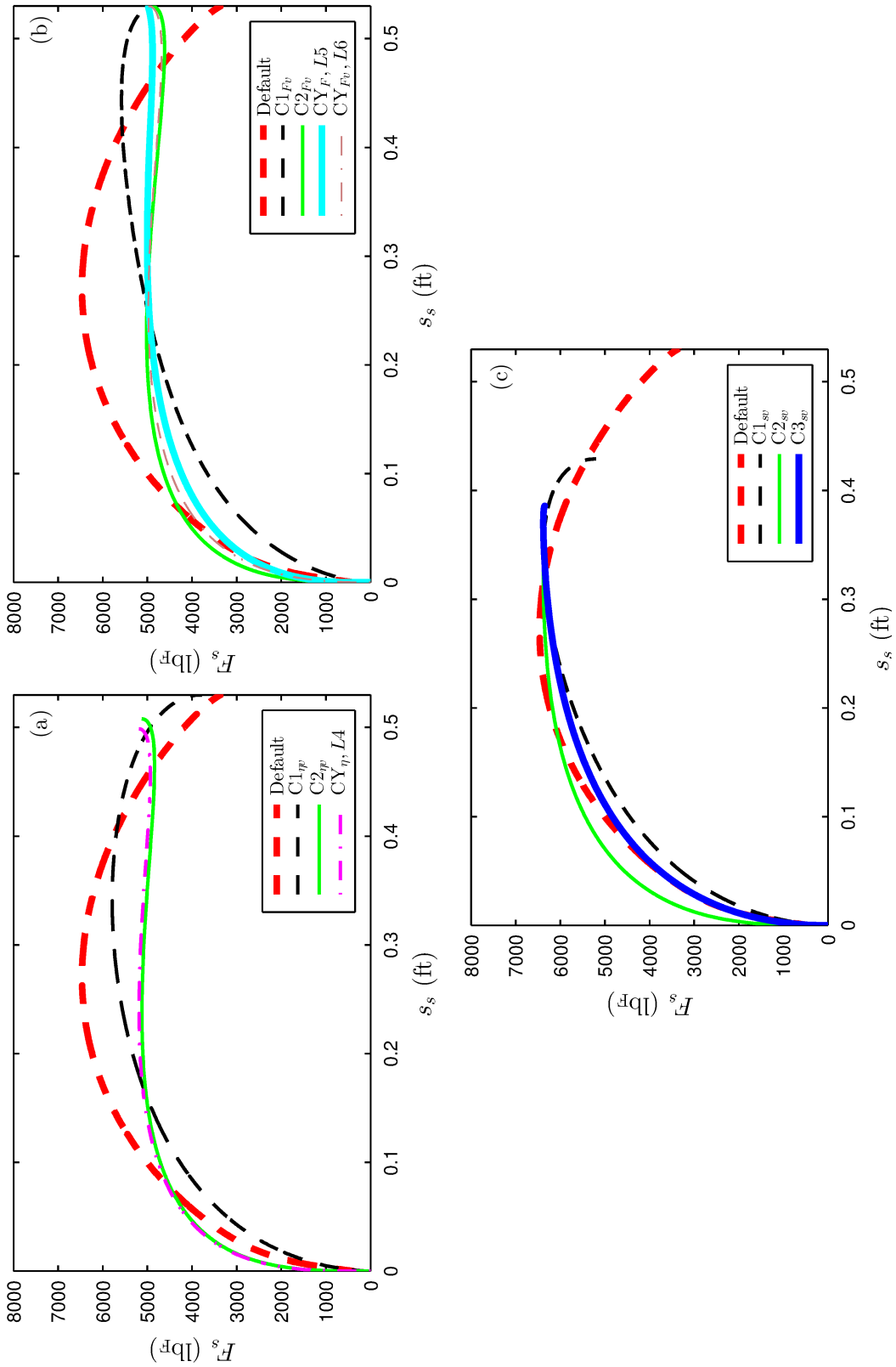

Fig. 4.6 The load-stroke curves improving (a) η_s, (b) F_{smax} and (c) s_{smax}.

4.3.3 Energy analysis of beneficial inerter-based struts

Up to this point, we have considered the energy absorption ability of the strut using η_s. A more detailed investigation into how much energy is dissipated and stored during touch-down process is now presented. The work-energy principle can be applied, to give

$$\Delta E_k + \Delta E_p = W_d + W_L, \tag{4.17}$$

where ΔE_k and ΔE_p represent the change of the kinetic and potential energy in the system, W_d and W_L are the work done by the damper(s) of the strut and the lifting force L, respectively. Here,

$$\Delta E_k = E_k(t_{end}) - E_k(0), \tag{4.18}$$

$$\Delta E_p = -W_1 \cdot z_1(t_{end}) - W_2 \cdot z_2(t_{end}) + E_{pt} + E_{ps}, \tag{4.19}$$

$$W_L = -L \cdot z_1(t_{end}) \tag{4.20}$$

where $E_k(0)$ and $E_k(t_{end})$ denote the kinetic energy of the system just prior to the tyres making contact with the ground and at the end of the compression stroke respectively. E_{pt} and E_{ps} are the potential energy stored in the tyres and the shock struts at the end of the process, respectively. Substituting Eqs. (4.1), (4.2), (4.18), (4.19), and (4.20) into (4.17) gives

$$E_k(0) = E_k(t_{end}) + E_{pt} + E_{ps} - W_d + W_2 \cdot s_s \cdot cos\phi, \tag{4.21}$$

which means the original kinetic energy of the system is transformed partially to the stored potential energy in the tyres and the strut, the work done by the gravity, as well as dissipated by the strut.

Table 4.5 summarises the individual energy distributions by the default nonlinear and optimal shock-strut configurations. Note $E_k(0)$ is not included in the Table since this term is the same for all configurations, $E_k(0) = 3100.5\,\mathrm{lb_F \cdot ft}$. It can be seen that the term $W_2 \cdot s_s \cdot cos\phi$ is small compared with E_{pt}, E_{ps} and $-W_d$. Therefore, Table 4.5 illustrates that the reduced kinetic energy is mostly transformed to the potential energy, stored in the tyres and shock struts, as well as the energy dissipated by the damping effects of the shock strut. It can also be seen that the maximum work done by the dampers $-W_d$ is achieved by $\mathrm{C2}_{\eta v}$, which is still significantly less than that achieved by the the default strut. Moreover, compared with the default configuration, more potential energy is stored in the shock strut, as well as in the tyre compliance. This will pose challenges for the design of the strut elongation process and may even lead to a rebound. Hence an energy dissipation constraint is implemented in the next section.

Table 4.5 Energy distributions of the beneficial configurations

Configurations	$E_k(t_{end})$ $\text{lb}_\text{F} \cdot \text{ft}$	E_{pt} $\text{lb}_\text{F} \cdot \text{ft}$	E_{ps} $\text{lb}_\text{F} \cdot \text{ft}$	$(-W_d)$ $\text{lb}_\text{F} \cdot \text{ft}$	$W_2 \cdot s_s \cdot cos\phi$ $\text{lb}_\text{F} \cdot \text{ft}$
Default	172.5	230.1	353.7	2157.5	67.8
$C1_{\eta v}$	151.8	400.8	955.4	1525.7	67.8
$C2_{\eta v}$	18.3	576.5	1170.3	1268.2	67.8
CY_{η}(L4)	146.7	595.2	1941.6	353.4	67.8
$C1_{Fv}$	73.9	645.9	1212.5	1100.9	67.8
$C2_{Fv}$	172.5	517.5	2156.4	186.7	67.8
CY_{F}(L5)	0.2	722.8	1225.0	1085.1	67.8
CY_{Fv}(L6)	156.0	561.3	2153.5	162.3	67.8
$C1_{sv}$	156.4	760.2	1064.3	1065.1	54.9
$C2_{sv}$	7.0	1076.7	1463.8	540.0	46.8
$C3_{sv}$	0.2	1094.1	1665.2	292.2	49.4

4.4 Optimisation results with an energy dissipation constraint

Further investigations with an extra constraint on energy dissipation are discussed in this section. It will be shown that with this constraint, limited improvements can be provided by the layouts proposed in Section 4.3. The reason for reduced improvements will be discussed. Configurations with a double-stage supporting spring are then proposed, which can achieve significant performance advantages.

4.4.1 Configurations with a linear supporting spring

To ensure good energy dissipation capability, the constraint that the energy dissipation is no less than that by the conventional strut, $2157.5\,\text{lb}_\text{F} \cdot \text{ft}$, is implemented. However, the optimisations found no results if considering $2157.5\,\text{lb}_\text{F} \cdot \text{ft}$ as the energy dissipation constraint directly. This is because a linear spring with $k_s \geq 4884.2$ $\text{lb}_\text{F}/\text{ft}$ is used as the static spring here. Such a spring stores more potential energy at the end of touch-down process than that of the nonlinear spring in the default system. Then with the energy dissipation constrained to be no less than $2157.5\,\text{lb}_\text{F} \cdot \text{ft}$, the total work done by the linear strut is inevitably more than the nonlinear system, resulting in either F_{smax} or s_{smax} exceeding their constraints. Two approaches are considered here to overcome this, firstly the energy dissipation constraint requirement is relaxed by 10% to $1941.8\,\text{lb}_\text{F} \cdot \text{ft}$. Later, in Sections 4.4.2 and 4.4.3, a double-stage static spring is considered. The strut efficiency and the maximum strut load will be used as the objection functions. In addition, k_s is fixed to $\overline{k}_s$ to minimise the potential energy stored in the supporting spring at the end. Note that the maximum stroke will not be optimised since as discussed in Section 4.3.2

the static stiffness is fixed and the maximum improvement is limited to 5.7% (from s_{smax} equals 0.53 ft to 0.50 ft).

For the optimisation, L4–L6 in Fig. 4.5, which can provide performance advantages in η_s and F_{smax}, are used as the candidate layouts (subscripts 'η' and 'F' are used to specify). Since the layout L6 exhibited no improvements in the two objective functions, the optimisation results are not presented here. Considering layouts L4 and L5, the corresponding configurations are labelled C4 and C5. Table 4.6 summarises the performance benefits and parameter values for these configurations. It can be seen that η_s is increased by 9.6% using either $C4_\eta$ or $C5_\eta$ over the default configuration. The optimisation gives $c_2 = 2.4 \times 10^{-11}$ $\mathrm{lb_F \cdot s/ft}$ for $C5_\eta$, suggesting that removing c_2 is possible to simplify this configuration. Hence $C4_\eta$ (row 2) is the most optimum configuration for this case, and its load-stroke curve is plotted in Fig. 4.7(a). Considering F_{smax}, it is found that the maximum benefit over the default configuration is obtained by $C4_F$, with a 9.0% improvement. Again we find that the $C5_F$ configuration simplifies to C4 (as c_2 is small, see row 5 of Table 4.6). The load-stroke curves with the conventional strut and $C4_F$ (row 4) are plotted in Fig. 4.7(b).

Note that in this optimisation case, L1–L3, and L4 with the inerter excluded, do not provide any improvement in η_s or F_{smax} comparing with the baseline system. This suggests that the performance benefits using layout L4 are attributed to the inclusion of the inerter. For both objective functions, the improvements listed in Table 4.6 compared to Table 4.4 are reduced. This is because if we consider the energy dissipation constraint, namely, $(-W_d) \geq 1941.8\,\mathrm{lb_F \cdot ft}$, the total work done by the optimised shock strut here exceeds that of the cases without the energy dissipation constraint. This may lead to a higher F_{smax} and also a worse η_s performance. Rather than considering a minimum energy dissipation constraint of $1941.8\,\mathrm{lb_F \cdot ft}$ (10% less than the default) if we consider $2157.5\,\mathrm{lb_F \cdot ft}$ (5% less), the performance improvement of η_s with the layout L4 is reduced to 5.6%, but with the advantage that the extension stroke is likely to be improved.

Table 4.6 Optimisation results with the linear k_s considering the energy dissipation constraint

Configurations	Performance		Layouts	Optimum parameter values	$(-W_d)$
	η_s	$F_{smax}(\mathrm{lb_F})$		$(\mathrm{lb_F/ft},\ \mathrm{lb_F \cdot s/ft},\ \mathrm{lb_m})$	$(\mathrm{lb_F \cdot ft})$
Default	81.5%	6380.3	-	-	2157.5
$C4_\eta$	89.3%(9.6%)	6070.13	L4	$k_s = 4884.2, c = 1286.1, k_1 = 43351,$ $b = 24.7$	1941.8
$C5_\eta$	89.3%(9.6%)	6111.8	L5	$k_s = 4884.2, c_1 = 1317.6, c_2 = 2.4 \times 10^{-11},$ $b = 25.1, k_1 = 43927$	1941.8
$C4_F$	88.7%	5803.5(9.0%)	L4	$k_s = 4884.2, c = 1043.2, k_1 = 42033,$ $b = 21.8$	1941.8
$C5_F$	88.7%	5803.7(9.0%)	L5	$k_s = 4884.2, c_1 = 1042.4, c_2 = 0.04,$ $b = 21.9, k_1 = 41706$	1941.8

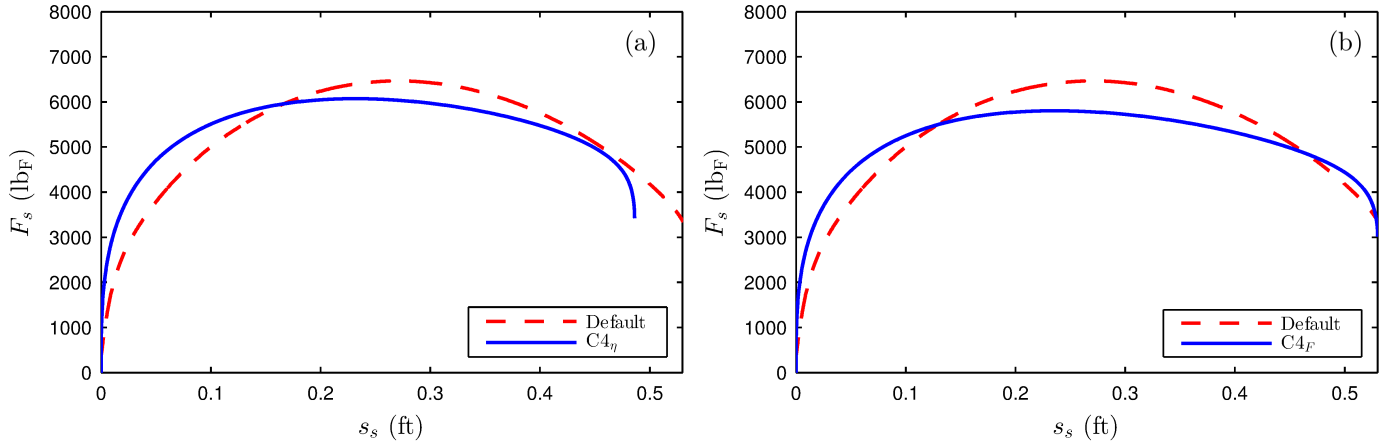

Fig. 4.7 The load-stroke curves obtained with (a) $C4_\eta$ and (b) $C4_F$.

4.4.2 Considering a double-stage supporting spring

Recall that the minimum spring stiffness $k_s = \overline{k}_s$ was selected such that the spring deflection matched that of the air spring when subjected to the aircraft static load. This point is indicated by a red dot in Fig. 4.8. The figure shows the force-deflection relationship for the full compression stroke (up until $s_{smax} = 0.53$ ft). It can be seen that during the compression of the spring the stored energy of the linear spring far exceeds that of the nonlinear device. When the energy dissipation constraint is considered, the limitation of performance benefits is inevitable as discussed in Section 4.4.3.

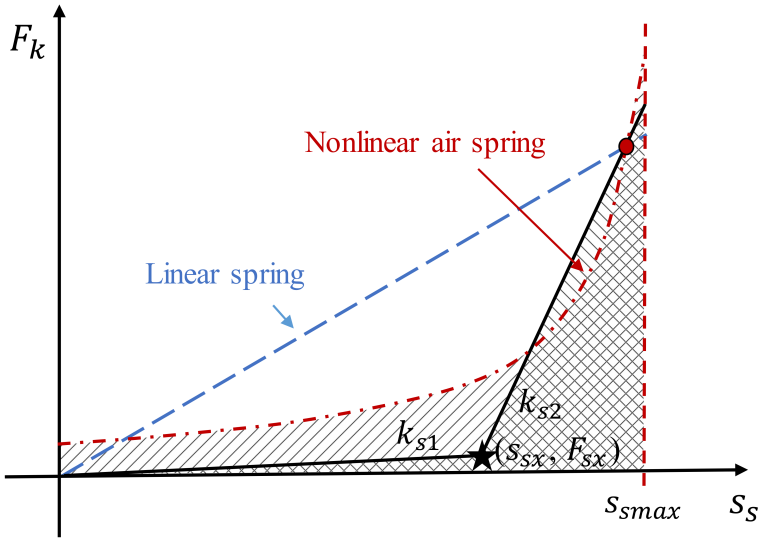

Fig. 4.8 Force-deflection relationships with the air spring and two kinds of k_s.

A supporting spring with a double-stage, or progressive-rate, supporting stiffness is now introduced. The force-stroke relationship of the double-stage spring is given as

$$F_k = \begin{cases} k_{s1} s_s & \text{if } s_s \leq s_{sx} \\ k_{s2}(s_s - s_{sx}) + F_{sx} & \text{if } s_s > s_{sx} \end{cases}$$

where F_k is the supporting spring force, k_{s1} and k_{s2} are the two spring rates. Here s_{sx} and F_{sx} are the stroke and spring force where the two rates intersect in the force-stroke curve and are treated as parameters to be optimised. As with the linear spring k_s, the double-stage one is designed to support the aircraft under the same stoke with the nonlinear air spring. An example force-displacement relationship is shown in Fig. 4.8. From the figure it can been seen that the double-stage supporting spring provides the possibility that its stored potential energy (right-slanted-shading region in Fig. 4.8) could

be less than that by the nonlinear spring (left-slanted-shading region in Fig. 4.8) when reaching the maximum stroke.

4.4.3 Beneficial configurations with double-stage spring

If we use the double-stage spring in the L1 layout, the optimisation can identify considerable improvements in performance, which are 7.6% in η_s by $C1_{\eta 2}$ and 14.1% in F_{smax} by $C1_{F2}$. However, we can not regard these configurations as beneficial ones since the load-stroke curve provided by $C1_{\eta 2}$ or $C1_{F2}$ experiences a sudden change. We take $C1_{\eta 2}$ as an example here. The parameter values of $C1_{\eta 2}$ are summarised in Table 4.7 and the load-stroke curves obtained with the default and $C1_{\eta 2}$ (black line) configurations are illustrated in Fig. 4.9(a). It can be seen that the upper and lower masses will also undergo sudden changes in their accelerations towards the end of the stroke, which will lead to passenger/crew discomfort and additional structural loading. Similar conclusions can be obtained for $C1_{F2}$, as well as the optimisation using L2 and L3. Therefore, we will not include the results of the optimal C1–C3 with a double-stage spring here. Instead, since the layout L4 is regarded as the most optimum layout in the previous optimisation, this layout will be used as an example layout to illustrate the benefits of the double-stage supporting spring. Note that the exact energy dissipation constraint, $(-W_d) \geq 2157.5\,\mathrm{lb_F \cdot ft}$, is considered in this case. The results of optimisation are illustrated in Table 4.7. The subscript '2' is used to specify this case. It can be seen that up to 11.9% improvement in η_s can be obtained using the configuration $C4_{\eta 2}$. Moreover, the layout with different parameter values, i.e. $C4_{F2}$ can also reduce F_{smax} by 20.0% comparing with the default configuration which represents a significant improvement of the 9.0% reduction achieved with the linear spring ($C4_F$, Table 4.6). The load-stroke curves for these two configurations are illustrated in Fig. 4.9. We note that for both cases the first stage stiffness is negligible.

Table 4.7 Optimisation results with the double-stage k_s considering the energy dissipation constraint

Configurations	Performance		Layouts	Optimum parameter values	$(-W_d)$
	η_s	F_{smax}(lbF)		(lbF/ft, lbF · s/ft, lbm)	(lbF · ft)
Default	81.5%	6380.3	-	-	2157.5
C1$_{\eta 2}$	87.7%(7.6%)	5482.0	L1	$k_{s1} = 520.1, k_{s2} = 78344, c = 975.9$	2157.5
C4$_{\eta 2}$	91.2%(11.9%)	5230.7	L4	$k_{s1} = 0.9, k_{s2} = 22011, c = 1060.7,$ $b = 15.4, k_1 = 43697$	2157.5
C4$_{F2}$	90.10%	5101.5(20.0%)	L4	$k_{s1} = 3.1, k_{s2} = 36899, c = 985.1,$ $b = 10.4, k_1 = 53305$	2157.5

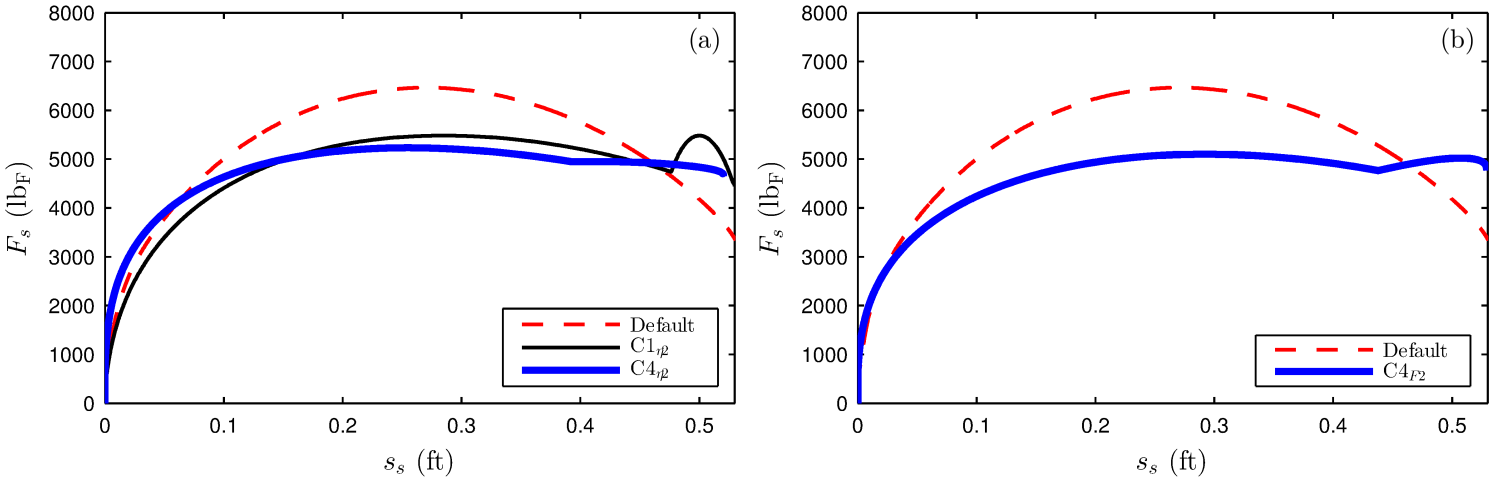

Fig. 4.9 The load-stroke curves obtained with (a) C1$_{\eta 2}$, C4$_{\eta 2}$, and (b) C4$_{F2}$.

4.5 Concluding remarks

In this chapter, we presented a study focusing on suppressing the transient vibrations caused by an initial impact using a passive linear absorber. This was demonstrated using the aircraft landing touch-down process. The benefits of inerter-based shock strut configurations were investigated to improve the performances of the strut efficiency, the maximum strut load and the maximum stroke, considering the energy dissipation constraint. The proposed optimum design approach in this chapter is applicable to other applications experiencing initial impact excitations, such as the design of a forging machine's foundation.

Based on a 2DOF model with the conventional oleo-pneumatic shock absorber, the baseline touch-down performances were obtained aimed at measuring the touch-down performances. Based on the design requirements for the shock absorber, four performance criteria were proposed, where the strut efficiency, the maximum strut load, the maximum strut stroke were considered as the objective functions while the reduction of aircraft kinetic energy at the end of touch-down process as the performance constraint for the optimisations.

Ensuring that the optimum shock struts absorb at least the same level of kinetic energy as the baseline system, the optimisations were carried out. Using the three objective functions, up to 14.0%, 22.0% and 30.2% improvements were obtained with beneficial shock struts over the conventional one, on the strut efficiency, the maximum strut load and the maximum strut stroke, respectively. It was also shown that the inclusion of an inerter led to significant advantages over the non-inerter designs.

We then carried out an energy analysis and it was shown that for the beneficial configurations according to the optimised criteria, more potential energy was unfortunately stored in the strut and via tyre compliance at the end of the strut compression process. This is undesirable since the stored potential energy needs to be released during the elongation stage to pose more challenges and may even lead to a rebound. Hence an energy dissipation constraint was implemented and the beneficial layouts obtained in the previous optimisation were used as the candidate layouts for further optimisations. The objective functions of the strut efficiency and the maximum strut load were considered. However, from the optimisations it was shown that with this additional energy constraint the performance benefits were limited. This was due to the use of a linear supporting spring which stored more potential energy at the end of touch-down over the default nonlinear spring. To ensure the system dissipated at least the same level of energy led to

an increased work done by the strut, giving a worse maximum force or stroke than the default system.

To overcome this, we proposed two approaches, one of which was to relax the energy dissipation constraint, and the other one to use a double-stage supporting spring which could store less potential energy than the nonlinear spring. With a relaxed energy dissipation constraint, the performance improvements were reduced to 9.6% in the strut efficiency and 9.0% in the maximum strut load. Then configurations with double-stage supporting springs were introduced. It was shown that up to 11.9% and 20.0% improvements in the strut efficiency and the maximum strut load were obtained, respectively.

Up to now, we have investigated the suppression of transient behaviour initiated by external perturbations of, i.e. a sudden disturbance in Chapter 3 and initial impact in this chapter. We will move on to considering the stability suppression problem in the next chapter and exploring the issue of the self-excited vibrations.

Chapter 5

Damper optimisation using bifurcation analysis for zero-shimmy stability

5.1 Introduction

This chapter proposes a method of selecting the suppression device parameter values to avoid the instability of self-excited oscillations. The effectiveness of this method is demonstrated using the shimmy problem of a dual-wheel MLG. Based on a nonlinear MLG model, a bifurcation study is carried out to capture the effects of shimmy-suppression devices on the landing gear dynamics via continuation. With the proposed method, the device parameter regions that ensure the aircraft is free from shimmy instability for any forward speed within its operating region are identified. This parameter region is termed as the *zero-shimmy region*, where the straight-rolling solution (zero solution) is stable and no stable LCO shimmy solution. It shows the benefits of one proposed spring-damper configuration on expanding the zero-shimmy regions over the conventional shimmy damper, which facilitate the robustness of shimmy-suppression devices. The potential of further extending such parameter regions are also explored with two inerter-based devices.

The landing gear of any civil aircraft is required to be free from excessive vibrations and any dynamic instabilities over a conservative range of operating conditions [44]. A key source of such vibrations or instabilities is shimmy, which will reduce the structure fatigue life or in some extreme cases, lead to severe structural failure [149]. The first stage of designing suppression devices is normally to establish the parameter region for which no instability exist. Once the region has been identified, the emphasis of the device design shifts to minimising the maximum transient responses due to perturbations, see Chapter 3.

The MLG shimmy dynamics will be analysed using a nonlinear low-order model in this work. Here the tyre will be modelled using the exact stretched-string formulation [150], an extension of the model proposed by Von Schlippe and Dietrich in [151]. For the representation of the landing gear structure, the torsional motion is a vital consideration in capturing the shimmy mechanism, see [142] for example. Since real landing gear systems exhibit various nonlinearities, the nonlinear dynamics of landing gear have attracted significant research interest. In [152, 153], Thota *et al.* investigated the effects of the geometric nonlinearity raised by a non-zero rake angle. They found that a lateral bending motion becomes coupled with the torsional motion.

In this chapter, numerical continuation is used to assess the gear's nonlinear response, which has been shown as a useful tool [154]. Numerical continuation allows one to track the stationary and periodic solution branches, and the quantitative change along such branches, i.e. bifurcation points, as key parameters are varied. The method can be supplemented with time-stepping simulations to fully understand the nonlinear effects on the dynamic stability of the system. A review of bifurcation analysis applied in nonlinear systems can be found in [155] and specific examples focused on aircraft shimmy analysis in [143, 156, 157]. Other analytical analyses have been conducted in the literature to investigate the nonlinear aircraft shimmy problem, based on the techniques of perturbation analysis [158] and the incremental harmonic balance method [159].

In this chapter, we explore the influences of the passive shimmy-suppression devices on the MLG shimmy dynamics via continuation analysis. Firstly a nonlinear mathematical model of a typical MLG configuration reported in [156] is discussed in Section 5.2. The geometry of this MLG is similar with the one used used in Chapter 3, except that a non-zero rake angle is introduced here. Nonlinear coupling between different DOFs and tyre dynamics are also considered. Comparing with the MLG used in Chapter 3, the gear used in this chapter is more likely to be unstable. In Section 5.3, a passive device consisting of a linear spring and damper in parallel (the shimmy damper) is considered first. A bifurcation study is carried out using the continuation software AUTO [160], which is integrated into a Matlab environment via the Dynamical Systems Toolbox [161]. This allows us to identify the device parameter region in which no sustained shimmy oscillations occur over the entire operating speed range – zero-shimmy region. This region in parameter space is shown to be quite narrow when a conventional shimmy damper is used.

To expand this zero-shimmy region then provide a more robust device, a layout which adds a linear spring in series with the shimmy damper is proposed. Its ability in expanding the zero-shimmy region is assessed. It is shown that the use of this proposed spring-damper

configuration can result in a more robust device in terms of the device damping over that of a conventional shimmy damper.

Based on the proposed beneficial spring-damper layout, configurations which include an inerter are considered in Section 5.4, which have TVMD-type and TID-type layouts. The original TVMD and TID layouts have been introduced in Section 2.3.3 while here an extra centering spring is introduced to these original layouts. Further benefits on expanding the zero-shimmy regions are observed in the two-parameter bifurcation diagrams.

Publications resulting from this work

Y. Li, C. Howcroft, S. A. Neild, and J. Z. Jiang, "Using continuation analysis to identify shimmy-suppression devices for an aircraft main landing gear," *Journal of Sound and Vibration*, vol. 408, pp. 234–251, 2017.

5.2 Formulation of nonlinear MLG model

In this section, a typical dual-wheel MLG system reported in [156] is considered and the formulation of a low-order mathematical model of the MLG is presented. The MLG motion is modelled in terms of two DOFs; the gear torsional rotation and the lateral bending. The dynamics of the shimmy-suppression device and elastic tyres are also considered.

5.2.1 Dynamics of a MLG system

A sketch of the dual-wheel MLG is shown in Fig. 5.1 from different views. To capture the nonlinear coupling between different DOFs, two frames are considered here, one is a global frame and the other is a body frame. The global frame $OXYZ$ is fixed to the ground. Similar with Chapter 3, the X axis points in the aircraft direction of travel, the Z axis vertically downwards, and the Y axis completes the right-handed coordinate system. The MLG consists of a main strut, side-stay, torque links, axle assembly connected with two wheels, etc. The top of the MLG is attached to the aircraft fuselage at the point A. We consider a typical orientation of the side-stay here, which is mounted laterally with respect to the main strut and is attached to the fuselage at the point F, as illustrated in Fig. 5.1(a). The main strut, which is inclined to the Z axis by a non-zero rake angle $\phi_{\text{„}}$ is constructed of two cylinders or tubes. To keep the alignment of the wheels, a pair of torque links is employed, with the upper link attached to the upper strut cylinder and

the lower one to the lower cylinder (piston), see Fig. 5.1(b). The end point of the piston is labelled C and the wheel axle is offset from the point C via a caster of length e.

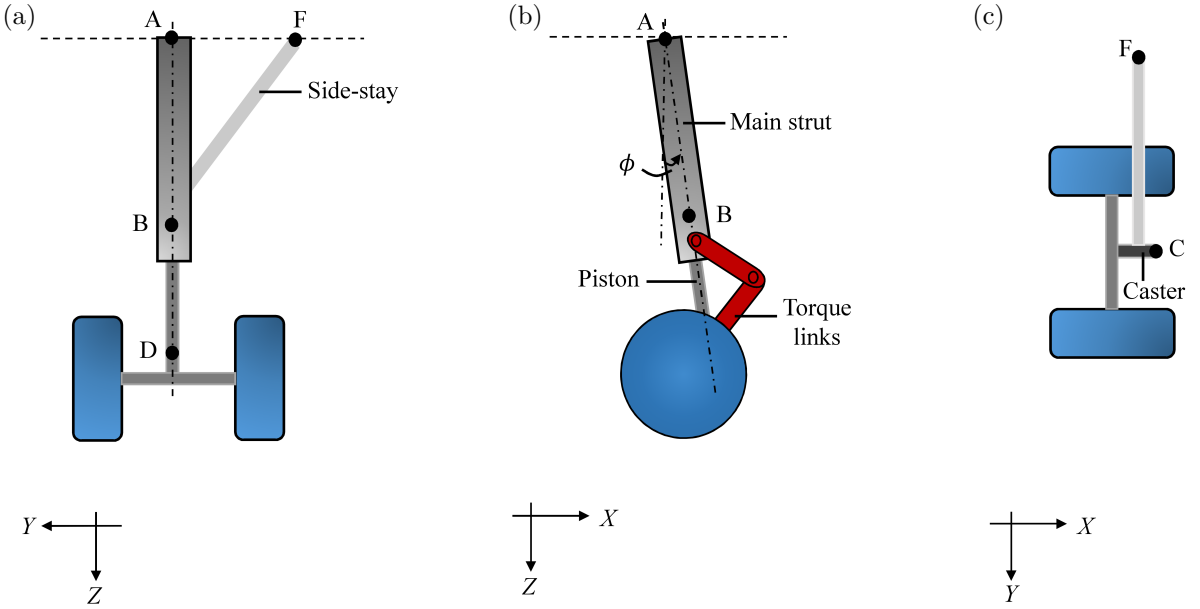

Fig. 5.1 The dual-wheel MLG geometry.

As can be seen from Fig. 5.2(a), the body frame B$\xi\eta\zeta$ is used in order to describe the dynamics of the MLG system in the disturbed state. The axis ζ is rotated from the Z axis along the Y axis by the rake angle ϕ, and is aligned with the strut axis. The axis ξ is parallel with the caster while the axis η completes the right-handed coordinate system. With a radius l_δ, the lower gear is allowed to bend laterally about point B along the ξ axis by the angle δ to represent the lateral compliance of the gear. We consider k_δ and c_δ to capture the structural stiffness and damping of such lateral motion. The gear below point B has a center of gravity located at the point D. The wheel and axle assembly may rotate about the ζ axis with the torsion angle ψ, as shown in Fig. 5.2(b). This represents the rotational compliance of the torque links that span the upper and lower parts of the strut and are present to provide a rotational stiffness k_ψ. A torsional damping c_ψ is also introduced to capture the MLG rotational damping. The MLG is allowed to move vertically and the vertical displacement of point B is z_B. A constraint that the tyres must always contact the ground is assumed. Note that as in [156] we do not consider any axial deflection here. Hence, δ and ψ are the two MLG DOFs.

The shimmy-suppression device is also fitted in the apex location between the upper and lower torque links, as shown in Fig. 5.2(a). As introduced in Section 3.2.1, such device is of translational characteristics but will have equivalent torsional properties. The DOF 'ε' across the device is introduced to represent the equivalent torsional motion of the shimmy-

suppression device. The overall equivalent torque T_ψ generated by torsional damping, torque link stiffnesses and shimmy-suppression device is illustrated in Fig. 5.2(b). As presented in [44, 6] and Section 3.2.1, the torsional stiffness k_ψ is treated as a series connection between the suppression device and the MLG torsional motion. Such MLG torsional mechanism is illustrated in Fig. 5.3(a).

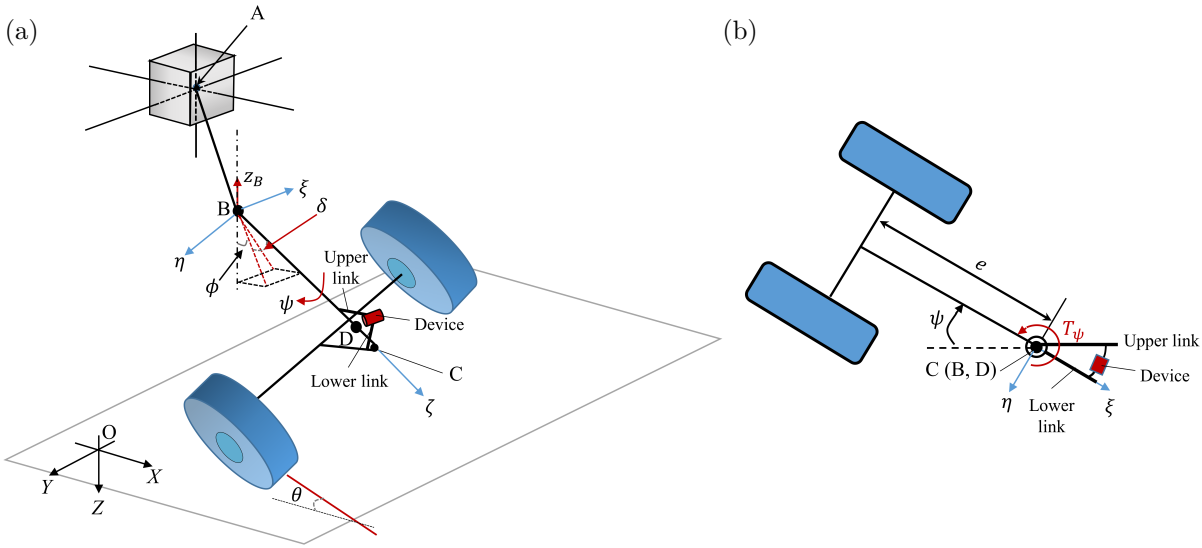

Fig. 5.2 Schematic of (a) the MLG system in the disturbed state and the location of shimmy-suppression device, (b) the ψ degree of freedom in the C$\xi\eta$ plane. The toque T_ψ represents the overall equivalent torque generated by torsional damping, torque link stiffness and shimmy-suppression device.

In this work the MLG mathematical model is established using the Lagrangian method. For each DOF, Lagrange's equation holds,

$$\frac{\partial}{\partial t}\left(\frac{\partial L}{\partial \dot{q}_i}\right) - \frac{\partial L}{\partial q_i} + \frac{\partial D}{\partial \dot{q}_i} = Q_i, \tag{5.1}$$

where L is Lagrangian and $L = T - U$, T and U represent the kinetic and potential energy of the MLG system, respectively. D is Rayleigh's dissipative function, Q_i is the generalised force applied to the MLG system and q_i is the generalised coordinate. When deriving the equations of motion for the system, z_B is temporarily treated as a MLG DOF before being eliminated using a compatibility equation of the tyre-ground contact constraint.

The MLG kinetic energy is

$$T = \frac{1}{2}(m_D|\mathbf{v_D}|^2 + \boldsymbol{\omega_\delta}^T \boldsymbol{J_D} \boldsymbol{\omega_\delta} + \boldsymbol{\omega_\psi}^T \boldsymbol{J_D} \boldsymbol{\omega_\psi}), \tag{5.2}$$

where m_D is the mass of the lower gear (below B), $\boldsymbol{J_D}$ is the inertia matrix at point D in the global frame, $\mathbf{v_D}$ is the velocity vector of the point D, $\boldsymbol{\omega_\delta}$ and $\boldsymbol{\omega_\psi}$ are the angular velocity vectors of the points D (lateral bending motion) and C (torsional motion), respectively. The potential energy is

$$U = \frac{1}{2}(k_\delta \delta^2 + k_\psi(\psi - \varepsilon)^2). \tag{5.3}$$

The ε DOF, representing the motion across the shimmy-suppression device, can be eliminated using a compatibility equation. The torque generated by the shimmy-suppression device T_d is balanced by the torsional spring torque $k_\psi(\psi - \varepsilon)$, as illustrated in Fig. 5.3(a). The expression for T_d is dependent on the device layout. For the shimmy damper layout (labelled L1) shown in Fig. 5.3(b), the compatibility equation is given by

$$T_d = k_d\varepsilon + c_d\dot{\varepsilon} = k_\psi(\psi - \varepsilon), \tag{5.4}$$

where k_d and c_d denote the stiffness and damping of the device. It should be noted that k_d is included and fixed at a default value for all the shimmy-suppression device layouts considered. This is to ensure the gear has sufficient rotational stiffness for centering the gear. The default value of k_d was determined via a scaling calculation based on [6], which is 1.09×10^5 Nm/rad. The Rayleigh's dissipative function is given by

$$D = \frac{1}{2}(c_\delta\dot{\delta}^2 + c_\psi\dot{\psi}^2), \tag{5.5}$$

where c_δ and c_ψ are the damping coefficients of the respective DOF.

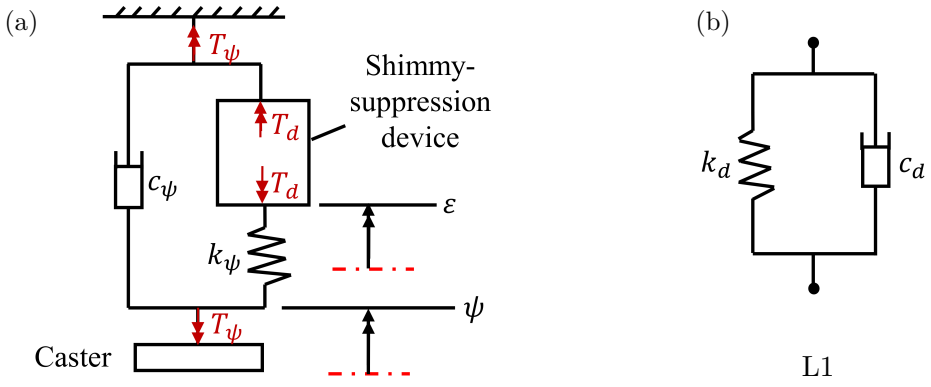

Fig. 5.3 View of (a) the MLG torsional mechanism, (b) the layout of the default shimmy damper.

Now we need to determine the exact expression of T based on Eq. (5.2). We consider all the terms in the global frame, so it is desirable to define the rotation matrix transforming

the vectors from the body frame to the global one. As the global frame can be transformed to the body frame via three rotations ϕ-δ-ψ in sequence, this matrix is given by

$$\boldsymbol{H} = \begin{bmatrix} \cos\phi\cos\psi + \sin\phi\sin\delta\sin\psi & -\cos\phi\sin\psi + \sin\phi\sin\delta\cos\psi & \sin\phi\cos\delta \\ \cos\delta\sin\psi & \cos\delta\cos\psi & -\sin\delta \\ -\sin\phi\cos\psi + \cos\phi\sin\delta\sin\psi & \sin\phi\sin\psi + \cos\phi\sin\delta\cos\psi & \cos\phi\cos\delta \end{bmatrix}. \tag{5.6}$$

The position and velocity vectors of point B in the global frame are given by

$$\boldsymbol{r_B^G} = \begin{bmatrix} Vt \\ 0 \\ -(z_B + L_A - l_B\cos\phi) \end{bmatrix}, \ \boldsymbol{v_B} = \dot{\boldsymbol{r}}_{\boldsymbol{B}}^{\boldsymbol{G}} = \begin{bmatrix} V \\ 0 \\ -\dot{z}_B \end{bmatrix}, \tag{5.7}$$

where V is the aircraft forward speed, t is the time, L_A is the MLG height, and l_B is the distance from points A to B. The position vector of point D in the body frame is given by

$$\boldsymbol{r_{BD}^b} = \begin{bmatrix} 0 \\ 0 \\ l_D \end{bmatrix}, \tag{5.8}$$

where l_D is the distance from B to D. Then, we obtain the position and velocity vectors of point D in the global frame by

$$\boldsymbol{r_D^G} = \boldsymbol{r_B^G} + \boldsymbol{H}\boldsymbol{r_{BD}^b}, \quad \boldsymbol{v_D} = \dot{\boldsymbol{r}}_{\boldsymbol{D}}^{\boldsymbol{G}}. \tag{5.9}$$

Due to the sequenced rotations applied from global to body frames, the two angular velocity vectors may be written as

$$\boldsymbol{\omega_\delta} = \begin{bmatrix} \dot{\delta}\cos\phi \\ 0 \\ -\dot{\delta}\sin\phi \end{bmatrix}, \ \boldsymbol{\omega_\psi} = \begin{bmatrix} \dot{\psi}\cos\delta\sin\phi \\ -\dot{\psi}\sin\delta \\ -\dot{\psi}\cos\phi\cos\delta \end{bmatrix}. \tag{5.10}$$

The inertia matrix tensor is given by

$$\boldsymbol{J_D^b} = \begin{bmatrix} J_{D\xi\xi}^b & 0 & 0 \\ 0 & J_{D\eta\eta}^b & 0 \\ 0 & 0 & J_{D\zeta\zeta}^b \end{bmatrix}, \tag{5.11}$$

where J^b_{DWW} represents the moment of inertia at point D with respect to W axis of the body frame. Hence, the inertia matrix tensor in the global frame can be given by

$$\boldsymbol{J}_{\boldsymbol{D}}^{\boldsymbol{G}} = \boldsymbol{H}\boldsymbol{J}_{\boldsymbol{D}}^{\boldsymbol{b}}\boldsymbol{H}^T. \tag{5.12}$$

Fig. 5.4 shows the external forces applied to the MLG system. There is a vertical force F_N acting on the point B and the gravitational force at point D, giving

$$\boldsymbol{F_B} = \begin{bmatrix} 0 \\ 0 \\ F_N \end{bmatrix}, \ \boldsymbol{G_D} = \begin{bmatrix} 0 \\ 0 \\ m_D g \end{bmatrix}, \tag{5.13}$$

where $F_N = Mg$, M is the mass of the fuselage and the upper part of the MLG (that above point B), and g is the gravitational constant. At the ground-tyre contact points, there are vertical forces $\boldsymbol{F_{zi}}$ and lateral forces $\boldsymbol{F_{yi}}$, where $i = L$ or R represents the force applied to the left or right tyre. These are given by

$$\boldsymbol{F_{zi}} = \begin{bmatrix} 0 \\ 0 \\ -F_{zi} \end{bmatrix}, \ \boldsymbol{F_{yi}} = \begin{bmatrix} -F_{zi}\Lambda_i \sin\theta \\ F_{zi}\Lambda_i \cos\theta \\ 0 \end{bmatrix}, \tag{5.14}$$

where F_{zi} is the magnitude of $\boldsymbol{F_{zi}}$, $\theta = \psi \cos\phi \cos\delta$ is the angle between the wheel actual travelling direction and the X axis. The expression of the coefficient Λ_i is dependent on the tyre model and will be given in Section 5.2.2. The vertical forces are given by

$$F_{zL} = \frac{1}{2}(-a\mu k_t + F_z), \quad F_{zR} = \frac{1}{2}(a\mu k_t + F_z), \tag{5.15}$$

where k_t is the tyre vertical stiffness, F_z is the total vertical force acting on the MLG from the ground, and a is the track width, as illustrated in Fig. 5.4. The angle μ is given by

$$\mu = \sin^{-1}(\sin\phi \sin\psi + \cos\phi \sin\delta \cos\psi). \tag{5.16}$$

Apart from the forces, the tyres also experience self-aligning moments $\boldsymbol{M_{ki}}$, as given by

$$\boldsymbol{M_{ki}} = \begin{bmatrix} 0 \\ 0 \\ -C_{ki}F_{zi} \end{bmatrix}, \tag{5.17}$$

where C_{ki} will be given in Section 5.2.2. The velocity vectors at ground-tyre contact points E_i are also needed for the calculation of the generalised forces. The positions of E_i in the body frame are given by

$$\boldsymbol{r}^{\boldsymbol{b}}_{\boldsymbol{BEi}} = \begin{bmatrix} -(e + R_i \sin\phi) \\ \mp\frac{a}{2} \\ l_\delta + R_i \cos\phi \end{bmatrix}, \tag{5.18}$$

where R_i is loaded radius of the left/right tyre. R_i can be expressed by

$$R_i = R - 0.2d_i, \tag{5.19}$$

where R is the tyre unloaded radius, $d_i = \mp\frac{1}{2}a\mu$, which represents the tyre deflections (see Daugherty [162]). Then, the position and velocity vectors can be calculated by

$$\boldsymbol{r}^{\boldsymbol{G}}_{\boldsymbol{Ei}} = \boldsymbol{r}^{\boldsymbol{G}}_{\boldsymbol{Bi}} + \boldsymbol{H}\boldsymbol{r}^{\boldsymbol{b}}_{\boldsymbol{BEi}}, \quad \boldsymbol{v_{Ei}} = \dot{\boldsymbol{r}}^{\boldsymbol{G}}_{\boldsymbol{Ei}}. \tag{5.20}$$

Thus, the generalised force for each coordinate is calculated by

$$Q_i = \boldsymbol{F_B} \cdot \frac{\partial \boldsymbol{v_B}}{\partial \dot{q}_i} + \boldsymbol{G_D} \cdot \frac{\partial \boldsymbol{v_D}}{\partial \dot{q}_i} + \sum_{i=L,R} (\boldsymbol{F_{yi}} + \boldsymbol{F_{zi}}) \cdot \frac{\partial \boldsymbol{v_{Ei}}}{\partial \dot{q}_i} + \sum_{i=L,R} \boldsymbol{M_{ki}} \cdot \frac{\partial(\boldsymbol{\omega_\delta} + \boldsymbol{\omega_\psi})}{\dot{q}_i}. \tag{5.21}$$

This completes the set of terms needed for Eq. (5.1).

As previously mentioned, the ground-contact constraint ensures the MLG always contacts the ground. Therefore, the velocities of the contact points in the vertical direction should equal 0, giving

$$v_{Ei.Z} = \dot{z}_B - \dot{r}_{BEi.Z} = 0, \tag{5.22}$$

where $v_{Ei.Z}$ and $\dot{r}_{BEi.Z}$ are the Z components of $\boldsymbol{v_{Ei}}$ and $\dot{\boldsymbol{r}}^{\boldsymbol{G}}_{\boldsymbol{BEi}}$ ($\boldsymbol{r}^{\boldsymbol{G}}_{\boldsymbol{BEi}} = \boldsymbol{H}\boldsymbol{r}^{\boldsymbol{b}}_{\boldsymbol{BEi}}$), respectively. Therefore, to satisfy this constraint for the two contact points, we have

$$\dot{z}_{BL} = \dot{r}_{BEL.Z}, \tag{5.23}$$

$$\dot{z}_{BR} = \dot{r}_{BER.Z}. \tag{5.24}$$

5.2.2 Tyre model

The exact stretched-string model detailed in [150] is used here to capture the tyre dynamics, and will be discussed in two parts. The first part involves the forces applied

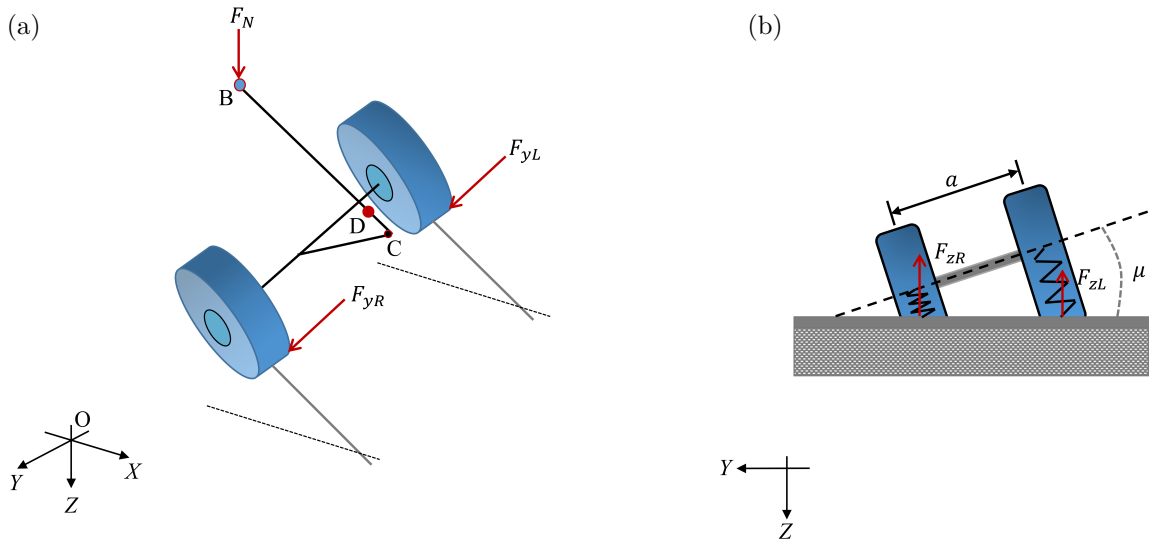

Fig. 5.4 View of (a) the general forces applied to the MLG, (b) the vertical forces acting at the ground contact points of the two wheels.

to the MLG, i.e., the lateral forces $\boldsymbol{F_{yi}}$ and the self-aligning moments $\boldsymbol{M_{ki}}$. According to the tyre model, to capture these forces, the definitions of coefficients Λ_i and C_{ki} need to be provided, written as

$$\Lambda_i = k_\lambda \tan^{-1}(7 \tan \alpha_i \cos(0.95 \tan^{-1}(7 \tan \alpha_i))), \tag{5.25}$$

and

$$C_{ki} = \begin{cases} k_\alpha \frac{\alpha_m}{\pi} \sin(\alpha_i \frac{\pi}{\alpha_m}) & \text{if } |\alpha_i| \leq \alpha_m \\ 0 & \text{if } |\alpha_i| > \alpha_m \end{cases}, \tag{5.26}$$

where k_λ is the tyre restoring coefficient, $\alpha_i = \tan^{-1}(\frac{\lambda_i}{l})$ is the tyre slip angle and l is the tyre relaxation length. In Eq. (5.26), k_α is the tyre self-aligning coefficient and α_m is the maximum slip angle. These definitions are taken from [153].

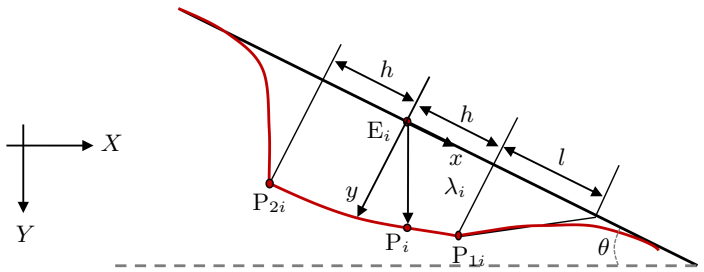

Fig. 5.5 The stretched-string tyre model and the tyre deformation λ_i.

The second part relates to the tyre dynamics at the ground-tyre contact plane. As shown in Fig. 5.5, the local tyre frame $\mathrm{E}_i xy$ is used and the actual shape of the tyre contact line is defined by a function $\mathrm{P}_i(x,t)$, $x \in [-h, h]$, where $2h$ is the contact patch length. Consider a point P_i between the leading and trailing points (P_1 and P_2, respectively) of the contact patch, it has a lateral deformation $y_i(x,t)$ along y axis. Then the absolute position of the point P_i is given by

$$\boldsymbol{r}_{\boldsymbol{Pi}}^{\boldsymbol{G}} = \boldsymbol{r}_{\boldsymbol{Ei}}^{\boldsymbol{G}} + \boldsymbol{r}_{\boldsymbol{EPi}}^{\boldsymbol{G}} = \begin{bmatrix} r_{Ei.X} + x\cos\theta - y_i(x,t)\sin\theta \\ r_{Ei.Y} + x\sin\theta + y_i(x,t)\cos\theta \\ r_{Ei.Z} \end{bmatrix}, \tag{5.27}$$

where $r_{Ei.X}$, $r_{Ei.Y}$ and $r_{Ei.Z}$ denote the X, Y and Z components of the vector $\boldsymbol{r}_{\boldsymbol{Ei}}^{\boldsymbol{G}}$. Then its velocity vector is given by

$$\boldsymbol{v}_{\boldsymbol{Pi}} = \dot{\boldsymbol{r}}_{\boldsymbol{Pi}}^{\boldsymbol{G}} = \begin{bmatrix} v_{Ei.X} + \dot{x}\cos\theta - \dot{\theta}x\sin\theta - \dot{\theta}y_i\cos\theta - (\dot{y}_i + \frac{\partial y_i}{\partial x}\dot{x})\sin\theta \\ v_{Ei.Y} + \dot{x}\sin\theta + \dot{\theta}x\cos\theta - \dot{\theta}y_i\sin\theta + (\dot{y}_i + \frac{\partial y_i}{\partial x}\dot{x})\cos\theta \\ v_{Ei.Z} \end{bmatrix}, \tag{5.28}$$

where $v_{Ei.X}$, $v_{Ei.Y}$ and $v_{Ei.Z}$ denote the X, Y and Z components of the vector $\boldsymbol{v}_{\boldsymbol{Ei}}^{\boldsymbol{G}}$.

Assuming the tyres are fully adhered to the ground leads to a zero velocity condition at the point P_i, whereby each component of the vector $\boldsymbol{v}_{\boldsymbol{pi}}$ equals 0. Further algebraic manipulation gives

$$\dot{y}_i = v_{Ei.X}\sin\theta - v_{Ei.Y}\cos\theta - x\dot{\theta} - \frac{\partial y_i}{\partial x}(\dot{\theta}y_i - v_{Ei.X}\cos\theta - v_{Ei.Y}\sin\theta). \tag{5.29}$$

The slope at P_{1i} is related to the lateral deformation of the leading point λ_i by the approximation

$$\frac{\partial y_i(h,t)}{\partial x} = -\frac{\lambda_i}{l}. \tag{5.30}$$

Substitution of Eq. (5.30) into Eq. (5.29) gives

$$\dot{\lambda}_i = v_{Ei.X}(\sin\theta - \frac{\lambda_i}{l}\cos\theta) - v_{Ei.Y}(\cos\theta + \frac{\lambda_i}{l}\sin\theta) - (h - \frac{\lambda_i^2}{l})\dot{\theta}. \tag{5.31}$$

5.2.3 Equations of motion

The equations of motion of the MLG system for $q_i = \delta, \psi$ and z_B are now written in the compact form

$$N_{11}^{\delta}\ddot{\delta} + N_{12}^{\delta}\ddot{z}_B + N_{21}^{\delta}\dot{\delta}^2 + N_{22}^{\delta}\dot{\delta}\dot{\psi} + N_3^{\delta}\dot{\delta} + N_4^{\delta}\delta + N_{5L}^{\delta}F_{zL} + N_{5R}^{\delta}F_{zR} + N_6^{\delta} = 0, \quad (5.32)$$

$$N_1^{\psi}\ddot{\psi} + N_{21}^{\psi}\dot{\delta}^2 + N_3^{\psi}\dot{\psi} + T_d + N_{5L}^{\psi}F_{zL} + N_{5R}^{\psi}F_{zR} = 0, \quad (5.33)$$

$$N_{11}^{z}\ddot{z}_B + N_{12}^{z}\ddot{\delta} + N_{21}^{z}\dot{\delta}^2 - F_{zL} - F_{zR} + m_D g + F_N = 0. \quad (5.34)$$

Via necessary substitutions, we obtain

$$F_{zL} = \frac{1}{2}(-a\mu k_t + N_{11}^{z}\ddot{z}_{BL} + N_{21}^{z}\dot{\delta}^2 + m_D g + F_N), \quad (5.35)$$

$$F_{zR} = \frac{1}{2}(a\mu k_t + N_{11}^{z}\ddot{z}_{BR} + N_{21}^{z}\dot{\delta}^2 + m_D g + F_N), \quad (5.36)$$

where $\ddot{z}_{Bi}$ is obtained via differentiation of the two constraints Eqs. (5.23) and (5.24). The expression of the shimmy-suppression dynamics, given by Eq. (5.4), is specific to the type of the device considered. Hence, the three second-order differential equations Eqs. (5.32)–(5.34), the first-order differential equation Eq. (5.31) for tyres, along with Eq. (5.4), complete the equations of motion for the MLG system.

The coefficients N_{aa}^{b} for the equations of motion are given as follows. For Eq. (5.32),

$$\begin{aligned}
N_{11}^{\delta} &= J_{D\xi\xi}^{b} + (J_{D\xi\xi}^{b} - J_{D\eta\eta}^{b})\cos^2\psi + m_D L_D^2 \cos^2\delta,\\
N_{12}^{\delta} &= m_D l_D \cos\phi \sin\delta, \quad N_{21}^{\delta} = L_D^2(1-2m_D)\cos\delta\sin\delta,\\
N_{22}^{\delta} &= -2(J_{D\xi\xi}^{b} - J_{D\eta\eta}^{b})\cos\psi\sin\psi, \quad N_3^{\delta} = c_\delta, \quad N_4^{\delta} = k_\delta,\\
N_{5i}^{\delta} &= N_{5i1}^{\delta}(-e - R_i\sin\phi) + N_{5i2}^{\delta}(l_\delta + R_i\cos\phi) \mp \frac{1}{2}aN_{5i3}^{\delta} + C_{ki}\sin\phi,\\
N_6^{\delta} &= l_D m_D g \sin\delta\cos\phi,
\end{aligned}$$

where $i = L/R$ and

$$\begin{aligned}
N_{5i1}^{\delta} &= \Lambda_i \sin\psi(\sin\phi\cos\delta\sin\theta + \sin\delta\cos\theta) + \cos\phi\cos\delta\sin\psi,\\
N_{5i2}^{\delta} &= \Lambda_i(-\sin\phi\sin\delta\sin\theta + \cos\delta\cos\theta) - \cos\phi\sin\delta,\\
N_{5i3}^{\delta} &= -\Lambda_i\cos\psi(\sin\phi\cos\delta\sin\theta + \sin\delta\cos\theta) - \cos\delta\cos\psi\cos\phi.
\end{aligned}$$

Table 5.1 Parameters values used in the analysis

Symbol	Parameter	Value
	MLG parameter	
a	Track width	0.5 m
c_δ	Lateral damping of the strut	300 Nms/rad
c_ψ	Torsional damping of the wheel assembly	300 Nms/rad
e	Caster length	0.12 m
k_δ	Lateral stiffness of the strut	6.1×10^6 Nm/rad
k_ψ	Effective torsional stiffness of the torque links	3.8×10^5 Nm/rad
$J^b_{D\xi\xi}$	Moment of inertia at D with respect to ξ axis	200 kgm^2
$J^b_{D\eta\eta}$	Moment of inertia at D with respect to η axis	250 kgm^2
$J^b_{D\zeta\zeta}$	Moment of inertia at D with respect to ζ axis	100 kgm^2
l_D	Distance from B to D	0.72 m
l_δ	Radius of lateral bending motion	0.75 m
m_D	Mass of the MLG bending part	500 kg
ϕ	MLG rake angle	0.0524 rad (3°)
	Tyre parameter	
h	Half of contact patch length	0.1 m
k_t	Tyre vertical stiffness	7.0×10^5 N/m
k_α	Tyre self-aligning coefficient	1.0 m
k_λ	Tyre restoring coefficient	0.002 /rad
l	Relaxation length	0.3 m
R	Tyre unloaded radius	0.362 m
α_m	Maximum slip angle	0.1745 rad
	Shimmy-suppression device parameter	
k_d	Device stiffness	1.09×10^5 Nm/rad
	Other	
g	Gravitational constant	9.81 m/s^2
M	Mass of the fuselage and the upper MLG	19.9 t

For Eq. (5.33),

$$N_1^{\psi} = J_{D\zeta\zeta}^b, \quad N_{21}^{\psi} = (J_{D\xi\xi}^b - J_{D\eta\eta}^b)\cos\psi\sin\phi, \quad N_3^{\psi} = c_{\psi},$$
$$N_{5i}^{\psi} = N_{5i1}^{\psi}(-e - R_i\sin\phi) + N_{5i2}^{\psi}(l_\delta + R_i\cos\phi) \mp \frac{1}{2}aN_{5i3}^{\psi} - C_{ki}\cos\phi\cos(\delta),$$

where $i = L/R$ and

$$N_{5i1}^{\psi} = \Lambda_i\sin\theta(\sin\phi\sin\delta\cos\psi - \sin\psi\cos\phi) + \cos\phi\sin\delta\cos\psi + \sin\phi\sin\psi,$$
$$N_{5i2}^{\psi} = -\Lambda_i\cos\phi\cos\delta\cos\theta,$$
$$N_{5i3}^{\psi} = -\Lambda_i(\cos\delta\sin\psi\cos\theta - \sin\theta(\cos\phi\cos\psi + \sin\phi\sin\delta\sin\psi)) + \sin\phi\cos\psi$$
$$- \cos\phi\sin\delta\sin\psi.$$

For Eq. (5.34),

$$N_{11}^z = m_D, \quad N_{12}^z = m_D l_D\cos\phi sin\delta, \quad N_{21}^z = m_D l_D\cos\phi\cos\delta.$$

The parameter values shown in Table 5.1 are used for the MLG system and are mostly taken from [156]. Similar one- and two-parameter bifurcation diagrams with those in [156], for example, Figures 9 and 10, are obtained with the presented model without installing the shimmy-suppression device here. Hence, this model is validated for a further analysis. The stiffness for the shimmy-suppression device, k_d, is calculated via the scaling analysis based on [6]. Note that all the parameters in Table 5.1 are fixed in the following discussions.

5.3 Analysis of non-inerter shimmy-suppression devices

Using the model presented in Section 5.2, the influence of two shimmy-suppression devices on MLG dynamics are investigated in this section, the first of which is the traditional shimmy-suppression device, the shimmy damper, shown in Fig. 5.3(b). Its effects on the MLG dynamic stability are studied via continuation. The continuation approach allows the region in parameter space in which no unstable solutions exist at any velocity within the operating range, the zero-shimmy region, to be identified. This is achieved via two-parameter bifurcation analysis in terms of forward velocity V and shimmy-suppression device damping c_d. The second proposed device comprises a spring-damper layout and the influence of this configuration on expanding the zero-shimmy region is explored. This zero-shimmy region, in which no sustained oscillations exist, has previously been studied

in terms of operating conditions, see for example [163, 164]. Here it is considered also in terms of device parameter values.

5.3.1 The default shimmy damper

In this subsection, the effects of a shimmy damper are analysed. The device stiffness k_d is fixed to 1.09×10^5 Nm/rad and the influence of the device damping c_d on the MLG shimmy dynamic behaviour is investigated using time-stepping method. Then, choosing the aircraft forward speed as the continuation parameter while setting c_d to three example values, one-parameter bifurcation diagrams are constructed showing both the stability of the MLG straight-rolling and LCO solutions within a certain range of speeds. After that, we treat c_d as a second continuation parameter and the resulting two-parameter bifurcation diagram is given in the parameter plane of the MLG forward speed and c_d. Regions in which different types of shimmy oscillations occur as well as stable zero-shimmy behaviour are identified in this parameter space.

Examples of shimmy oscillations

Figure. 5.6(a) shows the MLG time series response for $V = 20$ m/s and (b) for $V = 40$ m/s when $c_d = 3.6 \times 10^4$ Nms/rad. After applying a perturbation to the zero-shimmy state, the MLG is found to oscillate and settle down to a periodic solution, shown in the figure in terms of the torsional motion ψ, lateral bending motion δ^* and tyre deflection λ. Here, δ^* represents the resulting deflection of δ DoF at the point C and λ is the time history of λ_L or λ_R since the left/right tyre experiences the same deflection in the ground contact plane. It can be seen from Fig. 5.6(a) that the maximum deflection angle of ψ is 3.7 degrees while the maximum amplitude of δ^* is only of the order of 10^{-4} m. Hence, we define the solution as a kind of torsional-dominated shimmy (we refer to this as ψ-shimmy). Similarly, we observe that the response in Fig. 5.6(b) is dominated by the lateral bending motion and hence is referred to as δ-shimmy.

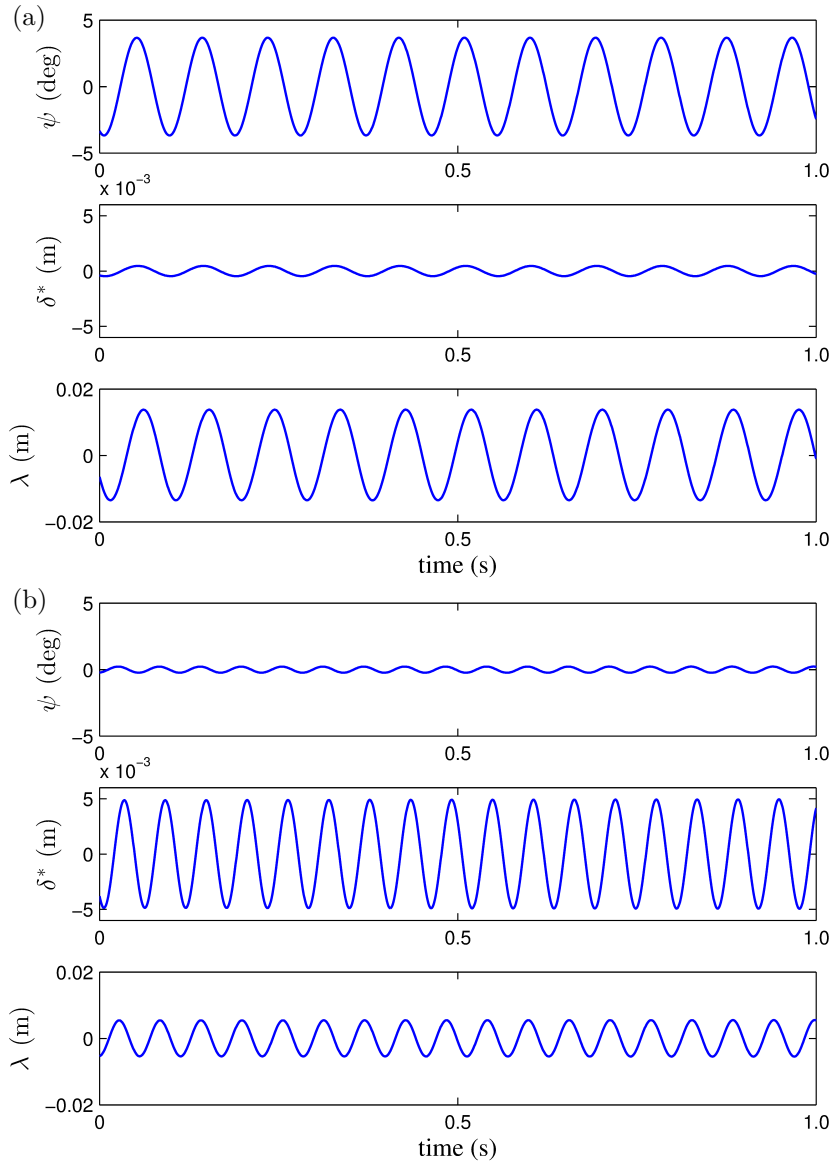

Fig. 5.6 Time histories of the MLG with $c_d = 3.6 \times 10^4$ Nms/rad experiencing (a) ψ-shimmy for $V = 20$ m/s and (b) δ-shimmy for $V = 40$ m/s.

One-parameter continuation

From Fig. 5.6, it can be observed that for a given set of parameter values, the system may experience different types of shimmy oscillations at different velocities. It is also true that for a given velocity the MLG can exhibit different periodic solutions with different initial conditions of the system. However, traditional time-stepping simulation methods have the limitation that they cannot systematically identify all periodic solutions for a given set of parameter values. Therefore, a bifurcation study is conducted here to

investigate the topology of multiple MLG straight-rolling and LCO solutions; see [165] as an example for details of bifurcation theory.

A one-parameter bifurcation analysis is now performed with the aircraft forward speed V as the continuation parameter. Fig. 5.7(a) shows with respect to V the maximum amplitudes of MLG periodic solutions in terms of torsional motion ψ and lateral bending motion δ^* when $c_d = 3.6 \times 10^4$ Nms/rad. Here, δ^* represents the resulting deflection of δ DOF at the point C. The stable solutions are represented by blue solid lines and unstable by red dashed ones. At low forward speeds, the straight-rolling solution is observed, which represents zero shimmy. When V is 13.4 m/s, the zero-shimmy solution loses stability and shimmy occurs. This qualitative change in behaviour is due to a Hopf bifurcation (labelled H) corresponding to a pair of complex conjugate eigenvalues crossing the imaginary axis in the complex plane; this gives birth to a periodic solution. This periodic branch ends with another Hopf point at $V = 33.8$ m/s. Along this branch, stability is changed at $V = 30.8$ m/s, with the existence of a torus bifurcation point (labelled T), resulting from a pair of complex eigenvalues with unit modulus. Note that for $V = 20$ m/s (point A in Fig. 5.7(a)) the maximum deflection angle of ψ is 3.7 degrees while the maximum amplitude of δ^* is only of the order of 10^{-4} m. It can be observed that along this branch the maximum deflection angle of ψ is always more significant than that of δ^*. Hence this branch represents ψ-shimmy. Moreover, there is another branch of periodic solutions which is connected by a further pair of Hopf bifurcation points. Following this branch, initially the solution is unstable but regains stability when a torus point is traversed at $V = 27.4$ m/s. Similarly, we observe that the response in this branch is dominated by the lateral bending motion, see $V = 40$ m/s (point B in Fig. 5.7(a)) as an example, and hence is referred to as δ-shimmy. Note that there is a velocity region bounded by the two torus bifurcations, where both branches are stable; within this bistable region the initial perturbation determines which solution branch will be observed. Figs. 5.7(b) and (c) show one-parameter bifurcation diagrams for smaller device damping: (b1) and (b2) for $c_d = 5.0 \times 10^3$ Nms/rad; (c1) and (c2) for $c_d = 2.0 \times 10^3$ Nms/rad. In contrast to the results shown in Fig. 5.7(a), for both cases, only one branch is observed and along this branch the solutions are stable. Since the δ-component is more significant in Fig. 5.7(b), the branch is δ-shimmy while that shown in (c) is a ψ-shimmy branch.

Two-parameter continuation

As observed in Fig. 5.7, the device damping c_d plays a significant role in the MLG dynamic behaviour. Hence, in order to investigate the influence of the device damping

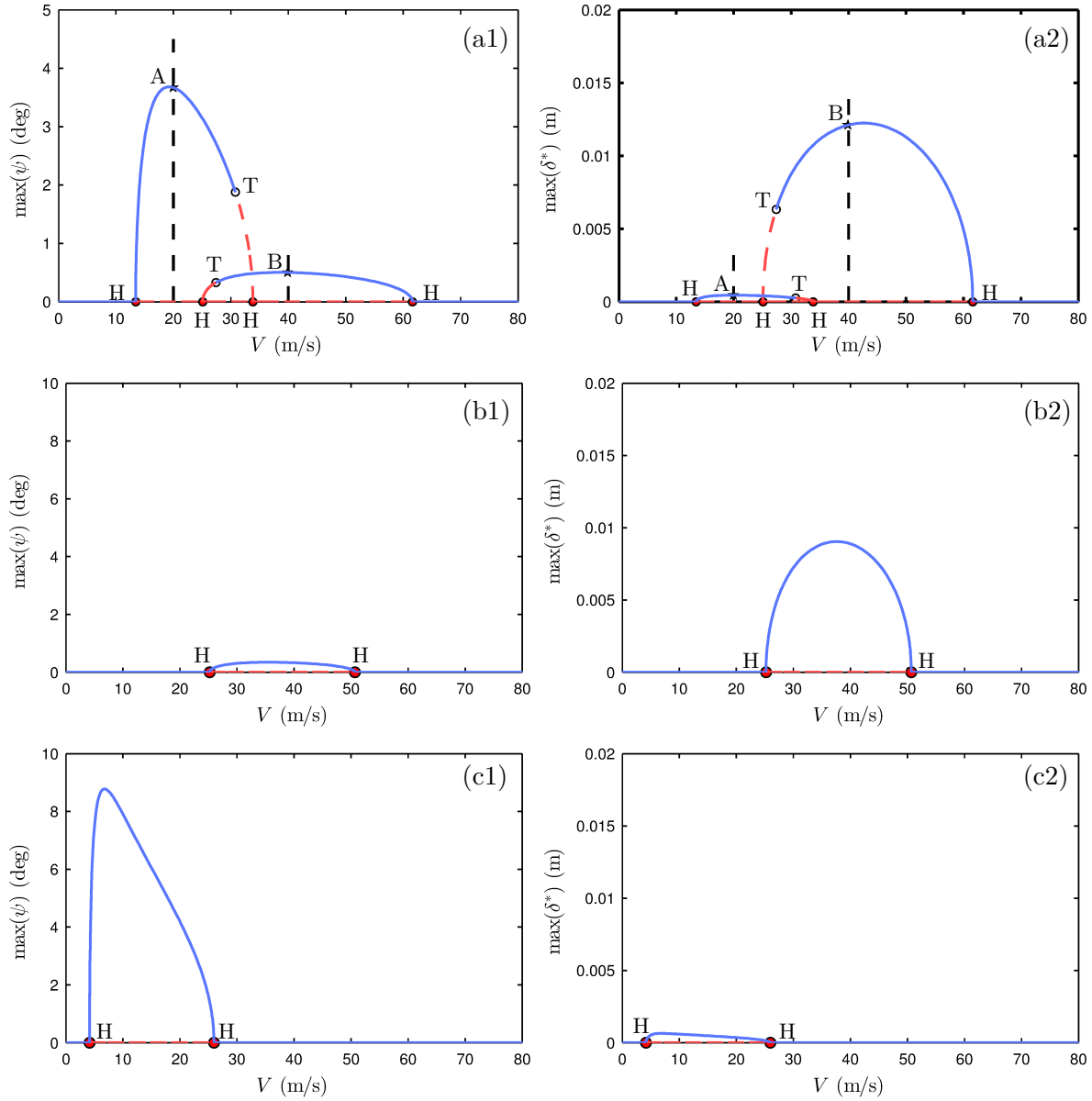

Fig. 5.7 One-parameter bifurcation diagrams in V. Panels (a1) and (a2) are for the damping $c_d = 3.6 \times 10^4$ Nms/rad; (b1) and (b2) for the damping $c_d = 5.0 \times 10^3$ Nms/rad; (c1) and (c2) for $c_d = 2.0 \times 10^3$ Nms/rad. Shown are the maxima of the torsional angle ψ (left column) and of deflections δ^* (right column). Stable solutions are represented by blue solid lines and unstable solutions by red dashed lines; Hopf bifurcation points (H) are shown as red dots, and torus bifurcation points (T) as no-fill circles. The star points A and B in (a1) and (a2) correspond to the cases in which $V = 20$ and 40 m/s, respectively.

c_d, we choose c_d as the second continuation parameter and construct a two-dimensional bifurcation diagram in the (V, c_d)-plane. This is illustrated in Fig. 5.8. Fig. 5.7 represents the three slices $c_d = 3.6 \times 10^4$, 5.0×10^3 and 2.0×10^3 Nms/rad in the two-dimensional plane. The red curves in Fig. 5.8 are Hopf curves which are formed via the continuation of the Hopf point H in the one-dimensional plane. In the (V, c_d)-plane, we observe two Hopf curves intersected with a pair of Hopf-Hopf points (labelled HH). Two curves of torus bifurcations emerge from the two HH points. The third Hopf curve is observed in the lower area of the (V, c_d)-plane. As discussed in the one-parameter bifurcation analysis, the existence of Hopf points represents the onset of shimmy oscillations. Similarly, in Fig. 5.8, these Hopf curves bound regions of different shimmy behaviour. In particular, we find two ψ-shimmy (left-shaded) and one δ-shimmy (right-shaded) region. Grey-shaded areas indicate (V, c_d) regions in which no shimmy solutions exist. Consequently, a region $c_d \in (2754.1, 3019.4)$ bounded by the two blue lines, see insert plot in Fig. 5.8, is also observed. In this region the landing gear will not have sustained shimmy oscillations at any forward speed over the operating range 0–200 m/s. Specifically, this indicates that if the damping of the shimmy damper is designed in the range (2754.1, 3019.4), the MLG will be free of shimmy for any value of V–this is the zero-shimmy region.

5.3.2 A beneficial spring-damper layout

From Fig. 5.8, we found that if the damping of the shimmy damper is designed in the zero-shimmy region, the MLG will be free from instabilities for any forward velocity. However, this zero-shimmy region $(2754.1, 3019.4)$ is quite narrow, so placing tight requirements for the design of the damper, such that it remains in this region for all operating conditions while also accounting for other damping contributions such as joint friction. Hence, it is desirable to expand this zero-shimmy region to provide a more flexible design requirement, hence increased device robustness. To achieve this, we now investigate how varying the stiffness properties will affect the zero-shimmy region.

Note that the focus of this work is the shimmy-suppression device while the structural stiffness as listed in Table 5.1 will not be changed. The suppression device comprises a torsional stiffness k_s connected in series to a spring-damper pair. This configuration is denoted L2 and is depicted in Fig. 5.9. Panel (a) illustrates that, when equipped with the shimmy damper, k_ψ and k_s contribute to give the effective stiffness $k_{\psi e}$. These stiffnesses are related by the expression

$$k_{\psi e} = \left(\frac{1}{k_\psi} + \frac{1}{k_s}\right)^{-1}. \tag{5.37}$$

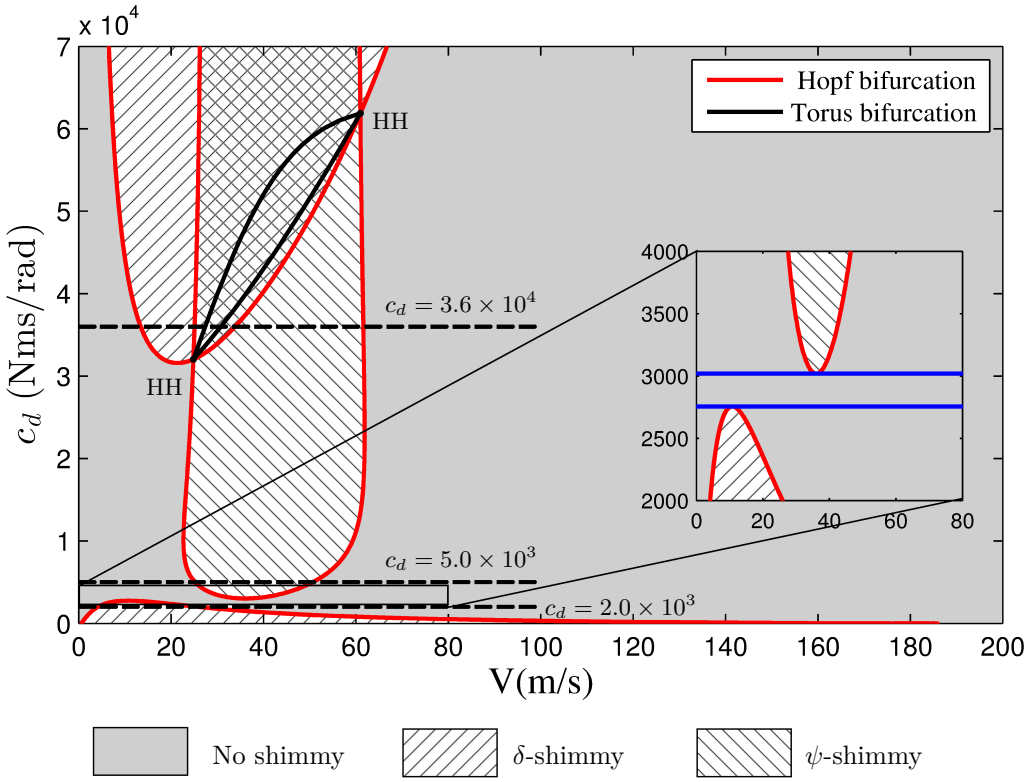

Fig. 5.8 Two-parameter bifurcation diagrams in the (V, c_d)-plane of the MLG with the shimmy damper. The regions of no shimmy, torsional ψ-shimmy and lateral δ-shimmy are shown. The points labelled HH are double Hopf points.

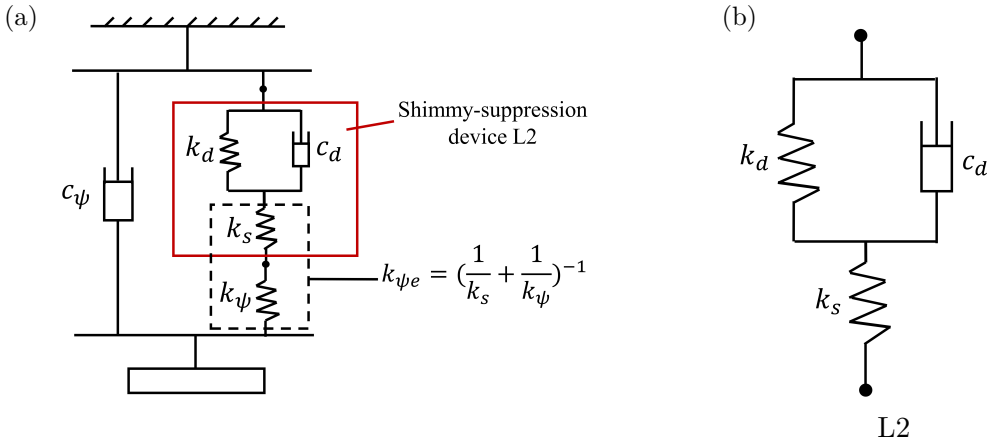

Fig. 5.9 View of (a) the effective structural stiffness $k_{\psi e}$, (b) the proposed spring-damper device layout.

We note that if $k_s = \infty$, $k_{\psi e}$ would equal k_ψ, otherwise $k_{\psi e} < k_\psi$. Now we can investigate the effects of varying $k_{\psi e}$ via varying k_s of L2 on the two-parameter bifurcation diagrams. Fig. 5.10 shows a series of continuations in the (V, c_d)-plane when varying the values of k_s. The black lines in Fig. 5.10(a) which represents $k_s = \infty$ case is equivalent to that in Fig. 5.8. Note that the torus bifurcations curves are omitted for Fig. 5.10 and the following two-parameter bifurcation diagrams. The dominant types of shimmy oscillations are similar to these shown in Fig. 5.8 and so are not marked by shading in this plot. It can be observed from Fig. 5.10(a) that when decreasing k_s from ∞, the δ-shimmy region shrinks and the two ψ-shimmy regions become more significant. This indicates that a smaller k_s, and hence a smaller torsional stiffness, would stabilise the MLG δ-shimmy while destabilising the ψ-shimmy. Fig. 5.10(b) shows that if k_s is decreased to 5.9×10^5 Nm/rad, the δ-shimmy region disappears and a wide zero-shimmy region is found. However, if k_s is reduced further, the two ψ-shimmy regions intersect each other eliminating the zero-shimmy region.

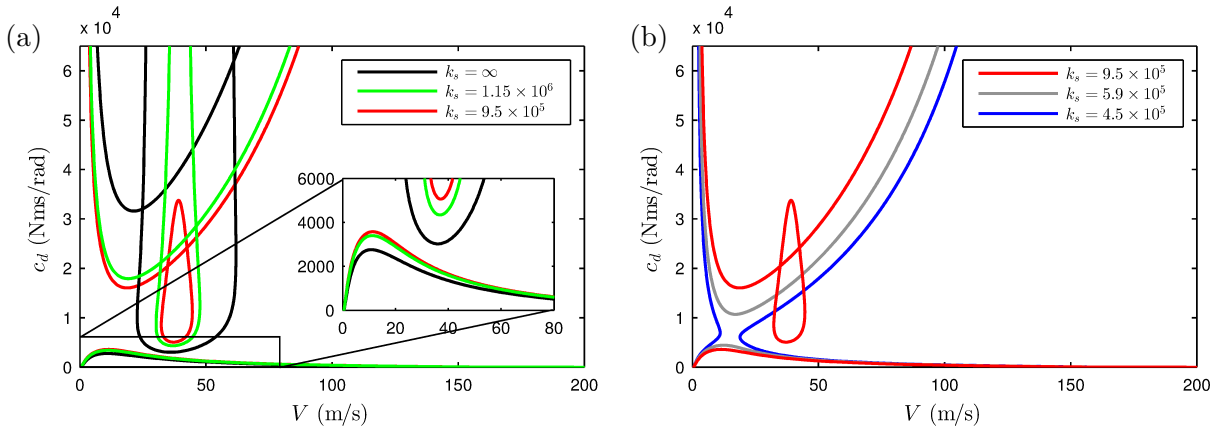

Fig. 5.10 Two-parameter bifurcation diagrams in the (V, c_d)-plane for varying the stiffness k_s (Nm/rad) of L2.

To identify the sensitivity of the system to the variations of k_s in L2 qualitatively, four boundary points of the three shimmy regions in the (V, c_d)-plane are defined, as shown in Fig. 5.11(a). BP1 and BP3 are the boundary points of the upper and lower ψ-shimmy regions, respectively. BP2$_u$ and BP2$_l$ represent the upper and lower boundaries of the δ-shimmy region. As k_s is varied the c_d values of these four boundary points form four curves in Fig. 5.11(b), and the grey area represents the zero-shimmy region. It can be observed that the red (BP3) and blue (BP1) lines intersect at $k_s = 4.73 \times 10^5$ Nms/rad. When k_s is increased from this value, the zero-shimmy region is growing to the maximum until the green lines, i.e. the δ-shimmy region, arise at $k_s = 7.86 \times 10^5$ Nms/rad. The grey area then splits into two parts, one is bounded by BP3 and BP2$_u$,

the other by BP1 and BP2$_l$. Fig. 5.11(c) shows the width of the grey area with respect to the value of k_s and we define this width as the *width in damping of the zero-shimmy region*. It can be seen that the zero-shimmy region is largest in terms of damping values ($c_d \in (3813.7, 14032.7)$) at $k_s = 7.86 \times 10^5$ Nms/rad; at this point the width in damping of this region is 1.02×10^4 Nms/rad ($14032.7 - 3813.7$), which is approximately 38 times what is obtainable with the shimmy damper alone ($k_s = \infty$). After the maximum value, the width in damping of the zero-shimmy region reduces sharply, as shown by the two green lines of Fig. 5.11(c). Therefore, comparing with the original shimmy damper case, this beneficial spring-damper layout L2 is seen to provide a greater allowable damping range over which the MLG will be free from shimmy for all operating velocities.

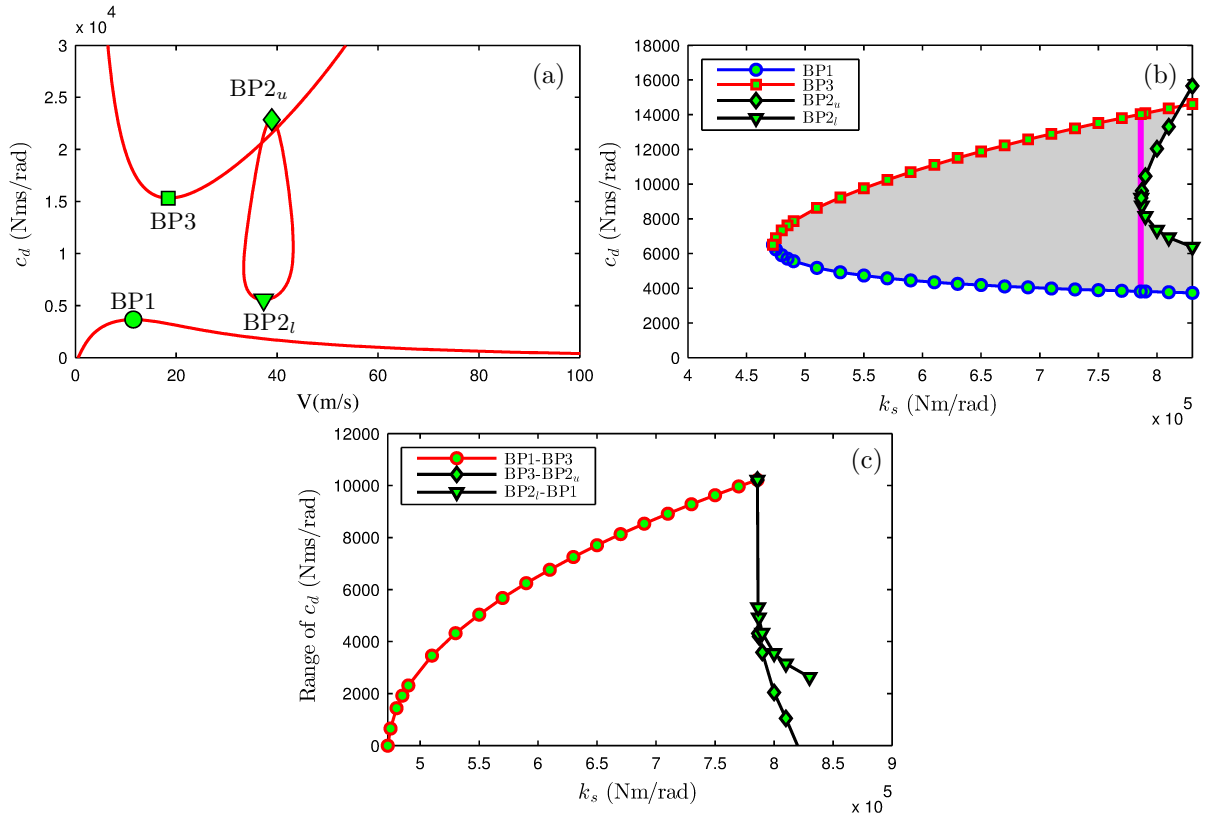

Fig. 5.11 (a) The definitions of four boundary points in two-parameter bifurcation diagrams in the (V, c_d)-plane, (b) the damping values of four boundary points when varying k_s and no-shimmy region in the (k_s, c_d)-plane, (c) the width in damping of the zero-shimmy region for the variation of k_s.

5.4 Effects of inerter-based shimmy-suppression devices

The performance improvements obtained by the inerter-based vibration-suppression devices have been identified for many industrial applications, as introduced in Section 2.3. In this section, two variations on layout L2 that include inerters are considered. The MLG's sensitivity to the parameters of these two inerter-based layouts are investigated and their performance advantages on expanding the zero-shimmy regions are then discussed.

5.4.1 Two candidate inerter-based shimmy-suppression layouts

Fig. 5.12 shows two inerter-based shimmy-suppression layouts proposed in this work, labelled LI1 and LI2. The layouts are inspired by work on the vibration suppression of buildings. LI1 is referred as a TVMD-type layout, which includes the inerter in parallel with c_d and k_d of L2. This layout was first proposed by Ikago *et al.* in [4] and was called the tuned-viscous-mass-damper (TVMD). The original layout excludes k_d; we propose k_d here to function as a centering spring. LI2 is a TID-type layout; the original TID (tuned-inerter-damper) layout was introduced by Lazar *et al.* in [5]. The spring k_s was not introduced in the original layout but is considered here, again acting as a centering stiffness. Note that for both layouts, we focus on the effects of k_s and b while fixing k_d to the value used for the default shimmy damper, 1.09×10^5 Nm/rad. Note also that the two layouts are equivalent to layout L2 if b is set to zero.

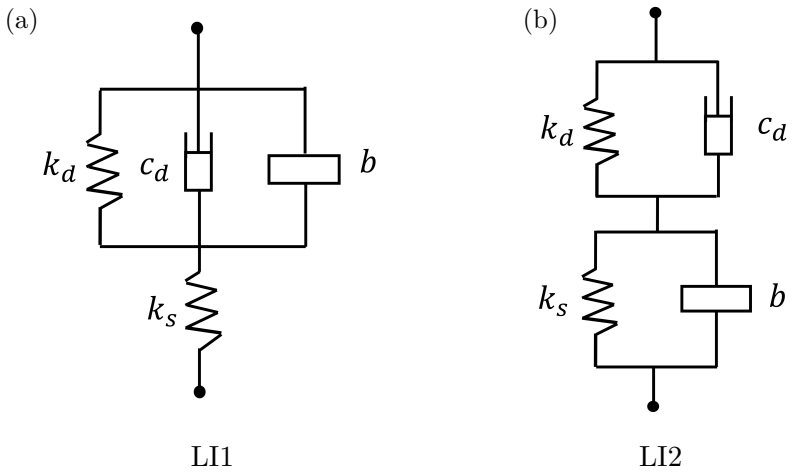

Fig. 5.12 Two candidate inerter-based device layouts, (a) TVMD-type LI1, (b) TID-type LI2.

5.4.2 Effects of layout LI1

Fig. 5.13 shows two-parameter bifurcation diagrams for the layout LI1 for several representative values of k_s when fixing b to different values in the range of $b \in [20, 150]$ Nms^2/rad. Note that $b = 0$ result is equivalent to the L2 bifurcation plots of Fig. 5.10. Several qualitative changes in the appearance of the δ-shimmy regions are observed here. When the inertance b is relatively small such as $b = 20$ Nms^2/rad, changing k_s produces a similar effect to that observed for L2 ($b = 0$). Hence, the width of the zero-shimmy region reaches its maximum just before the δ-shimmy occurs. When b is increased to 30 Nms^2/rad, the first qualitative change is observed – the δ-shimmy curve appears as a narrow-strip below the boundary point BP1 (recall the points BP1, BP2$_u$, BP2$_l$ and BP3 from Fig. 5.11(a)) and moves upwards for larger k_s. Consequently, for $b = 30$ Nms^2/rad, the zero-shimmy region is bounded by two points BP1 and BP3 and is maximised just before the upper boundary of the δ-shimmy region BP2$_u$ exceeds BP1. Increasing b to 70 Nms^2/rad produces a similar variation as that seen for $b = 30$ Nms^2/rad case but now the shape of the δ-shimmy region when it appears is a small circle. When b equals 100 Nms^2/rad, the upper boundary of the δ-shimmy region appears higher than BP1. Similar variation trends of the δ-shimmy region are observed for $b = 130$ and 150 Nms^2/rad.

Note that for the $b \in [70, 150]$ Nms^2/rad cases, an additional (third) ψ-shimmy dominated region is observed, as illustrated in Figs. 5.13(c)–(f). However, as this region is much lower than the point BP1 vertically in the (V, c_d)-plane, it will not affect the zero-shimmy region. It can be seen that a higher b or k_s will give rise to a higher third ψ-shimmy region. For $b = 130$ Nms^2/rad, the upper boundary of the third ψ-shimmy region is lower than BP1 when the δ-shimmy occurs. Here the widest zero-shimmy region is still determined by the two points BP1 and BP3. In contrast, for $b = 150$ Nms^2/rad, the upper boundary of the third ψ-shimmy region grows higher than BP1 before the appearance of the δ-shimmy region. Therefore in this situation, the zero-shimmy region is determined by BP3 and the upper boundary of the third ψ-shimmy region, and reaches the maximum just before the δ-shimmy emerges.

The boundary points in the (V, c_d)-plane are plotted in Figs. 5.14(a1) and (a2) as k_s and b vary. The zero-shimmy regions are shaded in grey and the vertical lines indicate the maximum width in damping of the zero-shimmy region occurs. In contrast to the results for the layout L2, the lower bounds of the grey areas are not just dependent on BP1 and the maximum width in damping of the zero-shimmy region is not always determined by the appearance of the δ-shimmy. The variation of this width with respect to b (vertical lines in Figs. 5.14(a1) and (a2)) is plotted in Fig. 5.14(b). It can be observed that when $b = 140$ Nms^2/rad and $k_s = 6.38 \times 10^5$ Nm/rad, the width of the zero-shimmy region is

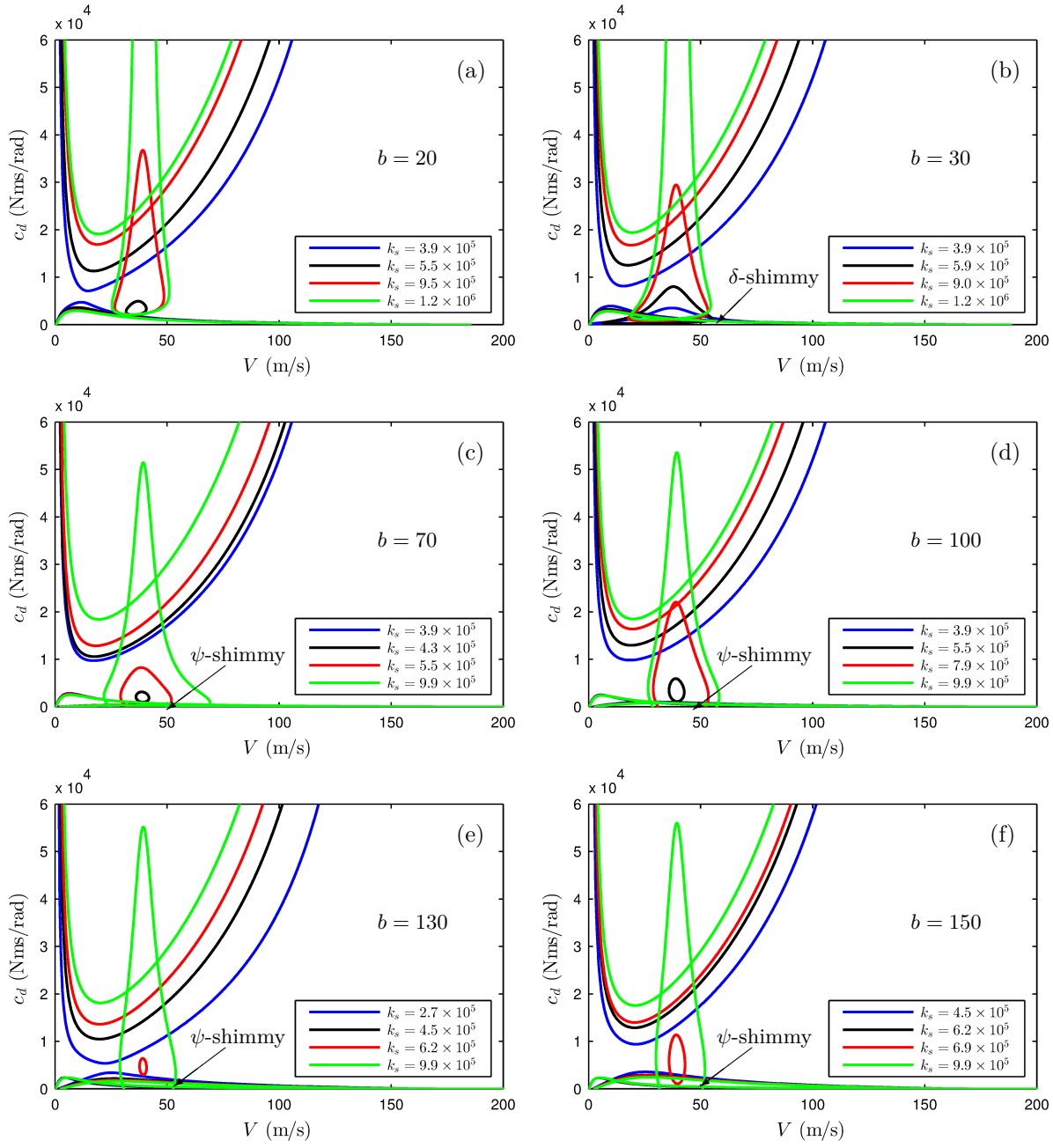

Fig. 5.13 Two-parameter bifurcation diagrams in the (V, c_d)-plane for varying the stiffness k_s (Nm/rad) and b (Nms^2/rad) of LI1.

maximised to 1.12×10^4 Nms/rad $(13561.6 - 2319.1)$, with a maximal 9.8% improvement over that with L2 $(1.02 \times 10^4$ Nms/rad). One notable benefit of the LI1 layout over L2 is that the lower bound of this region, 2319.1 Nms/rad, is significantly smaller than that of L2, 3813.7 Nms/rad. This is potentially beneficial from a manufacturing perspective.

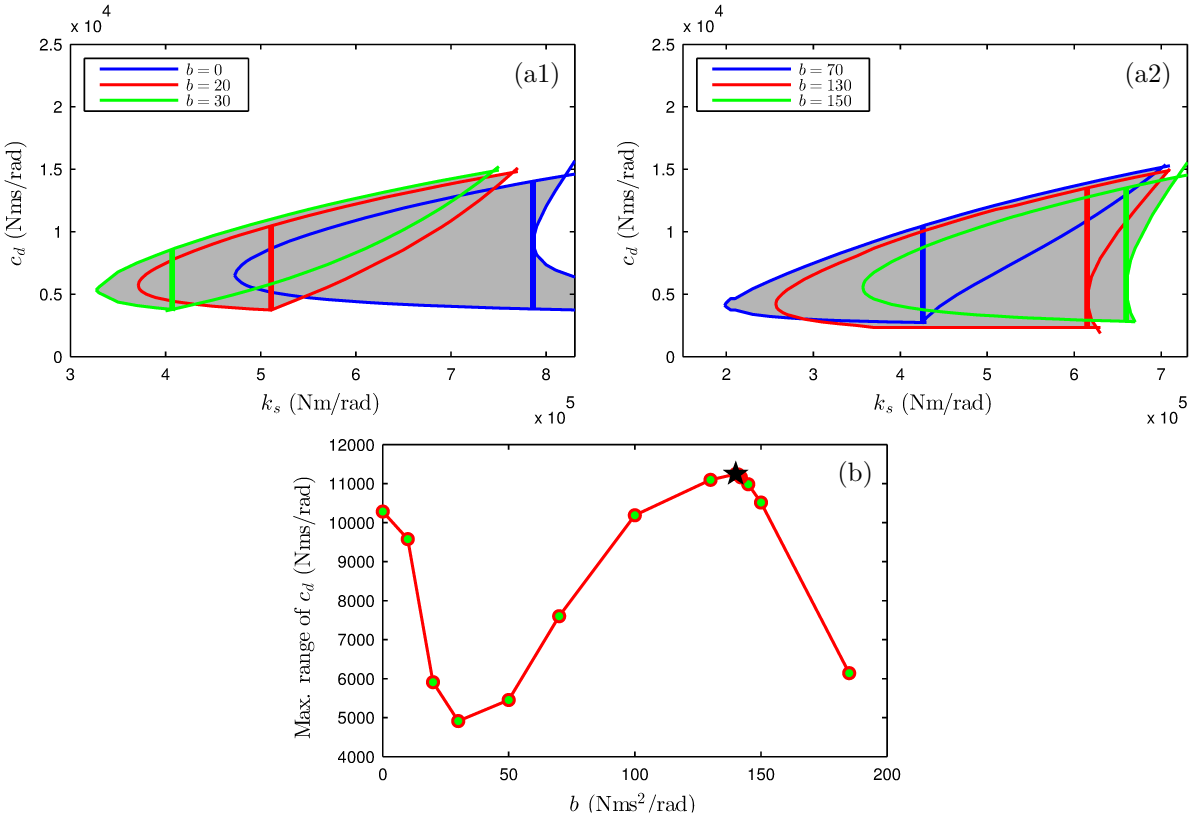

Fig. 5.14 (a) The damping values of boundary points when varying k_s (Nm/rad) and b (Nms^2/rad) of LI1, (b) the maximum width in damping of the zero-shimmy region for the variation of b.

5.4.3 Effects of layout LI2

The same approach is now taken to investigate the influence of layout LI2. Fixing b of LI2 to the specific values, 50 and 100 Nms^2/rad, and then varying k_s, the variations of the bifurcation diagrams in the (V, c_d)-plane are obtained and shown in Fig. 5.15.

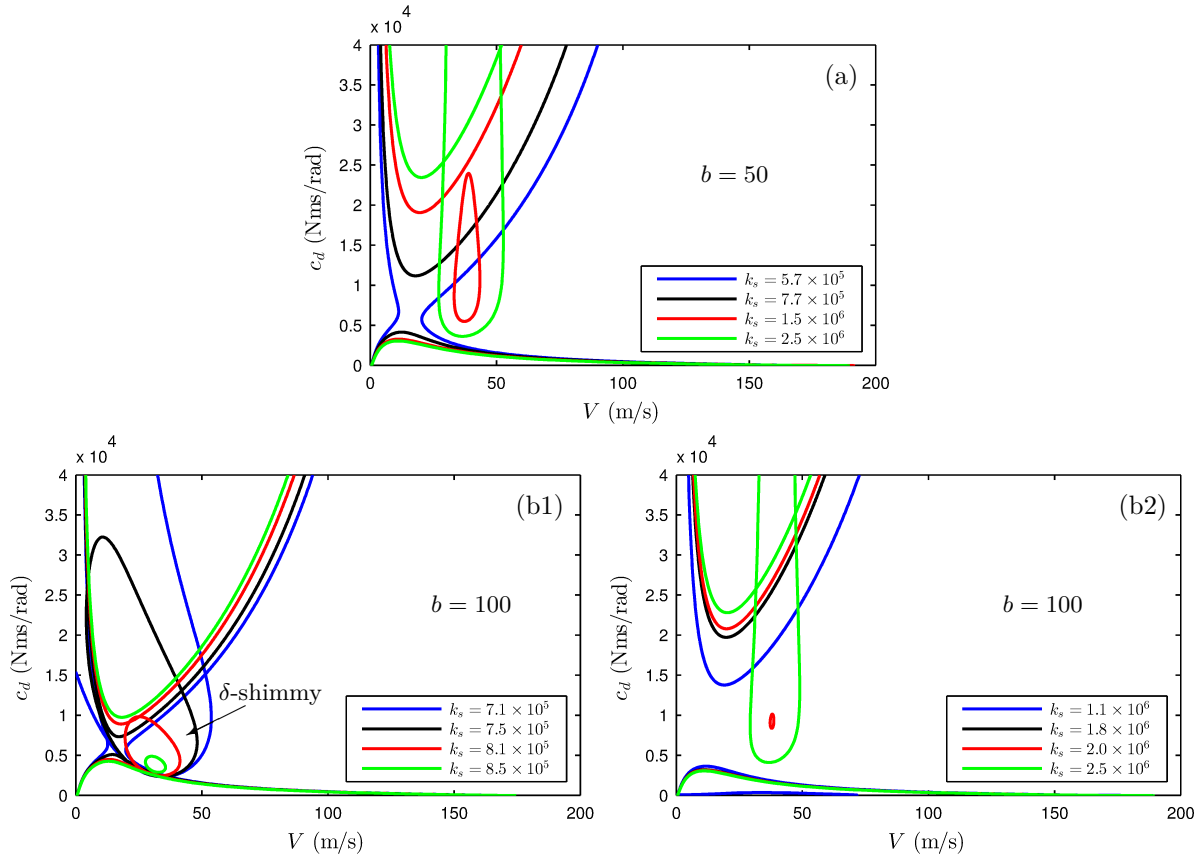

Fig. 5.15 Two-parameter bifurcation diagrams in the (V, c_d)-plane for varying the stiffness k_s (Nm/rad) and b (Nms^2/rad) of LI2.

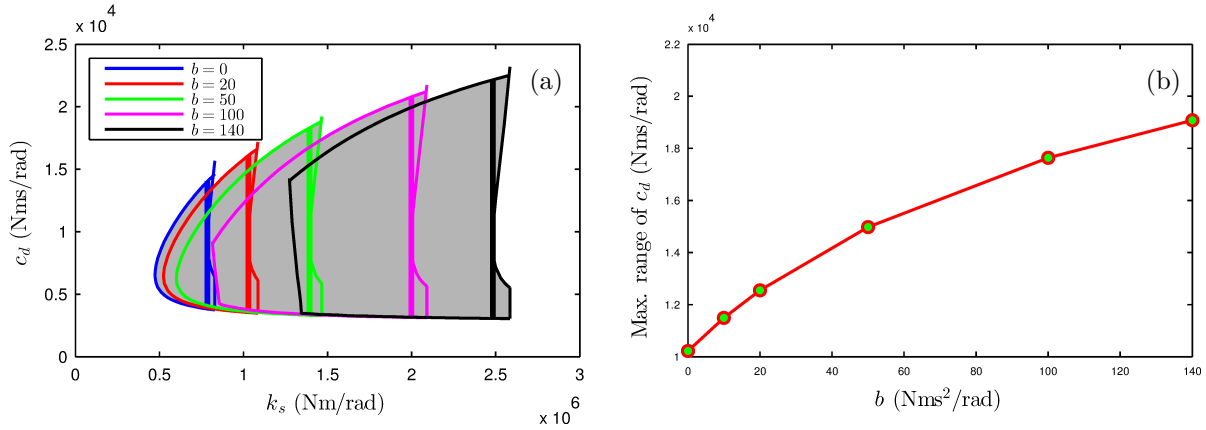

Fig. 5.16 (a) The damping values of four boundary points when varying k_s (Nm/rad) and b (Nms^2/rad) of LI2, (b) the maximum width in damping of the zero-shimmy region for the variation of b.

The zero-shimmy parameter regions are plotted in the (k_s, c_d)-plane in Fig. 5.16(a). As for the $b = 0$ case (layout L2), when $b = 50$ Nms^2/rad the maximum width in damping of the zero-shimmy region arises just before the occurrence of δ-shimmy. If b is increased further, such as to 100 Nms^2/rad, a relatively small k_s will result in a δ-shimmy as shown in Fig. 5.15(b1). This changes rapidly with the variation of k_s and disappears if k_s is allowed to increase sufficiently. The zero-shimmy region is affected by this δ-shimmy. Hence, as illustrated by the zero-shimmy areas bounded by the magenta and black lines of Fig. 5.16(a), the left boundaries are not formed by smooth curves. A further increased k_s leads to the appearance of another δ-shimmy region. It can be seen that the width in damping of the zero-shimmy region reaches its maximum value just before this δ-shimmy arises. As with in Fig. 5.14(b), Fig. 5.16(b) gives the width in damping of the widest zero-shimmy region of Fig. 5.16(a) for each b. It can be calculated that the maximum width in damping of the zero-shimmy region increases with b, however, a much larger k_s is required to obtain this maximum value. When comparing with the layout LI1, this growth trend ends with $b = 140$ Nms^2/rad and gives the maximum width in damping as 1.91×10^4 Nms/rad. This width provides a 87.2% improvement over that of L2. It should be noted that this improvement is determined by achievable values of b and k_s which in turn are likely to result in the shimmy-suppression device having a feasible size and weight.

5.5 Concluding remarks

This chapter was focused on the effects of several shimmy-suppression devices on a MLG system using bifurcation analysis, and proposed a method of selecting the device parameter values to prevent shimmy instability for any forward speed within the operating region. Using this method, it was shown that the use of a proposed spring-damper configuration can result in a more robust device in terms of the zero-shimmy stability over that of a conventional shimmy damper. Two inerter-based shimmy-suppression devices were also considered and yielded further benefits in terms of expanding the zero-shimmy regions in the two-parameter bifurcation diagrams.

Different from Chapter 3, the MLG system considered in this chapter was extended to account for the effects of system nonlinearity, such as geometric nonlinearity, coupling between different DOFs and nonlinear tyre dynamics. A nonlinear mathematical model was developed in terms of MLG torsional rotation, lateral bending and the tyre dynamics, alongside shimmy-suppression device motion. For the MLG equipped with a conventional shimmy damper, if the aircraft was operating under different forward velocity, we observed

two types of shimmy oscillations using time-stepping method, namely ψ-shimmy and δ-shimmy. A bifurcation study was then carried out to investigate the effects of the shimmy-suppression devices on the gear dynamics as two continuation parameters, the forward velocity V and the device damping c_d, were varied. One- and two-parameter bifurcation diagrams were presented to demonstrate how the MLG dynamics were affected by the parameter values of shimmy-suppression devices.

The first device analysed was the shimmy damper, labelled L1. The two-parameter bifurcation diagram in the (V, c_d)-plane found that, to ensure the MLG was free of shimmy instability for any forward velocity, the damping of the shimmy damper needed to be designed within a narrow range. This device damping range was defined as the width in damping of the zero-shimmy region and indicate the robustness of the device. Hence it needs to be enlarged to provide a larger parametric operating range for the damping device. The second layout labelled L2 was achieved by adding an additional spring k_s in series with the shimmy-damper layout, altering the effective torsional stiffness of the system. A series of two-parameter bifurcation diagrams in the (V, c_d)-plane were obtained with respect to k_s and for a range of k_s values, an enlarged zero-shimmy region was observed. The maximum width in damping of this zero-shimmy region was about 38 times that obtained by the shimmy damper.

Two inerter-combined layouts LI1 and LI2 were then proposed. The effects of changing the parameter values of LI1 and LI2, namely k_s and b, on the two-parameter diagrams in the (V, c_d)-plane were investigated. It was found that for LI1, the width in damping of the zero-shimmy region was maximised, with a maximal 9.8% improvement over that obtained with L2. One notable benefit of the LI1 layout over L2 was that the lower bound of this maximum zero-shimmy region was significantly smaller than that of L2. For LI2, the maximum width in damping of the zero-shimmy region increased significantly with growing b and k_s.

In Chapters 3, 4 and this chapter, we demonstrated the effectiveness of the proposed optimal design methodologies for passive vibration suppression devices, which focused on the device configuration level with idealised components (springs, dampers and inerters). There was no emphasis on the physical realisations of such components in a device which it is significant during an engineering design process. In the following chapter, this gap will be filled by introducing a systematic design approach on optimising the physical device arrangement of a mechanical/hydraulic device.

Chapter 6

Optimal physical device arrangements for a hydraulic engine mount

6.1 Introduction

In this chapter, we focus on suppressing steady-state oscillations with optimised vibration suppression devices. Here we consider hydraulic engine mounts optimising over a wide frequency range. A systematic mechanical design approach is proposed to identify optimal physical device arrangement, i.e. fluid passageways, within the hydraulic engine mount. This approach allows all possible networks with predetermined topologies and geometries of fluid passageways to be optimised. Based on the low-frequency optimisations, the performance advantages of beneficial fluid passageways on the maximum displacement transmissibility are demonstrated. Due to the trade-off between the low-frequency and high-frequency performance criteria, optimisations are extended to a wider frequency range and the effects of nonlinear decoupler and flow restriction are accounted for. The nonlinear dynamics are analysed using a combination of time-stepping and continuation methods.

As introduced in Section 2.1.2, engine mount design is crucial to achieve longer fatigue life, reduced noise and enhanced passage comfort for road vehicles. In the current drive for more light-weight and flexible vehicles, enhancing the capabilities of engine mounts becomes even more important. Apart from the function of supporting the engine, a good engine mount must satisfy two design requirements, each over a specific frequency range. Firstly, the mount needs to be 'soft' to isolate the car body from unbalanced engine forces that are in the frequency range 25–250 Hz. In addition, to protect the connecting parts between the engine and chassis, it is desirable to constrain the engine-chassis displacement resulting from low-frequency high-amplitude excitations. Such excitations are typically in the range of 0–30 Hz, such as idle shake or travelling over bumpy road [166]. Due to

this conflict, frequency-dependent mount behaviour is required. Consequently, hydraulic mounts were proposed to provide frequency-dependent amplitude-sensitive stiffness and damping, improving the dynamic properties over those of rubber-metal mounts [167].

A typical passive hydraulic engine mount [8] is illustrated as Fig. 6.1 and described in more detail in Section 6.2.1. As introduced in Section 2.2.1, the inertia track and the decoupler are two fluid paths to allow the fluid passing through while we treat the inerter track as the fluid passageway here. To capture the mount dynamic properties, numerous efforts have been made to model it as a linear system [166, 168, 169]. The nonlinear features have also been studied in [8, 170–173], both theoretically and experimentally.

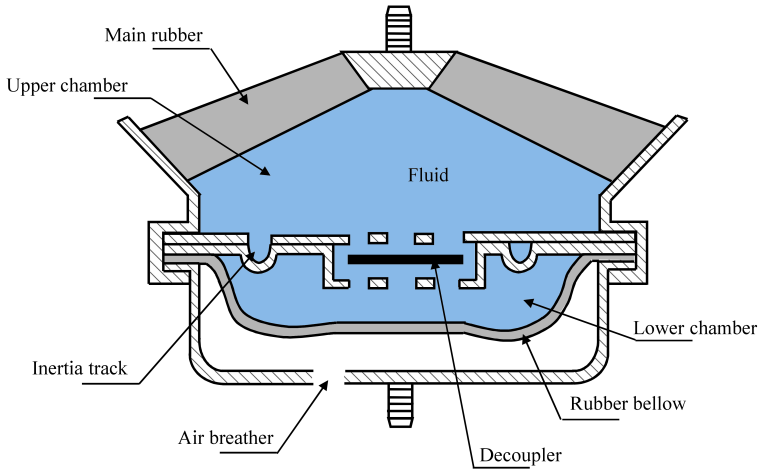

Fig. 6.1 Cross-section schematic of a typical hydraulic passive engine mount (reproduced from [8]).

Numerous studies have also been made to improve the engine mount performances. Apart from optimum tuning of the conventional mount properties, such as the rubber stiffness, piston area, fluid inertia, volumetric stiffness and damping [57–59], altering the mount's interior arrangements to improve flow motion has been considered in [72, 73, 174–177]. Controllable cross-section area [72] and length [73] of inertia track are achieved via semi-active means, as well as improved performance. Zhang *et al.* [176] investigated the dynamic responses of hydraulic mounts with multiple parallel inertia tracks for 0-30 Hz using linear and nonlinear lumped parameter models. The orifice was considered as a flow passageway type in [177] and its inclusion leads to a broadband device. However, in this area, experimental examination and analytical validation are limited to low frequency ranges. Furthermore, designs with multiple inertia tracks are considered in other hydraulic-rubber isolators, such as hydraulic bushings [85, 178, 179].

Up to now, most efforts for designing interior fluid passageways in a mount were via a 'trial and error' approach, with the main emphasis of the work on modelling. The improvement is limited due to the fact that there are countless possible designs that have not been covered by these studies. Furthermore, the optimum tuning work is restricted to specific operation conditions while the compromise of two conflicting low- and high-frequency design requirements is not considered in the optimisation process.

This chapter presents a systematic optimum design approach to explore all potential fluid passageway designs with predetermined passageway number and geometry constraints. Firstly a conventional hydraulic mount reported in [8] is discussed in Section 6.2. The nonlinear mathematical model for a full range of concerned frequency is presented. A linearised low-frequency model that ignores the effects of decoupler is also introduced, alongside the equivalent mechanical network using the mechanical-electrical-hydraulic analogy (see Section 2.3.2). In addition, considering the design requirements, two performance criteria, displacement transmissibility for low frequency and dynamic stiffness amplitude for high frequency, are proposed. Both time-stepping and continuation methods are used to analyse the high-frequency dynamic behaviour.

In Section 6.3, two types of fluid passageways are considered, one is the capillary inertia track and the other one is flow restriction. We then propose all possible topologies considering up to four fluid passageways. Using the linearised low-frequency model, optimisations are carried out to minimise the maximum displacement transmissibility with predetermined fluid passageway geometries and numbers. It is shown that the low-frequency responses obtained with linearly optimised solutions are affected notably by the decoupler mechanism and the high-frequency performances deteriorate slightly comparing with the default system. To address these, optimisations are extended using a nonlinear model in Section 6.4, and by limiting high-frequency dynamic stiffness. From the results it is shown that the improvement on low-frequency cost function is reduced if the high-frequency constraint is applied. A sensitivity analysis of low-frequency performances to high-frequency constraint is then carried out and it is shown that if the high-frequency constraint is relaxed slightly, the maximum low-frequency displacement transmissibility can be improved significantly.

Publications resulting from this work

Y. Li, J. Z. Jiang, and S. A. Neild, "Optimal fluid passageway designs for a hydraulic engine mount considering both low and high frequency performances," in preparation.

6.2 Passive hydraulic engine mount model and performance criteria

In this section, the nonlinear hydraulic engine mount model reported in [8] is considered to capture the mount dynamic behaviour over a wide frequency range. Considering the low-frequency excitations with large amplitudes, a linearised low-frequency model ignoring the decoupler is introduced. Based on the hydraulic dynamics, an equivalent mechanical model is also presented. Two performance criteria over the two concerned frequency ranges are then proposed according to the design requirements.

6.2.1 Passive hydraulic engine mount model

For a hydraulic engine mount, there are two fluid-filled chambers, the upper and the lower chambers, which are connected via a spiral inertia track and a decoupler. As shown in Fig. 6.1, a typical free decoupler is assumed and shown is its fully open state. The upper chamber provides the function of supporting the engine weight with stiffness k_r and act like a piston, with an effective piston area A_p, to push the fluid flowing through the fluid passageways to the lower chamber. The lower chamber's lower surface is made of a thin complaint rubber bellow. The chambers present volumetric compliance, C_1 and C_2. The decoupler mechanism consists of a rubber plate which is bounded by cages and the cage plates are configured with orifices. Such mechanism allows the decoupler plate to travel within a limited distance to control flow motion under excitations of different amplitudes.

Nonlinear model for a wide frequency range

A lumped parameter model [8], to predict the mount behaviour in both low and high frequencies, is considered here. Recall the two types of excitations introduced in Section 6.1, namely, low-frequency high-amplitude excitations that are typically road inputs and high-frequency low-amplitude ones, such as unbalanced engine forces. Here, we first consider a low-frequency base excitation x_s to formulate the overall equations of motion. Then a high-frequency engine excitation x_e will be assumed in Section 6.2.2, to capture the high-frequency performances.

The upper chamber damping, c_r, is introduced together with the stiffness k_r. Assuming the flow through the inertia track is laminar flow and the entrance loss is negligible, the inertia track is modelled by fluid inertia I_i and linear resistance R_i. Under the

large-amplitude excitation, the decoupler plate will contact the cage and the flow will almost entirely pass through just the inertia track. If the excitation amplitude is small, the fluid will freely flow through the decoupler cage orifice. In this model, the decoupler is modelled using fluid inertia I_d and a nonlinear resistance R_d of which the function will represent the switching mechanism. The chassis displacement excitation x_s due to road unevenness is applied and the resulting engine displacement is represented by x_e.

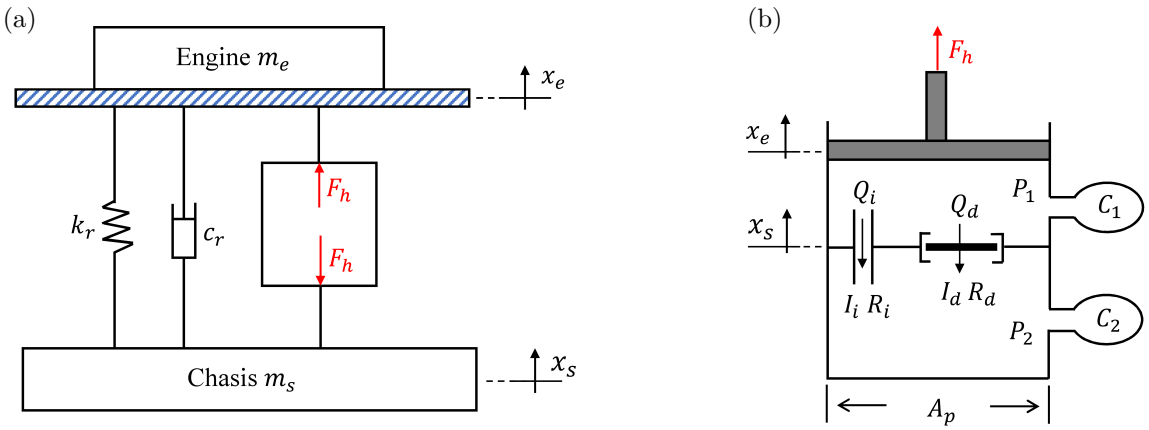

Fig. 6.2 Shown are (a) engine-mount-chassis model with chassis excitation x_s and resulting engine motion x_e, (b) the lumped hydraulic parameter model.

According to the continuity and momentum equations, we have

$$C_1\dot{P}_1 = -A_p(\dot{x}_e - \dot{x}_s) - Q_i - Q_d, \tag{6.1}$$

$$C_2\dot{P}_2 = Q_i + Q_d, \tag{6.2}$$

$$P_1 - P_2 = I_i\dot{Q}_i + R_iQ_i, \tag{6.3}$$

$$P_1 - P_2 = I_d\dot{Q}_d + R_dQ_d, \tag{6.4}$$

where P_1 and P_2 are the pressure within upper and lower chambers, and Q_i and Q_d are the fluid flow rates through the inertia track and decoupler, respectively. The flow volume for inertia track and decoupler are represented by $V_i = \int Q_i dt$ and $V_d = \int Q_d dt$, respectively. The nonlinear resistance R_d is

$$R_d = R_d^{'} + R_0 e^{(X_d/X_0)\arctan(Q_d/Q_0)}, \tag{6.5}$$

where $R_d^{'}$ is linear resistance and the term $R_0 e^{(X_d/X_0)\arctan(Q_d/Q_0)}$ represents an additional resistance to control the decoupler switching function. R_0 is a constant which is to represent such additional resistance magnitude in the appropriate range, the decoupler position $X_d = V_d/A_d$ where A_d is the measured decoupler area. The constants X_0 and

Q_0 are introduced to reflect the decoupler cage height and produce a crisp switching response, respectively.

To calculate the transmitted force F_T from the mount to the chassis or the engine, we have

$$F_T = m_e\ddot{x}_e = -k_r(x_e - x_s) - c_r(\dot{x}_e - \dot{x}_s) + F_h, \tag{6.6}$$

where

$$F_h = (A_p - A_{dfnc})(P_1 - P_2) + A_pP_2 + A_dR_dQ_d, \tag{6.7}$$

$$A_{dfnc} = \frac{1}{\pi}A_d(\frac{\pi}{2} - \arctan(\frac{(2/\pi)X_d \arctan(\Delta P/P_0) - X_{dmax}}{X_1})). \tag{6.8}$$

F_h represents the total force generated by the flow motion in the mount. The effective piston area equals the quantity of reducing the total piston area A_p by A_{dfnc}, which represents the decoupler area with respect to the plate position and pressure differential. P_0 and X_1 are constants used to normalise the function and control the switching function shape. X_{dmax} is half the decoupler cage height. Readers can refer to [8] for details of the modelling process.

In summary, there are 5 states in the equations of motion (Eqs. (6.1) - (6.8)), which are P_1 for the upper chamber fluid pressure, P_2 for the lower chamber fluid pressure, Q_i for the flow rate in inertia track, Q_d for the flow rate in decoupler and x_e for the engine motion. Eqs. (6.1) - (6.8) can be expressed as the following state-space representation,

$$\dot{\boldsymbol{x}} = \begin{bmatrix} 0 & 0 & -1/C_1 & -1/C_1 & 0 & -A_p/C_1 \\ 0 & 0 & 1/C_2 & 1/C_2 & 0 & 0 \\ 1/I_i & -1/I_i & -R_i/I_i & 0 & 0 & 0 \\ 1/I_d & -1/I_d & 0 & -R_d/I_d & 0 & 0 \\ 0 & 0 & 0 & 0 & 0 & 1 \\ (A_p - A_{dfnc})/m_e & A_{dfnc}/m_e & 0 & (A_dR_d)/m_e & -k_r/m_e & -c_r/m_e \end{bmatrix} \boldsymbol{x} + \boldsymbol{u}, \tag{6.9}$$

$$\boldsymbol{u}^T = [(A_p/C_1)\dot{x}_s \;\; 0 \;\; 0 \;\; 0 \;\; 0 \;\; (k_r/m_e)x_s + (c_r/m_e)\dot{x}_s],$$

where $\boldsymbol{x}^T = [P_1 \;\; P_2 \;\; Q_i \;\; Q_d \;\; x_e \;\; \dot{x}_e]$, $\dot{\boldsymbol{x}}^T = [\dot{P}_1 \;\; \dot{P}_2 \;\; \dot{Q}_i \;\; \dot{Q}_d \;\; \dot{x}_e \;\; \ddot{x}_e]$, and the nonlinear terms R_d and A_{dfnc} are defined by Eqs. (6.5) and (6.8).

The system parameters used in this analysis are summarised in Table 6.1. This model, which can provide the close low- and high-frequency responses comparing with [8], for example, Figures 4-9, has been validated for a further analysis. The default inertia track

Table 6.1 Parameters values used in the analysis

Symbol	Parameter	Value
	Mount parameter	
A_d	Effective decoupler area	6.6×10^{-4} m^2
A_i	Default inertia track cross-section area	5.72×10^{-5} m^2
A_p	Effective piston area	2.5×10^{-3} m^2
c_r	Upper chamber damping	300 Ns/m
C_1	Upper chamber compliance	3.0×10^{-11} m^5/N
C_2	Lower chamber compliance	2.6×10^{-9} m^5/N
I_d	Fluid inertia in decoupler	7.5×10^4 kg/m^4
I_i	Fluid inertia in inertia track	3.8×10^6 kg/m^4
k_r	Upper chamber stiffness	2.25×10^5 N/m
L_i	Default inertia track length	0.212 m
P_0	Pressure normalised constant	10 N/m^2
Q_0	Flow normalised constant	1.0×10^{-9} m^3/s
$R_d^{'}$	Linear fluid resistance in decoupler	1.17×10^7 kg/(s·m^4)
R_i	Fluid resistance in inertia track	1.05×10^8 kg/(s·m^4)
R_0	Nonlinear resistance constant in decoupler	1.0×10^{-4} kg/(s·m^4)
X_{dmax}	Half decoupler cage height	5.3×10^{-4} m
X_0	Decoupler position control constant	2.62×10^{-5} m
X_1	Decoupler switching function shape control constant	1.0×10^{-9} m
ρ	Fluid density	1.028×10^3 kg/m^3
	Engine parameter	
m_e	Engine mass	60 kg

geometry, the length L_i and cross-section area A_i, are also included in Table 6.1 and used as a reference for the following discussion. The constants of R_0, X_0, Q_0, P_0 and X_1 are identified to fit the experimental data [8].

Linearised low-frequency model

When the engine mount is subject to a low-frequency large-amplitude excitation, the decoupler plate deflects significantly and contacts the cage most of the time. Note that transition from bottom cage to top is assumed to be fast so very limited flow passes through the decoupler, see Section 6.2.2 for details. In this case, it can be assumed that the fluid can only travel through the inertia track and the state-space form of governing equations become

$$\dot{\boldsymbol{x}} = \begin{bmatrix} 0 & 0 & -1/C_1 & 0 & -A_p/C_1 \\ 0 & 0 & 1/C_2 & 0 & 0 \\ 1/I_i & -1/I_i & -R_i/I_i & 0 & 0 \\ 0 & 0 & 0 & 0 & 1 \\ A_p/m_e & 0 & 0 & -k_r/m_e & -c_r/m_e \end{bmatrix} \boldsymbol{x} + \boldsymbol{u}, \tag{6.10}$$

$$\boldsymbol{x}^T = [P_1 \;\; P_2 \;\; Q_i \;\; x_e \;\; \dot{x}_e], \quad \dot{\boldsymbol{x}}^T = [\dot{P}_1 \;\; \dot{P}_2 \;\; \dot{Q}_i \;\; \dot{x}_e \;\; \ddot{x}_e],$$
$$\boldsymbol{u}^T = [(A_p/C_1)\dot{x}_s \;\; 0 \;\; 0 \;\; 0 \;\; (k_r/m_e)x_s + (c_r/m_e)\dot{x}_s].$$

Using the analogy introduced in Section 2.3.2, an equivalent mechanical network which generates F_h is obtained, as shown in Fig. 6.3. The following relationships between hydraulic and mechanical parameters need to be satisfied:

$$k_1 = \frac{{A_p}^2}{C_1}, \;\; k_2 = \frac{{A_p}^2}{C_2}, \tag{6.11}$$

$$c_i = {A_p}^2 R_i, \;\; b_i = {A_p}^2 I_i. \tag{6.12}$$

This mechanical model does not include mass elements but does incorporate mechanical inerters b_i. The inclusion of inerter can help formulate the transfer functions of different fluid-passageway designs more conveniently while if mass elements are used the whole set of equations of motion needs to be written.

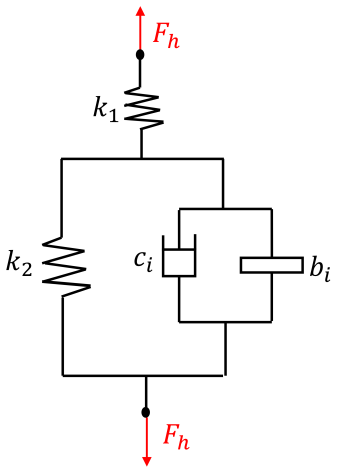

Fig. 6.3 A low-frequency equivalent mechanical network generated by hydraulic dynamics, assuming no flow through the decoupler.

6.2.2 Performance criteria

An ideal engine mount is expected to achieve lower vibration transmission at low frequency excitations and good isolation for higher frequencies. Therefore, two performance criteria are proposed in this analysis.

Low-frequency displacement transmissibility

One of the most significant low-frequency excitation sources is road disturbance. Under this excitation, the relative engine-chassis displacement transmissibility from the base excitation should be keep as low as possible to protect the connecting parts between engine and chassis [27] and avoid the system resonant vibrations. A relative engine displacement transmissibility T_d is introduced here to measure this performance criterion. The base excitation x_s is assumed as

$$x_s = \mathbf{X_{ms}} \sin(2\pi f t), \tag{6.13}$$

$$|T_d| = \frac{|x_e - x_s|}{|x_s|}, \tag{6.14}$$

where the excitation amplitude $\mathbf{X_{ms}} = 1.0$ mm and $0 < f \leq 30$ Hz [170]. Note that in this analysis the relative displacement transmissibility refers to its amplitude $|T_d|$.

Using the parameters summarised in Table 6.1, the time-domain responses for both nonlinear and linear models can be simulated using Matlab/Simulink. Then the frequency

responses of $|T_d|$ are obtained with Fourier transformation, as shown in Fig. 6.4. It can be calculated that for 0-30 Hz the nonlinear maximum $|T_d|$ (max($|T_d|$)) is 3.45 while the linear max($|T_d|$) is 3.64. Using state space, the system resonances can be calculated, the two peaks shown in Fig. 6.4, and resulting mode shapes. Based on the mode shapes and estimated system natural frequencies, it can be seen that the first peak is engine mass dominant and the second one inertia track dominant.

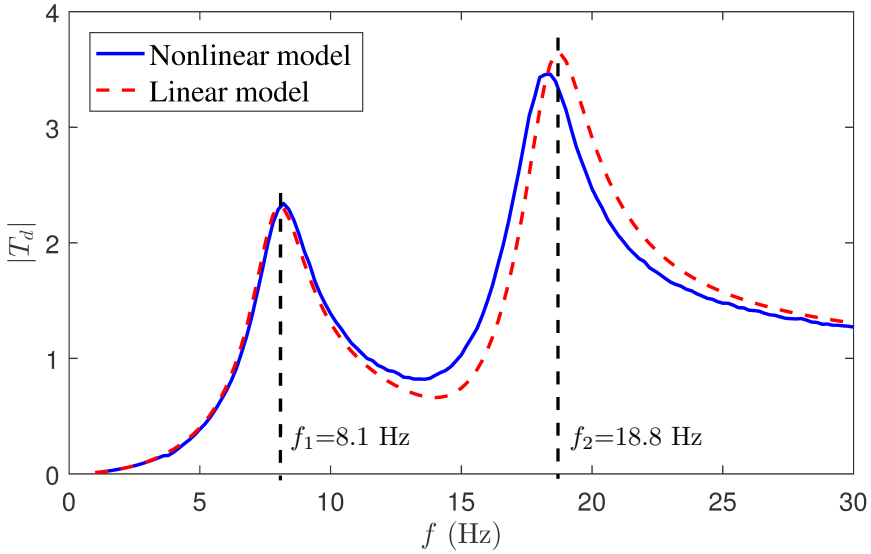

Fig. 6.4 Comparison of low-frequency $|T_d|$ using the nonlinear and the linear (Section 6.2.1) models under a base excitation x_s. f_1 and f_2 represent the two peak frequencies obtained with the linearised model.

The steady-state time-domain responses of Q_i and Q_d at two peak frequencies (f_1=8.1 Hz and f_2=18.8 Hz) of the linearised model are shown in Fig. 6.5. The peaks of the Q_d responses represent the fast transition flow from decoupler bottom cage to top. It can be seen that at f_1=8.1 Hz the effective flow through the decoupler is negligible comparing with that through the inertia track. Hence the effects of decoupler are negligible and the linearised model should provide similar results with the nonlinear model, as shown in Fig. 6.4. At f_2=18.8 Hz, the effects of decoupler flow motion are more significant than f_1=8.1 Hz case. So the difference between the results of linearised and nonlinear model is more noticeable. However, by observing the overall behaviour for low frequency, the effects of decoupler on the low frequency response is still regarded as insignificant.

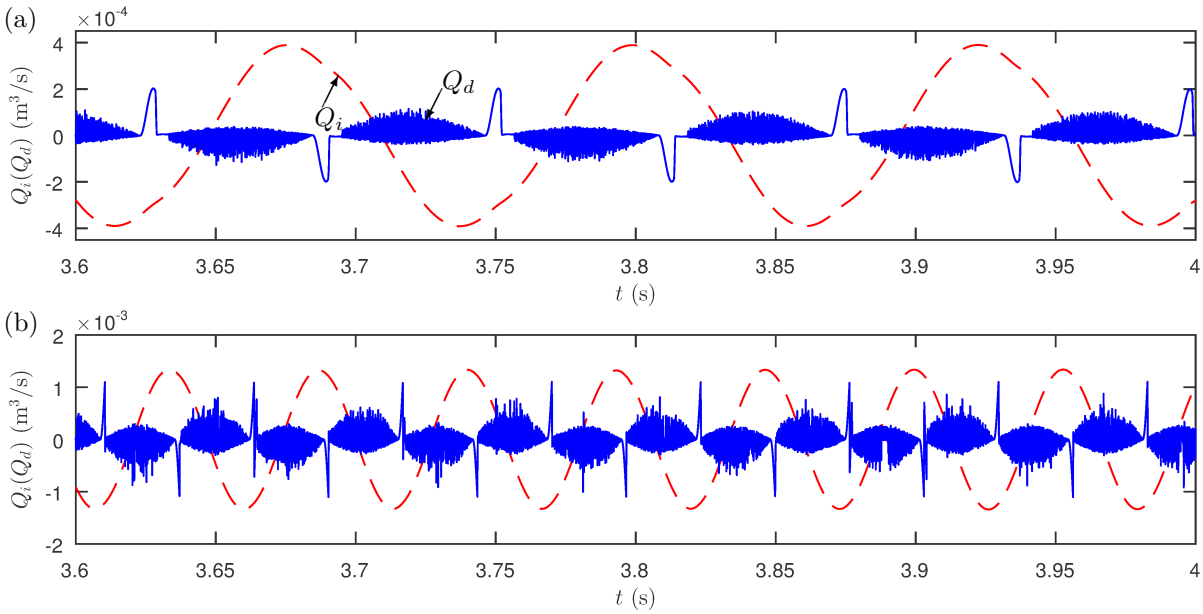

Fig. 6.5 Time histories of Q_i and Q_d at the two peaks frequencies, (a) $f_1 = 8.1$ Hz and (b) $f_2 = 18.8$ Hz.

High-frequency dynamic stiffness

To ensure good high-frequency isolation, the maximum high-frequency dynamic stiffness amplitude of the engine mount, which is represented by $\max(|K_{dyn}|)$, is chosen as the second performance criterion of interest. As introduced in Section 6.1, for high frequency the engine mount experiences the excitations with small amplitudes. Under these excitations, the decoupler is not normally in contact with the cage allowing flow motion across it. To capture the mount's dynamic behaviour under high-frequency small-amplitude excitations, the accurate nonlinear model over a wide range of frequency needs to be used here. A fixed base is assumed and an engine excitation x_e is applied, as shown in Fig. 6.6. We assume

$$x_e = \mathbf{X_{me}} \sin(2\pi f t), \tag{6.15}$$

$$|K_{dyn}| = \frac{|F_T|}{|x_e|}, \tag{6.16}$$

where the excitation amplitude $\mathbf{X_{me}} = 0.05$ mm and $30 < f \leq 250$ Hz [8]. Time stepping with Matlab/Simulink is used to achieve the dynamic stiffness amplitude in frequency domain.

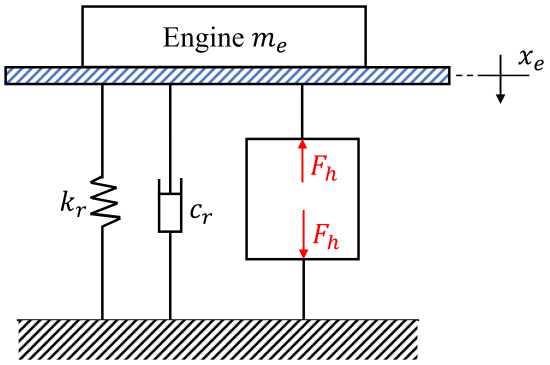

Fig. 6.6 Engine-mount-chassis system with engine excitation x_e considered.

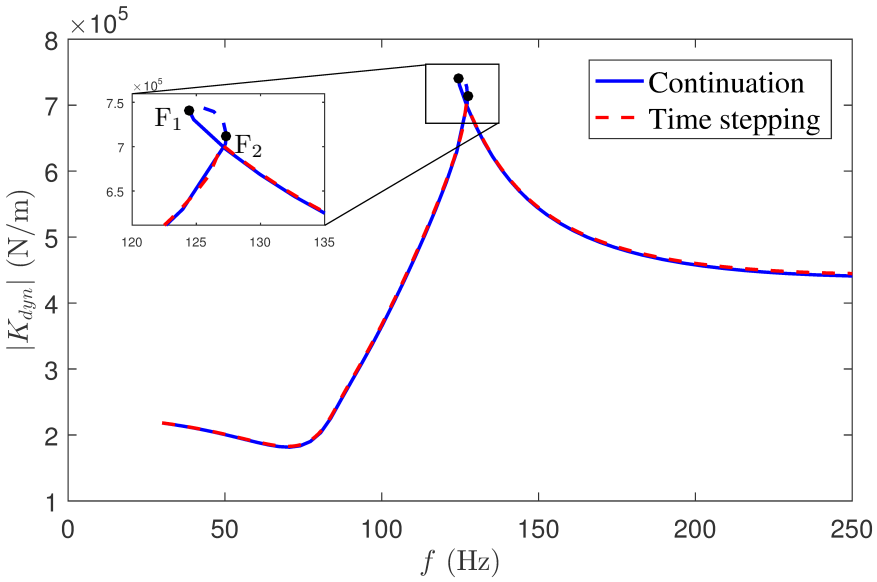

Fig. 6.7 Comparison of high-frequency $|K_{dyn}|$ using continuation and time-stepping methods. The two fold bifurcation points, labelled as 'F', are marked by two black points. The stable solutions are represented by blue solid lines and unstable by dashed ones.

However, it is found that over a frequency region around which the peak $|K_{dyn}|$ occur, the time-domain steady-state responses are multi-valued and sensitive to the initial conditions applied. This phenomenon, introduced by an unstable region due to the existence of nonlinearity, was also observed in [8]. Forward and backward sweep excitation techniques were applied to demonstrate the impacts of initial conditions in [8]. To identify such unstable region adequately, numerical continuation technique which was used in Chapter 5, is used in this work as well. The continuation software AUTO [160], which has been integrated into Matlab via the Dynamical Systems Toolbox [161] and used in Chapter 5, is also employed here. A comparison between the periodic responses obtained using continuation and time-stepping method with Matlab/Simulink with zero initial conditions

for a certain mount configuration is shown in Fig. 6.7. The stable solutions are represented by blue solid lines and unstable by dashed ones, which are $f \in [124.5, 127.3]$ Hz. This qualitative change in behaviour is due to a fold bifurcation (labelled F) involving two equilibria collide and annihilate each other. This method is arguably more robust than time stepping in finding the peak amplitude of response as close to the peak small perturbations, such as those introduced when stepping in frequency, can result in a premature jump to the other stable solutions. Figs. 6.8(a) and (b) show the maximum amplitudes of states Q_i and Q_d with respect to frequency. The solutions are obtained with the time-stepping forward sweep and backward sweep excitation cases, as well as via continuation. The maximum amplitude of decoupler position X_d with respect to frequency is also illustrated in Fig. 6.8(c). It can be seen that the maximum decoupler position almost reaches its limit, X_{dmax}.

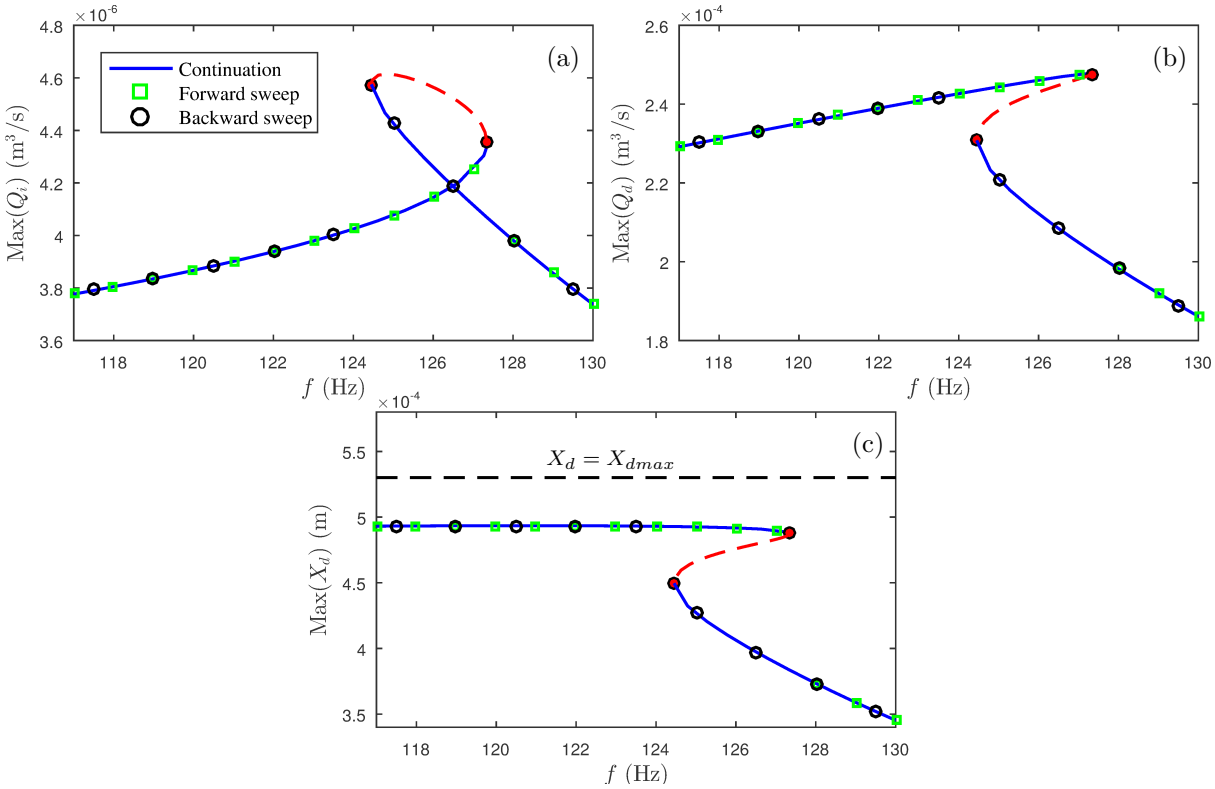

Fig. 6.8 Frequency responses of (a) maximum Q_i, (b) maximum Q_d, (c) maximum X_d using continuation and time-stepping method (forward and backward sweep excitations).

6.3 Beneficial fluid-passageway layout identifications using the linearised model

In this section, the low-frequency linearised engine mount model is used. Beneficial fluid passageway configurations, which are aimed at minimising the maximum low-frequency displacement transmissibility, are identified. The decoupler dynamics are excluded as its influence on low-frequency performance is slight. Two types of fluid passageways are considered, one is the capillary inertia track and the other one is flow restriction.

6.3.1 Optimisation procedure and candidate layouts

Considering optimisations with the linearised low-frequency model, the $\max(|T_d|)$ over $0 < f \leq 30$ Hz is chosen as the objective function. As introduced in Section 6.2.2, the default value of the objective function, $\max(|T_d^*|)$ (the * indicates the default system), is 3.64. Considering the practical implementation, the fluid passageway types considered in this analysis are the inertia track and a flow restriction. The inertia track will be modelled as a long capillary tube with circular cross-section shape, allowing the inertance and damping to be expressed as

$$I_i = \rho \frac{L_i}{A_i}, \tag{6.17}$$

$$R_i = \frac{128 \mu L_i}{\pi {d_i}^4}, \quad A_i = \frac{\pi {d_i}^2}{4}, \tag{6.18}$$

where μ is fluid dynamic viscosity and d_i is the diameter of the inertia track. Details about nonlinear flow restriction characteristics for orifice are introduced in Section 6.4.2. Here for simplification, it is assumed the damping associated with the flow restriction to be modelled as a linear viscous damping R_o. We define the optimisation parameters, the variations of inertia track geometry and the restriction damping, as

$$\text{Inertia track:}, \quad \delta_L = L_i / {L_i}^*, \quad \delta_A = A_i / {A_i}^*, \tag{6.19}$$

$$\text{Flow restriction:}, \quad \delta_o = R_o / {R_i}^*, \tag{6.20}$$

with the parameter constraints $0.5 \leq \delta_L \leq 1.5$, $0.5 \leq \delta_A \leq 1.5$, $\delta_o > 0$. Here we choose $\pm 50\%$ constraints on inertia track geometry [72, 73, 166]. Such constraints may be adjusted further according to requirements from manufactures.

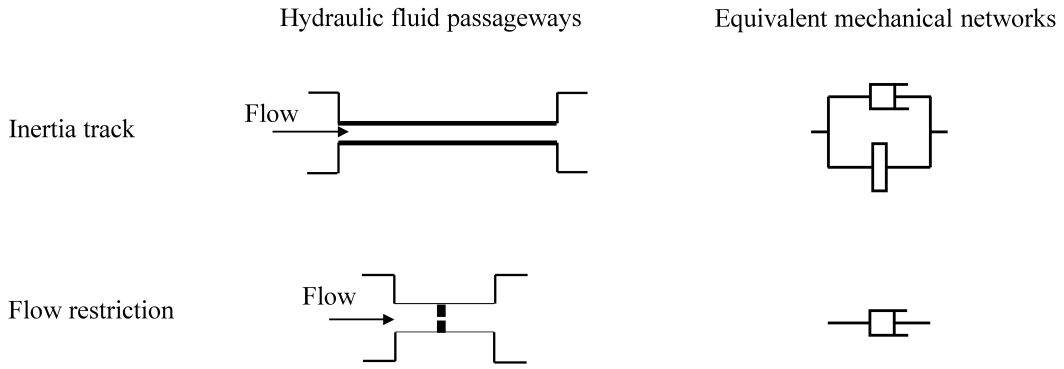

Fig. 6.9 Shown are fluid passageway representations and the equivalent mechanical networks of the inertia track and the flow restriction, respectively. Note here thin lines used in a flow restriction are to stress its negligible length of the practical hydraulic passageway.

Number of fluid passageways	Network topologies	Number of topologies
1		1
2		2
3	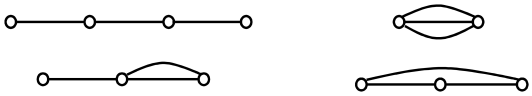	4
4	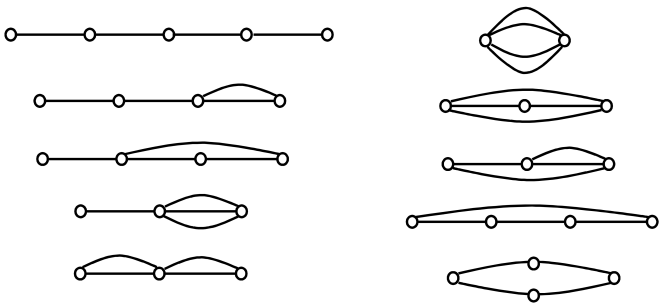	10

Fig. 6.10 All candidate network topologies with up to four fluid passageways.

The hydraulic fluid passageways considered, namely, the inertia track and the flow restriction, can be represented as a parallel damper-inerter mechanical layout or a single damper, respectively, as indicated in Fig. 6.9. With a predetermined number of fluid passageways involved, all possible network topologies can be achieved based on a systematic standard procedure proposed for generating two-terminal series-parallel electrical networks [180]. Considering the difficulty of design and manufacture, layouts

with at most four fluid passageways are considered here. All possible network topologies are summarised in Fig. 6.10, where each branch between circular nodes represents either an inertia track or flow restriction. Note that following the standard procedure more complex layouts with more fluid passageways may be achieved if necessary. The general layouts can also be achieved following the structure-immittance approach proposed in [87] (see Section 2.3.3). The difference is that in [87] the authors propose the layouts based on the component level (spring, damper or inerter) while, in this case, one would apply it at a device level (using inertia track and flow restriction).

Using the network topologies illustrated in Fig. 6.10, we can formulate the transfer functions for all equivalent mechanical networks consisting of up to four fluid passageways and perform the optimisations. Based on the optimal mechanical networks, the practical hydraulic fluid passageways will be identified. For the optimisations carried out in the present work, the Matlab command `patternsearch` is used first and then `fminsearch` for fine-tuning of the parameters.

6.3.2 Optimal results

The optimisation results based on minimising the low-frequency displacement transmissibility due to road inputs are summarised in Table 6.2. Two improvement measures are used in the following discussions, Δ_d is a comparison with the default configuration, Δ_{do} is a comparison with the optimal solution using the default layout. Note that we use the notation 'M_{mn}' to specify the mechanical network layout while using 'H_{mn}' to specify the hydraulic ones. The subscripts 'm' and 'n' are used to specify the nth beneficial network of the ones consisting of m fluid passageways. The corresponding beneficial mechanical layouts are shown in Fig. 6.11, as well as schematic representations of the equivalent hydraulic passageways.

It can be seen from Table 6.2 that the default layout with optimised inertia track geometry can provide a significant improvement, which is 35.71% comparing with the default system. This indicates that the default engine mount provides sub-optimised displacement transmissibility performance and altering the inertia track geometry will improve the performance significantly. Further performance benefits are found if the flow restrictions are included in the design, with up to 54.12% improvement using M_{42} comparing with the default system and 28.63% improvement comparing with the optimal M_1. As shown in Fig. 6.11 that the layout M_{42} consists of three inertia tracks and one flow restriction. It can be seen that increasing the layout complexity leads to increasing improvements, however, the rate of improvements when more passageways are added drops off rapidly. Comparing with the results of M_{21} and M_{22} the improvements obtained

Table 6.2 Optimisation results using a linearised low-frequency model

Layouts	Performances			Parameter values
	max($\lvert T_d \rvert$)	Δ_d (%)	Δ_{do} (%)	(see Eqs. (6.19), (6.20))
Default	3.64	-	-	-
M_1(optimal default)	2.34	35.71	-	$(\delta_L, \delta_A) = (0.5, 0.65)$
M_{21}	1.79	50.82	23.50	$(\delta_L, \delta_A) = (1.5, 1.03)$, $\delta_o = 5.07$
M_{22}	1.76	51.65	27.79	$(\delta_L, \delta_A) = (0.76, 1.22)$, $\delta_o = 1.85$
M_3	1.69	53.57	27.78	$(\delta_{L1}, \delta_{A1}) = (1.5, 0.88)$, $(\delta_{L2}, \delta_{A2}) = (0.5, 1.19)$, $\delta_o = 2.43$
M_{41}	1.69	53.57	27.78	$(\delta_{L1}, \delta_{A1}) = (1.5, 1.27)$, $\delta_{o1} = 0.44$, $(\delta_{L2}, \delta_{A2}) = (0.52, 1.19)$, $\delta_{o2} = 1.90$
M_{42}	1.67	54.12	28.63	$(\delta_{L1}, \delta_{A1}) = (1.5, 1.36)$, $(\delta_{L2}, \delta_{A2}) = (1.5, 1.42)$, $(\delta_{L3}, \delta_{A3}) = (0.57, 1.16)$, $\delta_o = 3.55$

by M_3, M_{41} and M_{42}, balanced with the additional manufacturing complexity, will arguably make these configurations less attractive. Hence we disregard M_3, M_{41} and M_{42} as being beneficial here. The low-frequency $|T_d|$ performances in frequency domain obtained with the default and beneficial configurations M_1, M_{21} and M_{22} are shown in Fig. 6.12. Note that these optimisation results are obtained based on the linearised low-frequency model that neglects the decoupler effects. It is worth to investigate the effects of the decoupler, on the performances of these beneficial solutions. Also, the high-frequency performances need to be investigated.

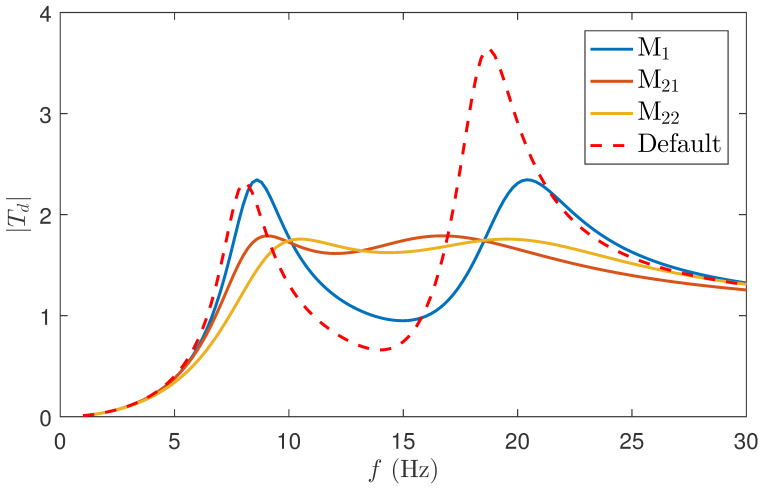

Fig. 6.12 $|T_d|$ performances with the default and beneficial configurations M_1, M_{21} and M_{22}.

Cases	Equivalent mechanical networks	Hydraulic fluid passageways
M_1	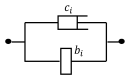	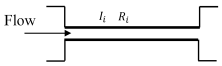
M_{21}	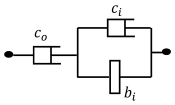	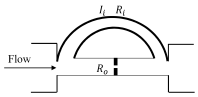
M_{22}	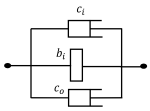	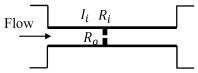
M_3	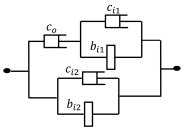	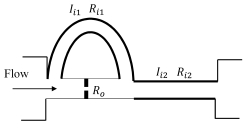
M_{41}	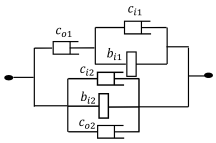	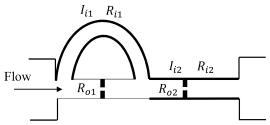
M_{42}	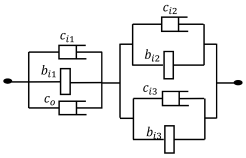	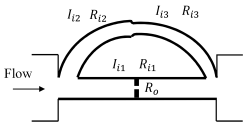

Fig. 6.11 Beneficial mechanical layouts and the equivalent hydraulic passageways.

6.4 Extended optimisations considering system nonlinearity

In this section, the effects of the decoupler on the low-frequency displacement transmissibility achieved by the linearly optimised solutions are investigated, using the nonlinear model introduced in Section 6.2.1. The beneficial configurations, M_1, M_{21} and M_{22} are considered. The high-frequency $|K_{dyn}|$ performances are also analysed with these solutions. Then to illustrate the impacts of nonlinearity on the optimal performances over a wide range of frequencies, we extend the optimisations to that using the nonlinear engine mount model. At most two flow passageways (the inertia track and the nonlinear flow restriction) are considered in the nonlinear optimisations. The low-frequency displacement transmissibility is still used as the objective function to be minimised while high-frequency $|K_{dyn}|$ will be controlled as a constraint. Note that this high-frequency constraint can not be applied in the linearised model as the effects of decoupler lost. The sensitivity analyses of low-frequency performances to such constraint are also examined.

6.4.1 Effects of decoupler nonlinearity on linearly optimised configurations

The effects of the decoupler on low-frequency performance benefits for the linearly optimised configurations still needs to be checked. Table 6.3 summarised the low-frequency $\max(|T_d|)$ achieved by the beneficial configurations, M_1, M_{21} and M_{22} in Table 6.2, with the nonlinear model introduced in Section 6.2.1. The $\max(|T_d|)$ performances achieved with the linear model (column 2 in Table 6.2) are also presented as a reference. It can be seen from Table 6.3 that the trend of a reduced $|T_d|$ with the increase of network complexity observed with the linear analysis still holds for the nonlinear model. Fig. 6.13 shows the comparison between the linear and nonlinear $|T_d|$ responses obtained with the default and M_{22} cases. It can be observed that for the difference between the linear and nonlinear responses obtained with optimised M_{22} is more significant than that of the default system.

Table 6.3 Nonlinear performances using linearly optimised configurations

Configurations	Low frequency				High frequency
	$\max(\|T_d\|)$ (linear)	$\max(\|T_d\|)$ (nonlinear)	Δ_d (%)	Δ_{do} (%)	$\max(\|K_{dyn}\|)$ (N/m)
Default	3.63	3.45	-	-	701985
M_1	2.34	2.34	35.52	-	706983.5
M_{21}	1.79	1.89	47.81	19.06	687134.5
M_{22}	1.76	1.85	49.01	20.92	711052

In addition to the effect of nonlinearity on the low-frequency performance it is interesting to consider the effect of linearly optimising the low-frequency performance on the high-frequency dynamics. The high-frequency $|K_{dyn}|$ performances obtained by the nonlinear model with linearly optimised solutions are shown in Fig. 6.14 and the max($|K_{dyn}|$) values are summarised in the last column of Table 6.3. It can be seen that the max($|K_{dyn}|$) of M_1 and M_{22} slightly exceed what is obtained by the default system but M_{21} provides a lower max($|K_{dyn}|$).

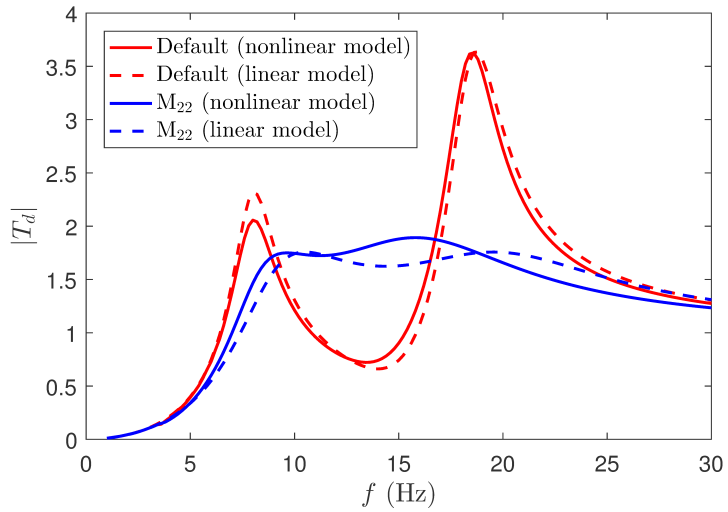

Fig. 6.13 Comparison between the linear and nonlinear low-frequency $|T_d|$ responses with the default and optimised M_{22}.

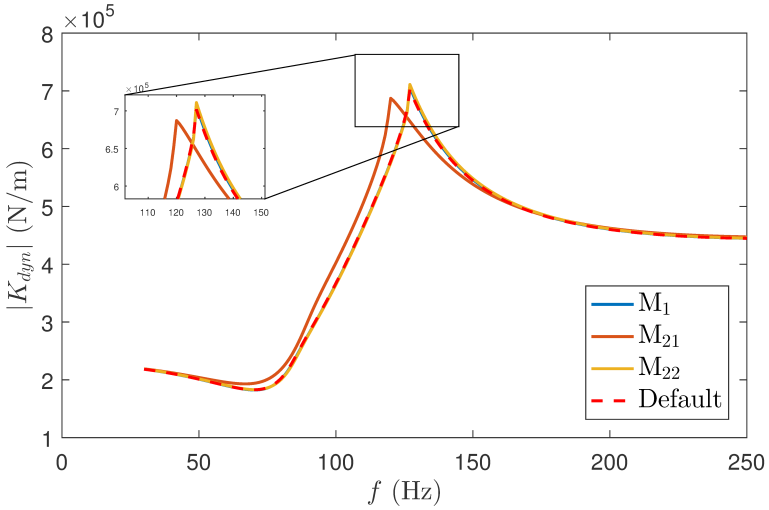

Fig. 6.14 High-frequency responses obtained with linearly optimised configurations M_1, M_{21} and M_{22} using time-stepping technique.

Furthermore, a linear restriction damping was assumed for optimisation in Section 6.3 while, in practical use, the pressure drop vs. flow rate relationship for a flow restriction is not linear. So it is necessary to consider a high-frequency performance constraint and extend the optimisations with the decoupler and nonlinear restriction for optimal design.

6.4.2 Optimisation including the decoupler and flow restriction nonlinearities

In this section, the $\max(|T_d|)$ for which $0 < f \leq 30$ Hz is still regarded as the objective function. A performance constraint that the $\max(|K_{dyn}|)$ is no larger than the default system, namely, $\max(|K_{dyn}|) \leq 701985$ N/m, $30 < f \leq 250$ Hz where 701985 N/m is the default value. Note that time-stepping method will be used for optimisations then the high-frequency performances will be checked with continuation. The layouts with up to two fluid passageways are considered, which specifically are the layouts with single inertia track (default system), two inertia tracks (in parallel or in series), and one inertia track and one restriction (in parallel and in series). The parameter constraints for inertia track introduced in Section 6.3.1 are kept. In this analysis, orifice is considered as an example physical flow restriction realisation to illustrate the benefits. The orifice characteristics will be introduced in Section 6.4.2, as well as the corresponding parameter constraints.

Optimal design with single and two inertia tracks

Two sets of optimisations, one with a constraint that the high-frequency $|K_{dyn}|$ is no larger than the default and the other with no such constraint, are considered and the results are summarised in Table 6.4. The subscripts 'Imk' are used to represent the case considering $|K_{dyn}|$ constraint, I denotes this optimisation only considering the inertia track and m is the number of inertia tracks ('Im' for the case without $|K_{dyn}|$ constraint). Note that the optimal design of two inertia tracks in series hydraulically is equivalent with the optimal single inertia track solution hence it is not included in the table. H_{I2k} or H_{I2} here refers to the layout with two inertia tracks in parallel hydraulically. It can be seen that if the $\max(|K_{dyn}|)$ is constrained, a 25.51% improvement is obtained with the optimal H_{I1k} configuration while with two parallel inertia tracks this improvement can only be further increased by 0.39%. However, if the high-frequency constraint is ignored, a significant improvement, which is up to 11.40%, can be achieved with the optimal H_{I2} comparing with optimal H_{I1}. From the optimum parameter values, we observe that the two inertia tracks of H_{I2} have the same cross-section area but different lengths, so the inertances and dampings of two tracks are proportional to each other. From the network

point of view, the optimal H_{I2} is equivalent with a single inertia track but H_{I1} provides less performance advantage due to the geometry constraint.

Table 6.4 Optimal solutions with single or two parallel inertia tracks

Configurations	Low frequency			High frequency	Parameter values
	Max($\|T_d\|$)	Δ_d (%)	Δ_{do} (%)	Max($\|K_{dyn}\|$) (α_k)	
Default	3.45	-	-	701985	-
H_{I1k}	2.57	25.51	-	701985(0)	$(\delta_L, \delta_A) = (0.5, 0.51)$
H_{I2k}	2.56	25.80	0.39	701985(0)	$(\delta_{L1}, \delta_{A1}) = (0.88, 0.5)$, $(\delta_{L2}, \delta_{A2}) = (1.11, 0.5)$
H_{I1}	2.28	33.91	-	707912(0.84%)	$(\delta_L, \delta_A) = (0.5, 0.67)$
H_{I2}	2.02	41.45	11.40	708656(0.95%)	$(\delta_{L1}, \delta_{A1}) = (0.88, 0.5)$, $(\delta_{L2}, \delta_{A2}) = (0.6, 0.5)$

For both optimal configurations H_{I1} and H_{I2}, the max($|K_{dyn}|$) will exceed the default value by 0.84% and 0.95%, respectively, and we use α_k to represent this variation,

$$\alpha_k = \frac{\max(|K_{dyn}|) - \max(|K^*_{dyn}|)}{\max(|K^*_{dyn}|)}. \tag{6.21}$$

Fig. 6.15 shows the low-frequency and high-frequency performances achieved with the default and optimal H_{I1} and H_{I2}. The continuation method is also used to obtain the exact max($|K_{dyn}|$) performance. The optimisations above indicate that the inclusion of $|K_{dyn}|$ constraint limits the low-frequency performance benefits of new designs. If we relax the high-frequency constraint very slightly, such as by 0.95%, the low-frequency objective function improves significantly.

A further investigation into the sensitivity of the low-frequency max($|T_d|$) to the $|K_{dyn}|$ constraint is therefore necessary. Specifically, the variation of $|K_{dyn}|$ constraint value, as defined by α_k, is set to be within [-1.0%, 1.5%]. For different high-frequency constraint value, optimum tuning for both H_{I1k} and H_{I2k} are performed and the results are illustrated in Fig. 6.16. It can be seen that when α_k is increased from -1.0% to 1.5%, the optimal low-frequency max($|T_d|$) for both H_{I1k} and H_{I2k} are significantly sensitive to α_k. The improvement of low-frequency $|T_d|$ is compromised by high-frequency $|K_{dyn}|$, which suggests a trade-off between the two performance criteria. It can also be seen that no matter the value of α_k is, the design with two parallel inertia tracks is always more beneficial than the single inertia track case.

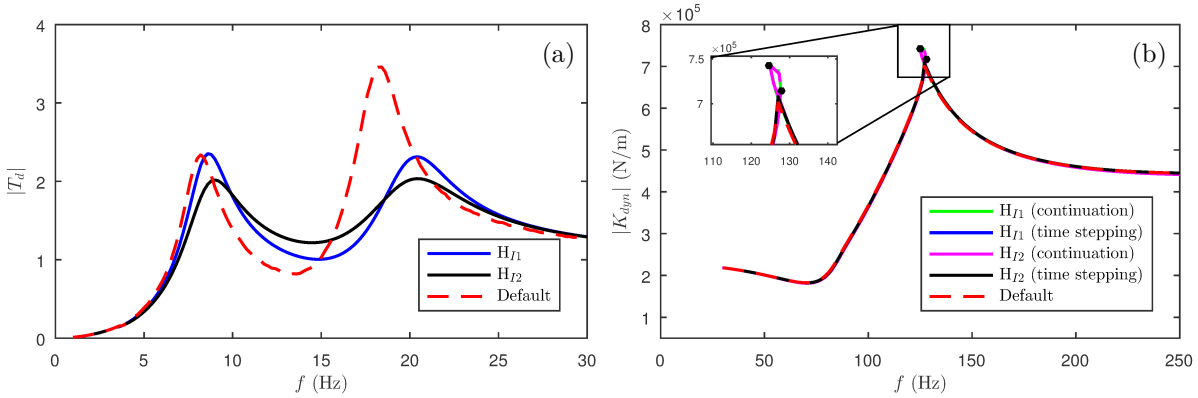

Fig. 6.15 With the default, H$_{I1k}$ and H$_{I2k}$ configurations, shown are (a) $|T_d|$ frequency performances and (b) $|K_{dyn}|$ frequency responses with time-stepping and continuation techniques. The fold bifurcation points are marked by black points.

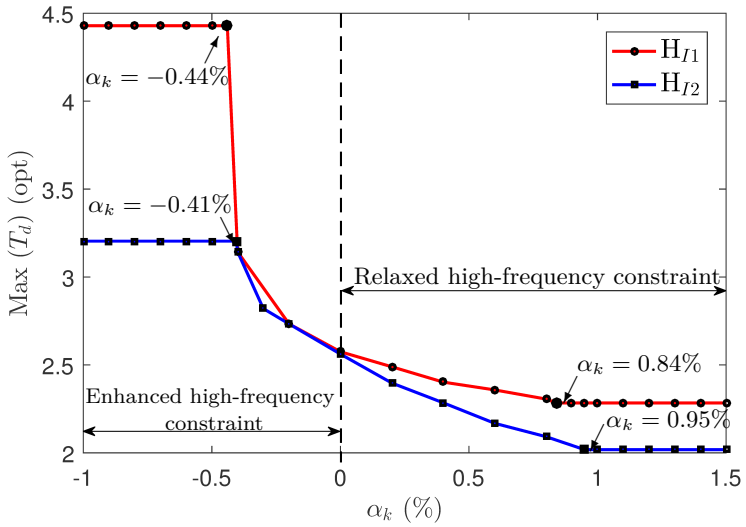

Fig. 6.16 Sensitivity analysis of α_k on the low-frequency max($|T_d|$) for H$_{I1k}$ and H$_{I2k}$.

The worst $|T_d|$ performances exist when $\alpha_k = -0.44\%$ (H$_{I1k}$) and $\alpha_k = -0.41\%$ (H$_{I2k}$). With such worst $|T_d|$ performances, the maximum dynamic stiffness can only be reduced by 0.44% for H$_{I1k}$ or 0.41% for H$_{I2k}$, while no more further reduction can be obtained. When α_k is approaching these worst cases backward, the $|T_d|$ performances experience a sharp increase.

Model for the orifice

Fig. 6.17 illustrates a typical symmetric orifice flow restriction. D_o and D_1 are the orifice and upstream pipe diameters, respectively. Different from the linear system analysis, the

nonlinear characteristics for a restriction, of which the pressure-flow model [181], are considered here, as given by

$$\Delta P = \frac{Q_o}{|Q_o|}\frac{\rho}{2K^2A_o^2}Q_o^2, \tag{6.22}$$

where ρ is the fluid density, Q_o is the flow rate across the restriction, K represents flow coefficient and A_o is orifice cross-section area. A diameter ratio β is defined as D_o/D_1, then $\beta = \sqrt{A_o/A_1}$, where A_1 is the upstream cross-section area. In the relationship expressed by Eq. (6.22), the flow is assumed to be steady, incompressible and symmetric along a streamline. For a standardised restriction, sufficient test data has been used to develop the empirical equations for predicting the empirical flow coefficient K based on specified restriction type, diameter ratio and Reynolds number. In this analysis the concentric orifice case with corner pressure taps is considered and the empirical equation for predicting K [182] is

$$K = K_o(1 + b\lambda), \quad b = (0.002 + 0.026\beta^4)K_o, \tag{6.23}$$

$$K_o = 0.6004 + 0.35\beta^4 - 0.052(0.5 - \beta)^{(3/2)} - 0.62(\beta - 0.7)^{(5/3)}, \tag{6.24}$$

$$\lambda = \frac{1000}{\sqrt{Re_{D1}}}, \quad Re_{D1} = \frac{\rho|\overline{V_1}|D_1}{\mu}, \tag{6.25}$$

where Re_{D1} is pipe Reynolds number, $\overline{V_1}$ is flow velocity in the upstream pipe and the dynamic viscosity μ is chosen as 0.02Ns/m^2 [183]. For the case in which the orifice is configured in the inertia track, an assumption that $0.1 < \beta < 0.82$ is made [182] to ensure sufficient accuracy of Eqs. (6.23)-(6.25). If the inertia track and the orifice are configured in parallel hydraulically, the upstream of the orifice will be the upper chamber which has a quite large cross-section area comparing with that of the orifice and then the variation of K is insensitive to Re_{D1}. In this case, a constant K, i.e. 0.60, is assumed in the calculation. Note that we are aware that this model of predicting flow coefficient is not precise for all working conditions. For practical damper design, the effects of various factors, such as temperature, on the orifice characteristics need to be emphasised and the precise model to be verified with experimental data fitting. However, this is beyond the scope of this work which is to investigate the potential of innovative fluid passageway design concepts and propose a systematic optimum design approach.

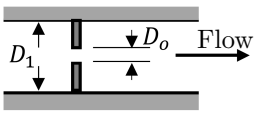

Fig. 6.17 Schematic of a typical symmetric orifice and one of the flow directions.

Optimal design with one inertia track and one nonlinear orifice

The nonlinear flow restriction, which is orifice here, is considered as a fluid passageway type here. The designs with one inertia track and one nonlinear orifice (in parallel H_{21o} and in series H_{22o} hydraulically) are optimised here and the subscripts 'o' are used to represent the cases considering orifice. Similarly, optimisations are carried out with and without the high-frequency constraint and the results are summarised in Tables. 6.5 and 6.6.

Table 6.5 Optimal solutions with a nonlinear orifice (with $|K_{dyn}|$ constraint).

Configurations	Low frequency			High frequency	Parameter values
	Max($\|T_d\|$)	Δ_d (%)	Δ_{do} (%)	Max($\|K_{dyn}\|$) (α_k)	
Default	3.45	-	-	701985	-
H_{I1k}	2.57	25.51	-	701985(0)	$(\delta_L, \delta_A) = (0.5, 0.51)$
H_{21ok}	1.97	42.90	13.60	500972.6 (-28.63%)	$(\delta_L, \delta_A) = (1.48, 1.05)$, $D_o = 5.42$ mm
H_{22ok}	2.36	31.60	8.17	701985(0)	$(\delta_L, \delta_A) = (0.98, 1.06)$, $D_o = 7.21$ mm

If the constraint is applied, the optimal H_{21ok} configuration provides the maximum improvement on the objective function here, which is 13.60% comparing with the optimal H_{I1k}. It should be noted that the achieved max($|K_{dyn}|$) is much lower than the default system, i.e., 28.63% reduction, which is beneficial for high-frequency isolation performance. The use of an orifice in H_{22ok} will reduce the low-frequency objective function by 8.17% comparing with the optimised default configuration. When the high-frequency constraint is ignored, the maximum improvement is obtained with H_{22o}, which is 17.54% comparing with the optimal H_{I1}. The results of H_{21o} are the same as the case H_{21ok}. The low-frequency $|T_d|$ and high-frequency $|K_{dyn}|$ responses are illustrated in Fig. 6.18 with time-stepping method. Fig. 6.19(a) shows all the high-frequency responses obtained with continuation method. It can be seen that H_{21ok} can significantly reduce the high-frequency $|K_{dyn}|$ as under high-frequency excitations, more fluid will flow through the orifice rather the decoupler and produce a smaller effective damping in the system, hence reducing the $|K_{dyn}|$.

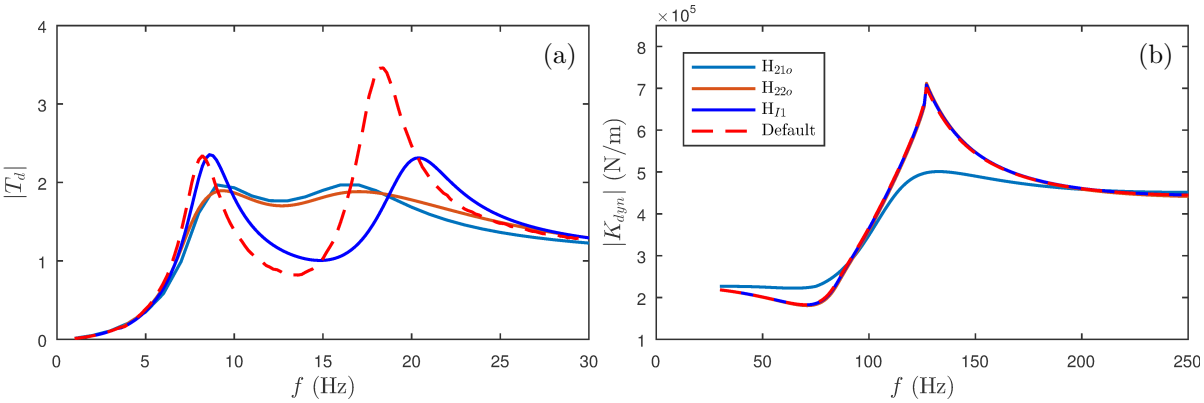

Fig. 6.18 With the default, H_{I1}, H_{21o} and H_{22o} configurations, shown are (a) $|T_d|$ frequency performances and (b) $|K_{dyn}|$ frequency responses.

Table 6.6 Optimal solutions with a nonlinear flow restriction (without $|K_{dyn}|$ constraint).

Configurations	Low frequency			High frequency	Parameter values
	Max($|T_d|$)	Δ_d (%)	Δ_{do} (%)	Max($|K_{dyn}|$)	
Default	3.45	-	-	701985	-
H_{I1}	2.28	33.91	-	707912(0.84%)	$(\delta_L, \delta_A) = (0.5, 0.67)$
H_{21o}	1.97	42.90	13.60	500972.6 (-28.63%)	$(\delta_L, \delta_A) = (1.48, 1.05)$, $D_o = 5.42$ mm
H_{22o}	1.88	45.51	17.54	711742.9 (1.39%)	$(\delta_L, \delta_A) = (0.59, 0.95)$, $D_o = 6.83$ mm

A similar sensitivity analysis is also conducted to explore the impacts of the $|K_{dyn}|$ constraint value on low-frequency objective function for H_{22ok}. The results are shown in Fig. 6.19(b) and H_{I1k} is used as a reference. Comparing with H_{I1k}, the optimal H_{22ok} configuration can provide significant performance benefits when the constraint is relaxed. This is similar with the results obtained with H_{I2k} (two parallel inertia tracks, see in Fig. 6.16), but comparing with H_{I2k}, a more relaxed $|K_{dyn}|$ constraint value is required if H_{22ok} provides the largest improvement.

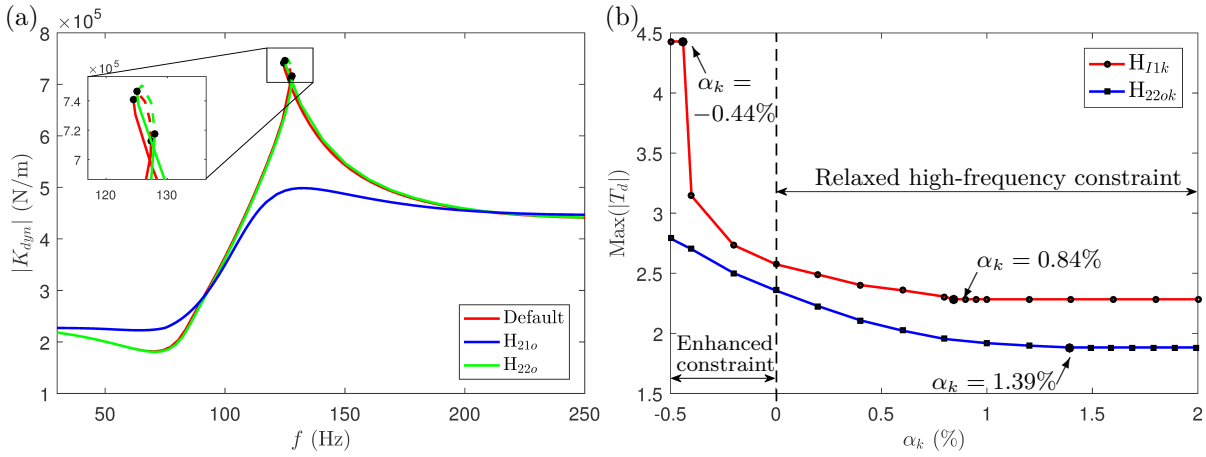

Fig. 6.19 (a) Comparison of high-frequency $|K_{dyn}|$ responses using continuation method. The fold bifurcation points are marked by black points. (b) Sensitivity analysis of α_k on the low-frequency $\max(|T_d|)$ for H_{I1k} and H_{22ok}.

6.5 Concluding remarks

In this chapter steady-state vibration suppression was considered and the optimal device physical arrangement was investigated. Specifically, the performance benefits of a hydraulic engine mount with tailored fluid passageways on suppressing steady-state oscillations were analysed, considering the performance criteria at different frequency bands. A systematic optimum design approach to identify such fluid passageway arrangements was proposed. It was shown that, for the engine mount with the identified optimum fluid passageway configurations, the maximum low-frequency displacement transmissibility can be improved significantly while only deteriorated the high-frequency dynamic stiffness slightly. This mechanical design procedure, which takes advantages of network synthesis theory and mechanical-electrical-hydraulic analogy, is applicable to other hydraulic or interdisciplinary devices.

Firstly a nonlinear model of a conventional hydraulic engine mount was reviewed, alongside a linearised low-frequency model that ignores the effects of decoupler. It was shown that the effects of decoupler dynamics were slight on low-frequency performance. Then first we used the low-frequency linearised model to minimise the maximum low-frequency displacement transmissibility. By optimising over all possible networks with up to four fluid passageways while considering geometry constraints, it was seen that increasing the layout complexity leaded to increasing improvements. However, comparing with the layouts with low complexity, these improvements were very slight. Hence we regarded the configurations with two fluid passageways, one inertia track and one flow restriction,

as beneficial. The configuration of one inertia track and one flow restriction in hydraulic series provided up to 51.65% performance improvement over the default system and 27.79% improvement over the optimised default layout. With linearly optimised solutions, it was found that the low-frequency responses obtained using a nonlinear model were affected notably by the nonlinearity from the decoupler mechanism and the high-frequency performances deteriorated slightly with linearly optimised solutions.

To illustrate the impacts of nonlinearity on the optimal performances over a wide range of frequencies, we extended the optimisations to that using the nonlinear engine mount model. The maximum low-frequency displacement transmissibility was still used as the cost function while a constraint on the high-frequency dynamic stiffness was included. At most two flow passageways (the inertia track and the nonlinear flow restriction) were considered in the nonlinear optimisations. It was shown that with the high-frequency constraint, which restricts the maximum high-frequency dynamic stiffness amplitude to be no larger than the default, the improvements provided by the configurations with only inertia tracks on the maximum low-frequency displacement transmissibility were limited. However, it was found that an up to 42.90% performance improvement, which was 13.60% improvement over the optimised default layout, was obtained with one inertia track and one orifice configured in parallel hydraulically. This configuration also reduced the high-frequency maximum dynamic stiffness amplitude by 28.63% over the default system.

Via a sensitivity analysis of low-frequency performances to high-frequency constraint, it was seen that if the high-frequency constraint was relaxed slightly, the maximum low-frequency displacement transmissibility could be further improved significantly. Comparing with the improved default system, up to 17.54% improvement on low-frequency cost function was identified for the configuration with one orifice and one inertia track in hydraulically series, which only compromises the high-frequency performance criteria by 1.39%.

Chapter 7

Conclusions and future work

This thesis established the methodologies for optimal design of passive vibration suppression devices for both configurations and physical arrangements. Several typical vibration suppression problems were tackled. It also demonstrated the potential advantages of introducing inerters in each case. In this chapter, a summary of the results and the drawn conclusions are presented, alongside a discussion of potential avenues of further work.

7.1 Conclusions

This section summarises the conclusions for the development of optimal design methodologies for both configurations and physical device arrangements of passive vibration suppressors and the effectiveness on dealing with the three typical problems. In addition, the obtained performance advantages of inerter-based devices for each case study are also concluded.

7.1.1 Optimal design methodologies for passive vibration-suppression-device configurations

This thesis firstly concentrated on the optimal design of vibration-suppression-device configurations. Here, the term *configuration* represents the topological arrangement of components that are ideal passive springs, dampers and inerters, as well as their parameter values. Appropriate design methodologies were proposed, for each vibration suppression problem, to identify the optimal configurations of passive suppressors.

Transient vibrations were regarded as ones triggered by external deterministic but aperiodic excitations, which could experience a short or long duration, and normally

decay to zero after a period. This thesis focused on the suppression of transient vibrations caused by initial excitations with short periods, which were moderate perturbations and initial impact. This work suggested the time-domain based method to measure transient vibrations, define the performance criteria according to the design requirements and carry out the optimisations.

Specifically, we first considered how to suppress transient vibrations excited by initial moderate perturbations via using linear passive suppression devices in Chapter 3. Here, we focused on the shimmy transient decays in the Fokker 100 MLG system. A linear model was presented to capture the gear's oscillations, which were the torsional-yaw, lateral and torsional-roll motions. The conventional shimmy damper was located between the apex point between the upper and lower torque links, to provide more damping to the torsional-yaw motion. Such shimmy damper would be altered with the candidate layouts proposed using both structure- and immittance-based approaches. Initially a frequency-domain optimisation was conducted to maximise the damping ratio among all the system modes. It was observed that while the lowest damping ratio was increased significantly, the transient vibrations deteriorated compared with the default shimmy damper. This suggested that the frequency-domain technique was deficient for this problem in which the system mode shapes were significantly changed when certain suppression devices were varied. Based on this observation we found that for a system with coupled modes, time-domain technique was more convenient when analysing the transient vibrations given the cost functions being considered. Two perturbations applied to the tyre were considered to trigger the gear transient response. For the optimisations, two example time-domain performance criteria, the maximum amplitude and the settling time of the torsional-yaw motion, were used as the cost functions. Different optimal configurations were identified corresponding to the cost function and the input used.

The second type of transient vibrations considered was an impact problem. In Chapter 4, the aircraft landing gear touch-down process was analysed. The shock absorber unit was to be optimised to provide enhanced touch-down performances, namely, the strut efficiency, the maximum strut load to the frame and the maximum stroke. According to the design requirements, it was also essential to include an energy dissipation constraint into the optimal design process of shock absorbers – this was to avoid imposing additional challenges in energy dissipation for the elongation stage of the process. The performances obtained with a conventional nonlinear oleo-pneumatic shock absorber were regarded as the baseline. Temporarily ignoring the energy dissipation constraint, a number of beneficial shock strut layouts were identified, by using both structure- and immittance-based design approaches. However, when implementing the energy dissipation constraint, it was observed that the benefits provided by such beneficial layouts were limited. This

was mainly because a linear supporting spring was needed and compared with the nonlinear one, more potential energy was stored at the end of touch-down rather than being dissipated. It was then found that the performance was strongly dependent on the energy dissipation constraint, and by relaxing the constraint slightly quickly led to improvements in the cost functions. Additionally, we proposed absorbers using a nonlinear supporting spring with progressive rates, namely double-stage spring, which have been shown to be beneficial for storing less potential energy and provide enhanced touch-down performances.

Self-excited vibrations are a special class of vibrations that can affect structures through indirect excitation. For a nonlinear dissipative system, periodic oscillations with bounded amplitudes, e.g. LCOs, are generated. There is essential to investigate the local stability of such periodic oscillations and avoid the occurrence of instability with vibration suppressors. Numerical continuation is a valuable tool for finding the branches of periodic solutions when varying the operational and design parameters. This technique is suited to analysing the ability of suppression devices to resist self-excited vibrations. A method of selecting the suppression device parameter values to prevent the instability of self-excited oscillations using numerical continuation was proposed in this thesis.

In detail, Chapter 5 showed optimal damper designs for suppressing shimmy instability in aircraft landing gears using the proposed method. A nonlinear reduced-order model was developed to capture the dual-wheel MLG dynamics equipped with the shimmy-suppression device. Using numerical continuation, two-parameter bifurcation diagrams were obtained with the variations of the aircraft forward speed and a device parameter, e.g. the damping coefficient. We defined that a region in the device parameter space where no sustained shimmy oscillations occur over the entire operating speed range as the zero-shimmy region. It was demonstrated that for the conventional shimmy damper this zero-shimmy region was quite narrow. Using the proposed design method, the obtained beneficial shimmy-suppression devices were capable of expanding the zero-shimmy region significantly. They may potentially improve the device's robustness to shimmy instability over the full operational speed.

7.1.2 Optimal design approach for physical device arrangement

As for the design of passive vibration suppression devices, not only the layouts and the parameter values, one also needs to consider the physical constraints, for example due to manufacture, and also the involved device nonlinearities at the design stage. Therefore in this thesis a systematic approach for designing the physical arrangement in a vibration suppressor was also established. This approach that makes use of network synthesis theory

and mechanical-electrical-hydraulic analogy is applicable to other hydraulic, pneumatic or interdisciplinary devices.

In Chapter 6, we considered the physical design, the fluid passageways, in a hydraulic engine mount for an automotive vehicle to suppress **steady-state vibrations**. Such vibrations can result in shortening the structure fatigue life. To suppress such vibrations it is important to apply absorbers providing frequency- and amplitude-dependent vibration suppression behaviour.

A conventional hydraulic engine mount included one fluid passageway, inertia track, and a decoupler, which could be altered to improve the dynamic performance. With the proposed approach, all possible network topologies with a predetermined number of fluid passageways involved were explored in a systematic manner, rather than in a 'trial and error' way that was used in the previous literature. In the design process, it was easy to implement the geometry constraints of fluid passageways to guarantee the implementability in practical applications. Two types of fluid passageways were considered in this work, which were the capillary inertia track and the flow restriction.

A linearised low-frequency engine mount model was presented first to capture the mount's low-frequency performance, i.e. the low-frequency displacement transmissibility with respect to the road input. Considering the difficulty of design and manufacture, all possible networks with up to four fluid passageways that had linear characteristics were optimised with geometry constraints to be satisfied. Based on this model, it was shown that increasing the layout complexity resulted in further reductions of the maximum low-frequency displacement transmissibility. However, comparing with the layouts with low complexity, these improvements were very slight. To address the high-frequency dynamics and nonlinear flow characteristics, a nonlinear engine mount model over a full-frequency range was then considered. Based on this model, the beneficial layouts obtained from low-frequency linear optimisations were re-optimised to guarantee that the maximum high-frequency dynamic stiffness was no larger than that of the default system. Using optimisations it was found that for most of the designs, if the high-frequency constraint was relaxed slightly, the maximum low-frequency displacement transmissibility could be further improved significantly. While the arrangement with one inertia track and one orifice configured in parallel hydraulically could provide significant improvements on both low- and high-frequency performances.

7.1.3 The potential benefits of passive inerter-based vibration suppression

This thesis investigated the potential of using inerter for suppressing different vibration behaviours. The inerter, a passive mechanical device that generates the force proportional to the relative accelerations between its terminals, has been shown to fundamentally enlarge the range of dynamic properties that can be achieved via passive absorbers. Using the mechanical-electrical-hydraulic analogy, it is equivalent to an electrical capacitor or a hydraulic inertance. Performance advantages of inerter-based vibration suppression systems have been demonstrated in various engineering structures, such as road vehicle, building, railway vehicle, cable and motorcycle. In this thesis, inerter-based applications in the aircraft landing gear systems were explored.

In Chapters 3 and 4, we analysed the potential of suppressing transient oscillations, which were stable transient shimmy and landing touch-down vibrations, using inerter-based passive suppression devices. For the shimmy suppression case, the parallel inerter-spring-damper layout was identified as beneficial for reducing the maximum oscillation amplitude and the settling time. It was shown that in this layout, the inclusion of inerter provided significant performance benefits over the gear geometric modification and the optimised traditional parallel spring-damper design. As for the touch-down performances, the landing efficiency, the maximum strut load and the maximum stroke, were improved significantly by inerter-based shock struts, comparing with non-inerter configurations. However, since the inerter stores the energy rather than dissipating energy, it can not directly increase the amount of dissipated energy but can help modify the dynamic behaviour of dampers to dissipate more energy.

Additionally, the inerter-based vibration suppression devices brought benefits when considering the system stability. This was demonstrated by investigating suppression of MLG shimmy instability in Chapter 5. In this work, a beneficial spring-damper layout was proposed demonstrating its improvements in expanding the zero-shimmy region over a conventional shimmy damper. The inclusion of inerter into this proposed layout further expanded the zero-shimmy region, which suggested that inerter-based shimmy-suppression devices was more robust to the variations of operational and device design parameters. However, it was also shown the extent of performance advantages was determined by achievable inertance, which was limited by the feasible size and weight of the device in nature.

7.2 Future work

To move towards real-life applications, it is suggested that the future focus should be on making the techniques more applicable in an industrial setting.

7.2.1 Model extensions

For each vibration suppression case, simplified models were used to demonstrate the effectiveness of the proposed design methodologies. It is interesting and useful to take into consideration un-modelled dynamics, to examine the sensitivity of device performances to them, and then extend the system models considering the most significant factors.

With regards to the shimmy problem, whilst the reduced-order parametric MLG model used in Chapter 5 has considered some key effects, there are other un-modelled features. For example, the aircraft weight variation, the axial deflection of the shock strut and the freeplay also influence the system dynamics as well as the function of the shimmy-suppression device. The challenge here is to identify to what extent these features affect the system behaviour and how robust the shimmy-suppression device is to them. Since the method proposed here is applicable to alternative system parameter settings, one could conduct sensitivity analyses of the MLG stability to the variation of the un-modelled effects. The identified key features can then be fed into the design models.

Whilst the engine mount model used in Chapter 6 follows previous studies and adopted commonly used simplifications, there are also some un-modelled factors worth to be considered, such as the nonlinear rubber properties which highly depended on the frequencies and amplitudes of excitations [167]. The pressure-flow relationship in the fluid passageway is also nonlinear which will vary with the flow conditions, laminar or turbulent. Another important un-modelled aspect is fluid-structure interaction since the engine mount is a interdisciplinary device and two domains are influenced with each other.

Another un-modelled feature is the nonlinearity encountered in the inerter device itself. For example, the ball-screw inerter experiences the backlash, the dry friction and nonlinear compliance, which can have some impacts on their performances [78]. The impacts of such factors on the device performances need to be analysed before the devices can be exploited in an industrial setting.

7.2.2 Experimental validation and physical implementation

The work presented in this thesis were simulation studies. To facilitate the practical industry use of the proposed beneficial designs, it is necessary to experimentally verify their performance advantages. Prototypes need to be built, tested and adjusted considering the inherent characteristics present in the devices. For example, the theoretical advantages of beneficial engine mount designs introduced in Chapter 6 also need to be validated experimentally. The key system parameters, such as the rubber and fluid passageway properties, need to be identified experimentally.

For the prototype development, one needs to consider physical implementations for specific real-life industrial applications. For example, to realise certain inertance, flywheel-based realisations have already been adopted and experimentally tested [1, 76]. However, after certain operation cycles, such mechanisms may experience excessive wear which may lead to poor system performances. To overcome this, alternative fluid-based realisations or rubber-hydraulic devices have been proposed [81, 2, 85] but these introduce additional nonlinear behaviour.

References

[1] C. Papageorgiou, N. E. Houghton, and M. C. Smith, "Experimental testing and analysis of inerter devices," *Journal of Dynamic Systems, Measurement, and Control*, vol. 131, no. 1, p. 011001, 2009.

[2] X. Liu, J. Z. Jiang, B. Titurus, and A. Harrison, "Model identification methodology for fluid-based inerters," *Mechanical Systems and Signal Processing*, vol. 106, pp. 479–494, 2018.

[3] F.-C. Wang, C.-W. Chen, M.-K. Liao, and M.-F. Hong, "Performance analyses of building suspension control with inerters," in *46th IEEE Conference on Decision and Control*, pp. 3786–3791, IEEE, 2007.

[4] K. Ikago, K. Saito, and N. Inoue, "Seismic control of single-degree-of-freedom structure using tuned viscous mass damper," *Earthquake Engineering and Structural Dynamics*, vol. 41, no. 3, pp. 453–474, 2012.

[5] I. F. Lazar, S. A. Neild, and D. J. Wagg, "Using an inerter-based device for structural vibration suppression," *Earthquake Engineering and Structural Dynamics*, vol. 43, no. 8, pp. 1129–1147, 2014.

[6] R. Van der Valk and H. B. Pacejka, "An analysis of a civil aircraft main gear shimmy failure," *Vehicle System Dynamics*, vol. 22, no. 2, pp. 97–121, 1993.

[7] B. Milwitzky and F. E. Cook, "Analysis of landing-gear behavior," Tech. Rep. 1154, NACA, 1953.

[8] A. Geisberger, A. Khajepour, and F. Golnaraghi, "Non-linear modelling of hydraulic mounts: Theory and experiment," *Journal of Sound and Vibration*, vol. 249, no. 2, pp. 371–397, 2002.

[9] D. J. Inman, *Engineering vibration*, vol. 3. Prentice Hall New Jersey, 2008.

[10] D. J. Inman, *Vibration with control*. John Wiley & Sons, 2017.

[11] R. E. D. Bmop, A. G. Parkinson, and J. W. Pendered, "Linear analysis of transient vibration," *Journal of Sound and Vibration*, vol. 9, no. 2, pp. 313–337, 1969.

[12] S. S. Rao and F. F. Yap, *Mechanical vibrations*, vol. 4. Prentice Hall Upper Saddle River, 2011.

[13] H. P. Y. Hitch, "Aircraft ground dynamics," *Vehicle System Dynamics*, vol. 10, no. 4-5, pp. 319–332, 1981.

[14] N. S. Currey, *Aircraft landing gear design: principles and practices*. AIAA Education Series, Washington, 1988.

[15] D. W. Young, "Aircraft landing gears—the past, present and future," *Proceedings of the Institution of Mechanical Engineers, Part D: Transport Engineering*, vol. 200, no. 2, pp. 75–92, 1986.

[16] J. H. Walls, "Investigation of the air-compression process during drop tests of an oleo-pneumatic landing gear," Tech. Rep. TN 2477, NACA, 1951.

[17] J. H. Walls, "An experimental study of orifice coefficients, internal strut pressures, and loads on a small oleo-pneumatic shock strut," Tech. Rep. TN 3426, NACA, 1955.

[18] B. Milwitzky and F. E. Cook, "Effect of interaction on landing-gear behavior and dynamic loads in a flexible airplane structure," Tech. Rep. 1278, NACA, 1955.

[19] M. R. Svinkin, "Predicting soil and structure vibrations from impact machines," *Journal of Geotechnical and Geoenvironmental Engineering*, vol. 128, no. 7, pp. 602–612, 2002.

[20] T. P. Waters, Y. Hyun, and M. J. Brennan, "The effect of dual-rate suspension damping on vehicle response to transient road inputs," *Journal of Vibration and Acoustics*, vol. 131, no. 1, p. 011004, 2009.

[21] J. N. Yang and W. J. Trapp, "Reliability analysis of aircraft structures under random loading and periodic inspection," *AIAA Journal*, vol. 12, no. 12, pp. 1623–1630, 1974.

[22] H. Haddad Khodaparast, G. Georgiou, J. Cooper, L. Riccobene, S. Ricci, G. Vio, and P. Denner, "Efficient worst case 1-cosine gust loads prediction," *Journal of Aeroelasticity and Structural Dynamics*, vol. 2, no. 3, 2012.

[23] J. S. Rao and R. V. Dukkipati, *Mechanism and machine theory*.

[24] M. Klasztorny, "Reduction of steady-state forced vibrations of structures with dynamic absorbers," *Earthquake Engineering and Structural dynamics*, vol. 24, no. 8, pp. 1155–1172, 1995.

[25] D. J. P. Hartog, *Mechanical vibrations*. McGraw-Hill Book Company, 1956.

[26] Y. Yu, N. G. Naganathan, and R. V. Dukkipati, "A literature review of automotive vehicle engine mounting systems," *Mechanism and Machine Theory*, vol. 36, no. 1, pp. 123–142, 2001.

[27] M. S. Foumani, A. Khajepour, and M. Durali, "A new high-performance adaptive engine mount," *Modal Analysis*, vol. 10, no. 1, pp. 39–54, 2004.

[28] R. S. Barbosa, "Vehicle dynamic response due to pavement roughness," *Journal of the Brazilian Society of Mechanical Sciences and Engineering*, vol. 33, no. 3, pp. 302–307, 2011.

[29] J. Van Der Tempel, *Design of support structures for offshore wind turbines*. PhD thesis, TU Delft, Delft University of Technology, 2006.

[30] A. A. Andronov and S. E. Khajkin, *Theory of oscillations*. Princeton University Press, 1949.

[31] L. Librescu and P. Marzocca, "Advances in the linear/nonlinear control of aeroelastic structural systems," *Acta Mechanica*, vol. 178, no. 3-4, pp. 147–186, 2005.

[32] V. Anishchenko, T. Vadivasova, and G. Strelkova, "Stochastic self-sustained oscillations of non-autonomous systems," *The European Physical Journal Special Topics*, vol. 187, no. 1, pp. 109–125, 2010.

[33] D. H. Hodges and G. A. Pierce, *Introduction to structural dynamics and aeroelasticity*, vol. 15. Cambridge University Press, 2011.

[34] E. Dowell, J. Edwards, and T. Strganac, "Nonlinear aeroelasticity," *Journal of Aircraft*, vol. 40, no. 5, pp. 857–874, 2003.

[35] D. S. Woolston, H. L. Runyan, and T. A. Byrdsong, "Some effects of system nonlinearities in the problem of aircraft flutter," Tech. Rep. 3539, NACA, 1955.

[36] P. J. Holmes, "Bifurcations to divergence and flutter in flow-induced oscillations: a finite dimensional analysis," *Journal of Sound and Vibration*, vol. 53, no. 4, pp. 471–503, 1977.

[37] P. Marzocca, L. Librescu, and W. A. Silva, "Flutter, postflutter, and control of a supersonic wing section," *Journal of Guidance, Control, and Dynamics*, vol. 25, no. 5, pp. 962–970, 2002.

[38] K. Y. Billah and R. H. Scanlan, "Resonance, tacoma narrows bridge failure, and undergraduate physics textbooks," *American Journal of Physics*, vol. 59, no. 2, pp. 118–124, 1991.

[39] D. S. Whitehead, "Effect of mistuning on the vibration of turbo-machine blades induced by wakes," *Journal of Mechanical Engineering Science*, vol. 8, no. 1, pp. 15–21, 1966.

[40] M. P. Paidoussis and F. C. Moon, "Nonlinear and chaotic fluidelastic vibrations of a flexible pipe conveying fluid," *Journal of Fluids and Structures*, vol. 2, no. 6, pp. 567–591, 1988.

[41] G. Broulhiet, "The suspension of the automobile steering mechanism: Shimmy and tramp," *Bulletin of Society of Civil Engineers*, vol. 78, pp. 540–554, 1925.

[42] H. Fromm, "Brief report on the history of the theory of shimmy," Tech. Rep. TM-1365, NACA, 1954.

[43] J. Glaser and G. Hrycko, "Landing gear shimmy–de havilland's experience," in *81st Meeting of the AGARD Structures and Materials Panel*, 1995.

[44] I. J. M. Besselink, *Shimmy of aircraft main landing gears*. PhD thesis, TU Delft, Delft University of Technology, 2000.

[45] H. E. Merritt, "Theory of self-excited machine-tool chatter: contribution to machine-tool chatter research," *Journal of Engineering for Industry*, vol. 87, no. 4, pp. 447–454, 1965.

[46] M. Wiercigroch, "Chaotic vibration of a simple model of the machine tool-cutting process system," *Journal of Vibration and Acoustics*, vol. 119, no. 3, pp. 468–475, 1997.

[47] N. H. Hanna and S. A. Tobias, "A theory of nonlinear regenerative chatter," *Journal of Engineering for industry*, vol. 96, no. 1, pp. 247–255, 1974.

[48] J. Tlusty, "The stability of machine tools against self-excited vibrations in machining," *International Research in Production Engineering*, 1963.

[49] G. Quintana and J. Ciurana, "Chatter in machining processes: A review," *International Journal of Machine Tools and Manufacture*, vol. 51, no. 5, pp. 363–376, 2011.

[50] H. Frahm, "Device for damping vibrations of bodies," Apr. 18 1911. US Patent 989,958.

[51] F. Sadek, B. Mohraz, A. W. Taylor, and R. M. Chung, "A method of estimating the parameters of tuned mass dampers for seismic applications," *Earthquake Engineering and Structural Dynamics*, vol. 26, no. 6, pp. 617–636, 1997.

[52] N. Hoang and P. Warnitchai, "Design of multiple tuned mass dampers by using a numerical optimizer," *Earthquake Engineering and Structural Dynamics*, vol. 34, no. 2, pp. 125–144, 2005.

[53] S. Elias, V. Matsagar, and T. Datta, "Effectiveness of distributed tuned mass dampers for multi-mode control of chimney under earthquakes," *Engineering Structures*, vol. 124, pp. 1–16, 2016.

[54] T. T. Soong and M. C. Costantinou, *Passive and active structural vibration control in civil engineering*, vol. 345. Springer, 1994.

[55] X. M. Wang and U. Carl, "Fuzzy control of aircraft semi-active landing gear system," in *AIAA 37th Aerospace Sciences Meeting and Exhibit*, pp. 1–11, 1999.

[56] S. F. N. Jenkins, "Landing gear design and development," *Proceedings of the Institution of Mechanical Engineers, Part G: Journal of Aerospace Engineering*, vol. 203, no. 1, pp. 67–73, 1989.

[57] K. Seto, K. Sawatari, A. Nagamatsu, M. Ishihama, and K. Doi, "Optimum design method for hydraulic engine mounts," *SAE Technical Paper*, 1991.

[58] Y. K. Ahn, Y. C. Kim, B. S. Yang, M. Ahmadian, K. K. Ahn, and S. Morishita, "Optimal design of an engine mount using an enhanced genetic algorithm with simplex method," *Vehicle System Dynamics*, vol. 43, no. 1, pp. 57–81, 2005.

[59] J. Christopherson and G. N. Jazar, "Optimisation of classical hydraulic engine mounts based on rms method," *Shock and Vibration*, vol. 12, no. 2, pp. 119–147, 2005.

[60] F. Yi and S. J. Dyke, "Structural control systems: performance assessment," in *American Control Conference*, vol. 1, pp. 14–18, IEEE, 2000.

[61] N. Jalili, "A comparative study and analysis of semi-active vibration-control systems," *Journal of Vibration and Acoustics*, vol. 124, no. 4, pp. 593–605, 2002.

[62] W. E. Howell, J. R. Mcgehee, R. H. Daugherty, and W. A. Vogler, "F-106B airplane active control landing gear drop test performance," Tech. Rep. TM 102741, NASA, 1990.

[63] L. G. Horta, R. H. Daugherty, and V. J. Martinson, "Modeling and validation of a navy a6-intruder actively controlled landing gear system," Tech. Rep. TP 209124, NASA, 1999.

[64] G. Pouly, T.-H. Huynh, J.-P. Lauffenburger, and M. Basset, "Indirect fuzzy adaptive control for active shimmy damping," *IFAC Proceedings Volumes*, vol. 41, no. 2, pp. 15058–15063, 2008.

[65] H. Tourajizadeh and S. Zare, "Robust and optimal control of shimmy vibration in aircraft nose landing gear," *Aerospace Science and Technology*, vol. 50, pp. 1–14, 2016.

[66] Y.-W. Lee and C.-W. Lee, "Dynamic analysis and control of an active engine mount system," *Proceedings of the Institution of Mechanical Engineers, Part D: Journal of Automobile Engineering*, vol. 216, no. 11, pp. 921–931, 2002.

[67] M. D. Symans and M. C. Constantinou, "Semi-active control systems for seismic protection of structures: A state-of-the-art review," *Engineering Structures*, vol. 21, no. 6, pp. 469–487, 1999.

[68] D. Karnopp, M. J. Crosby, and R. Harwood, "Vibration control using semi-active force generators," *Journal of Engineering for Industry*, vol. 96, no. 2, pp. 619–626, 1974.

[69] W. Krüger, "Design and simulation of semi-active landing gears for transport aircraft," *Mechanics of Structures and Machines*, vol. 30, no. 4, pp. 493–526, 2002.

[70] Y.-T. Choi and N. M. Wereley, "Vibration control of a landing gear system featuring electrorheological/magnetorheological fluids," *Journal of Aircraft*, vol. 40, no. 3, pp. 432–439, 2003.

[71] D.-E. Chen, H.-B. Gu, and H. Wu, "Application of magneto-rheological damper in landing gear shimmy," in *3rd International Symposium on Systems and Control in Aeronautics and Astronautics (ISSCAA)*, pp. 1212–1216, IEEE, 2010.

[72] T. Q. Truong and K. K. Ahn, "A new type of semi-active hydraulic engine mount using controllable area of inertia track," *Journal of Sound and Vibration*, vol. 329, no. 3, pp. 247–260, 2010.

[73] M. Wang, G.-F. Yao, J.-Z. Zhao, and M. Qin, "A novel design of semi-active hydraulic mount with wide-band tunable notch frequency," *Journal of Sound and Vibration*, vol. 333, no. 8, pp. 2196–2211, 2014.

[74] M. C. Smith, "Synthesis of mechanical networks: The inerter," *IEEE Transactions on Automatic Control*, vol. 47, no. 10, pp. 1648–1662, 2002.

[75] F. A. Firestone, "A new analogy between mechanical and electrical systems," *The Journal of the Acoustical Society of America*, vol. 4, no. 3, pp. 249–267, 1933.

[76] C. Papageorgiou and M. C. Smith, "Laboratory experimental testing of inerters," in *44th IEEE Conference on Decision and Control and the European Control Conference*, pp. 3351–3356, IEEE, 2005.

[77] J.-M. Nie, X.-L. Zhang, H.-B. Jiang, and L. Chen, "Research on the inerter structure," *Machine Design and Research*, vol. 28, no. 1, pp. 29–32, 2012.

[78] A. Gonzalez Buelga, I. F. Lazar, J. Z. Jiang, S. A. Neild, and D. J. Inman, "Assessing the effect of nonlinearities on the performance of a tuned inerter damper," *Structural Control and Health Monitoring*, vol. 24, no. 3, 2017.

[79] F.-C. Wang and W.-J. Su, "Impact of inerter nonlinearities on vehicle suspension control," *Vehicle System Dynamics*, vol. 46, no. 7, pp. 575–595, 2008.

[80] F.-C. Wang, M.-F. Hong, and T.-C. Lin, "Designing and testing a hydraulic inerter," *Proceedings of the Institution of Mechanical Engineers, Part C: Journal of Mechanical Engineering Science*, vol. 225, no. 1, pp. 66–72, 2011.

[81] S. J. Swift, M. C. Smith, A. R. Glover, C. Papageorgiou, B. Gartner, and N. E. Houghton, "Design and modelling of a fluid inerter," *International Journal of Control*, vol. 86, no. 11, pp. 2035–2051, 2013.

[82] A. Ogawa and K. Adachi, "Theoretical analysis of a novel planetary gear type inerter for the torsional vibration suppression capability of automotive drive train system," in *ASME 2017 International Mechanical Engineering Congress and Exposition*, pp. V013T01A001–V013T01A001, American Society of Mechanical Engineers, 2017.

[83] J. L. Shearer, A. T. Murphy, and H. H. Richardson, *Introduction to system dynamics*, vol. 7017. Addison-Wesley Reading, 1967.

[84] A. Geisberger, A. Khajepour, and F. Golnaraghi, "Non-linear modelling of hydraulic mounts: Theory and experiment," *Journal of Sound and vibration*, vol. 249, no. 2, pp. 371–397, 2002.

[85] T. Chai, J. T. Dreyer, and R. Singh, "Frequency domain properties of hydraulic bushing with long and short passages: System identification using theory and experiment," *Mechanical Systems and Signal Processing*, vol. 56, pp. 92–108, 2015.

[86] F.-C. Wang and H.-A. Chan, "Vehicle suspensions with a mechatronic network strut," *Vehicle System Dynamics*, vol. 49, no. 5, pp. 811–830, 2011.

[87] S. Y. Zhang, J. Z. Jiang, and S. A. Neild, "Passive vibration control: A structure–immittance approach," *Proceedings of the Royal Society A*, vol. 473, no. 2201, p. 20170011, 2017.

[88] J. E. Storer, *Passive network synthesis*. McGraw-Hill, New York, 1957.

[89] M. E. Van Valkenburg, *Introduction to modern network synthesis*. Wiley, New York, 1965.

[90] R. Bott and R. Duffin, "Impedance synthesis without use of transformers," *Journal of Applied Physics*, vol. 20, no. 8, pp. 816–816, 1949.

[91] S. Evangelou, D. J. N. Limebeer, R. S. Sharp, and M. C. Smith, "Mechanical steering compensators for high-performance motorcycles," *Journal of Applied Mechanics*, vol. 74, no. 2, pp. 332–346, 2007.

[92] S. Y. Zhang, J. Z. Jiang, and S. A. Neild, "Optimal configurations for a linear vibration suppression device in a multi-storey building," *Structural Control and Health Monitoring*, vol. 24, no. 3, 2017.

[93] C. Papageorgiou and M. C. Smith, "Positive real synthesis using matrix inequalities for mechanical networks: Application to vehicle suspension," *IEEE Transactions on Control Systems Technology*, vol. 14, no. 3, pp. 423–435, 2006.

[94] F.-C. Wang, M.-K. Liao, B.-H. Liao, W.-J. Su, and H.-A. Chan, "The performance improvements of train suspension systems with mechanical networks employing inerters," *Vehicle System Dynamics*, vol. 47, no. 7, pp. 805–830, 2009.

[95] J. Z. Jiang and M. C. Smith, "Regular positive-real functions and five-element network synthesis for electrical and mechanical networks," *IEEE Transactions on Automatic Control*, vol. 56, no. 6, pp. 1275–1290, 2011.

[96] J. Z. Jiang and M. C. Smith, "Series-parallel six-element synthesis of biquadratic impedances," *IEEE Transactions on Circuits and Systems I: Regular Papers*, vol. 59, no. 11, pp. 2543–2554, 2012.

[97] J. Z. Jiang and M. C. Smith, "On the theorem of reichert," *Systems and Control Letters*, vol. 61, no. 12, pp. 1124–1131, 2012.

[98] S. Mcbeath, "Shocks to the system." Racecar Engineering, 2011.

[99] University of Cambridge, *Secrets of the inerter revealed*. http://www.cam.ac.uk/research/news/secrets-of-the-inerter-revealed.

[100] M. C. Smith and F.-C. Wang, "Performance benefits in passive vehicle suspensions employing inerters," *Vehicle System Dynamics*, vol. 42, no. 4, pp. 235–257, 2004.

[101] F. Scheibe and M. C. Smith, "Analytical solutions for optimal ride comfort and tyre grip for passive vehicle suspensions," *Vehicle System Dynamics*, vol. 47, no. 10, pp. 1229–1252, 2009.

[102] Y. Hu, M. Z. Q. Chen, and Z. Shu, "Passive vehicle suspensions employing inerters with multiple performance requirements," *Journal of Sound and Vibration*, vol. 333, no. 8, pp. 2212–2225, 2014.

[103] A. Kuznetsov, M. Mammadov, I. Sultan, and E. Hajilarov, "Optimisation of improved suspension system with inerter device of the quarter-car model in vibration analysis," *Archive of Applied Mechanics*, vol. 81, no. 10, pp. 1427–1437, 2011.

[104] Y. Shen, L. Chen, X. Yang, D. Shi, and J. Yang, "Improved design of dynamic vibration absorber by using the inerter and its application in vehicle suspension," *Journal of Sound and Vibration*, vol. 361, pp. 148–158, 2016.

[105] Y. Shen, L. Chen, Y. Liu, and X. Zhang, "Influence of fluid inerter nonlinearities on vehicle suspension performance," *Advances in Mechanical Engineering*, vol. 9, no. 11, p. 1687814017737257, 2017.

[106] F.-C. Wang, C.-H. Yu, M.-L. Chang, and M. Hsu, "The performance improvements of train suspension systems with inerters," in *45th IEEE Conference on Decision and Control*, pp. 1472–1477, IEEE, 2006.

[107] F.-C. Wang and M.-K. Liao, "The lateral stability of train suspension systems employing inerters," *Vehicle System Dynamics*, vol. 48, no. 5, pp. 619–643, 2010.

[108] J. Z. Jiang, A. Z. Matamoros-Sanchez, R. M. Goodall, and M. C. Smith, "Passive suspensions incorporating inerters for railway vehicles," *Vehicle System Dynamics*, vol. 50, no. sup1, pp. 263–276, 2012.

[109] J. Z. Jiang, A. Z. Matamoros-Sanchez, A. Zolotas, R. M. Goodall, and M. C. Smith, "Passive suspensions for ride quality improvement of two-axle railway vehicles," *Proceedings of the Institution of Mechanical Engineers, Part F: Journal of Rail and Rapid Transit*, vol. 229, no. 3, pp. 315–329, 2015.

[110] A. Z. Matamoros-Sanchez and R. M. Goodaoll, "Applications of the inerter in railway vehicle suspension," in *UKACC International Conference on Control*, pp. 555–560, IEEE, 2014.

[111] S. Evangelou, D. J. N. Limebeer, R. S. Sharp, and M. C. Smith, "Control of motorcycle steering instabilities," *IEEE Control Systems*, vol. 26, no. 5, pp. 78–88, 2006.

[112] F.-C. Wang, M.-F. Hong, and C.-W. Chen, "Building suspensions with inerters," *Proceedings of the Institution of Mechanical Engineers, Part C: Journal of Mechanical Engineering Science*, vol. 224, no. 8, pp. 1605–1616, 2010.

[113] I. Takewaki, S. Murakami, S. Yoshitomi, and M. Tsuji, "Fundamental mechanism of earthquake response reduction in building structures with inertial dampers," *Structural Control and Health Monitoring*, vol. 19, no. 6, pp. 590–608, 2012.

[114] T. Furuhashi and S. Ishimaru, "Mode control seismic design with dynamic mass," in *5th International Conference on Urban Earthquake Engineering*, 2008.

[115] K. Ikago, Y. Sugimura, K. Saito, and N. Inoue, "Modal response characteristics of a multiple-degree-of-freedom structure incorporated with tuned viscous mass dampers," *Journal of Asian Architecture and Building Engineering*, vol. 11, no. 2, pp. 375–382, 2012.

[116] L. Marian and A. Giaralis, "Optimal design of a novel tuned mass-damper-inerter (TMDI) passive vibration control configuration for stochastically support-excited structural systems," *Probabilistic Engineering Mechanics*, vol. 38, pp. 156–164, 2014.

[117] A. Giaralis and F. Petrini, "Wind-induced vibration mitigation in tall buildings using the tuned mass-damper-inerter," *Journal of Structural Engineering*, vol. 143, no. 9, p. 04017127, 2017.

[118] H. Garrido, O. Curadelli, and D. Ambrosini, "Improvement of tuned mass damper by using rotational inertia through tuned viscous mass damper," *Engineering Structures*, vol. 56, pp. 2149–2153, 2013.

[119] R. M. Hessabi and O. Mercan, "Investigations of the application of gyro-mass dampers with various types of supplemental dampers for vibration control of building structures," *Engineering Structures*, vol. 126, pp. 174–186, 2016.

[120] I. F. Lazar, S. A. Neild, and D. J. Wagg, "Vibration suppression of cables using tuned inerter dampers," *Engineering Structures*, vol. 122, pp. 62–71, 2016.

[121] J. Luo, J. H. G. Macdonald, and J. Z. Jiang, "Use of inerter-based vibration absorbers for suppressing multiple cable modes," *Procedia Engineering*, vol. 199, pp. 1695–1700, 2017.

[122] L. Sun, D. Hong, and L. Chen, "Cables interconnected with tuned inerter damper for vibration mitigation," *Engineering Structures*, vol. 151, pp. 57–67, 2017.

[123] Y. Hu and M. Z. Q. Chen, "Inerter-based passive structural control for load mitigation of wind turbines," in *29th Chinese Control And Decision Conference (CCDC)*, pp. 3056–3061, IEEE, 2017.

[124] Y. Hu and M. Z. Q. Chen, "Passive structural control with inerters for a floating offshore wind turbine," in *36th Chinese Control Conference (CCC)*, pp. 9266–9271, IEEE, 2017.

[125] N. Alujević, D. Čakmak, H. Wolf, and M. Jokić, "Passive and active vibration isolation systems using inerter," *Journal of Sound and Vibration*, vol. 418, pp. 163–183, 2018.

[126] C. P. Szczyglowski, S. Neild, B. Titurus, J. Z. Jiang, and E. Coetzee, "Passive gust load alleviation in a truss-braced wing using an inerter-based device," in *2018 AIAA/ASCE/AHS/ASC Structures, Structural Dynamics, and Materials Conference*, p. 1958, 2018.

[127] X. Dong, Y. Liu, and Z. Q. Chen, Michael, "Application of inerter to aircraft landing gear suspension," in *34th Chinese Control Conference (CCC)*, pp. 2066–2071, IEEE, 2015.

[128] Y. Liu, M. Z. Q. Chen, and Y. Tian, "Nonlinearities in landing gear model incorporating inerter," in *IEEE International Conference on Information and Automation*, pp. 696–701, IEEE, 2015.

[129] X.-J. Zhang, M. Ahmadian, and K.-H. Guo, "On the benefits of semi-active suspensions with inerters," *Shock and Vibration*, vol. 19, no. 3, pp. 257–272, 2012.

[130] M. Z. Q. Chen, Y. Hu, C. Li, and G. Chen, "Performance benefits of using inerter in semiactive suspensions," *IEEE Transactions on Control Systems Technology*, vol. 23, no. 4, pp. 1571–1577, 2015.

[131] P. Li, J. Lam, and K. C. Cheung, "Control of vehicle suspension using an adaptive inerter," *Proceedings of the Institution of Mechanical Engineers, Part D: Journal of Automobile Engineering*, vol. 229, no. 14, pp. 1934–1943, 2015.

[132] A. Z. Matamoros-Sanchez and R. M. Goodall, "Novel mechatronic solutions incorporating inerters for railway vehicle vertical secondary suspensions," *Vehicle System Dynamics*, vol. 53, no. 2, pp. 113–136, 2015.

[133] M. Zilletti, "Feedback control unit with an inerter proof-mass electrodynamic actuator," *Journal of Sound and Vibration*, vol. 369, pp. 16–28, 2016.

[134] W. Krüger, I. Besselink, D. Cowling, D. Doan, W. Kortüm, and W. Krabacher, "Aircraft landing gear dynamics: simulation and control," *Vehicle System Dynamics*, vol. 28, no. 2-3, pp. 119–158, 1997.

[135] D. J. Jones and R. A. Evans, "Compact shimmy damper for aircraft landing gear," Jan. 26 2012. US Patent App. 13/166,424.

[136] N. K. Sura, "Lateral response of nonlinear nose wheel landing gear models with torsional free-play," *Journal of Aircraft*, vol. 44, no. 6, pp. 1991–1997, 2007.

[137] N. K. Sura and S. Suryanarayan, "Lateral stability of aircraft nose-wheel landing gear with closed-loop shimmy damper," *Journal of Aircraft*, vol. 46, no. 2, pp. 505–509, 2009.

[138] F. Feng, H. Nie, M. Zhang, and Y. Peng, "Effect of torsional damping on aircraft nose landing-gear shimmy," *Journal of Aircraft*, vol. 52, no. 2, pp. 561–568, 2014.

[139] M. A. Padmanabhan and E. H. Dowell, "Landing gear design/maintenance analysis for nonlinear shimmy," *Journal of Aircraft*, vol. 52, no. 5, pp. 1707–1710, 2015.

[140] E. Atabay and I. Ozkol, "Application of a magnetorheological damper modeled using the current-dependent bouc-wen model for shimmy suppression in a torsional nose landing gear with and without freeplay," *Journal of Vibration and Control*, vol. 20, no. 11, pp. 1622–1644, 2014.

[141] R. F. Smiley, "Correlation, evaluation, and extension of linearized theories for tire motion and wheel shimmy," *NACA*, vol. 1299, 1957.

[142] G. Somieski, "Shimmy analysis of a simple aircraft nose landing gear model using different mathematical methods," *Aerospace Science and Technology*, vol. 1, no. 8, pp. 545–555, 1997.

[143] N. Terkovics, S. Neild, M. Lowenberg, and B. Krauskopf, "Bifurcation analysis of a coupled nose-landing-gear–fuselage system," *Journal of Aircraft*, vol. 51, no. 1, pp. 259–272, 2014.

[144] S. Society of Automotive Engineers, Gears and C. C. A-5B, "Landing Gear Stability," Tech. Rep. SAE AIR 4894, Aerospace Landing Gear Systems, 1995.

[145] G. Roe and T. Thorpe, "Experimental investigation of the parameters affecting the castor stability of road wheels," *Journal of Mechanical Engineering Science*, vol. 15, no. 5, pp. 365–369, 1973.

[146] C. Niu, *Airframe structural design: practical design information and data on aircraft structures*. Conmilit Press, 1988.

[147] W. Flügge and C. W. Coale, "The influence of wheel spin-up on landing-gear impact," Tech. Rep. TN 3217, NACA, 1954.

[148] D. Yadav and R. Ramamoorthy, "Nonlinear landing gear behavior at touchdown," *Journal of Dynamic Systems, Measurement, and Control*, vol. 113, no. 4, pp. 677–683, 1991.

[149] P. Woerner and O. Noel, "Influence of nonlinearity on the shimmy behaviour of landing gear," in *81st Meeting of the AGARD Structures and Materials Panel*, 1995.

[150] L. Segel, "Force and moment response of pneumatic tires to lateral motion inputs," *Journal of Engineering for Industry*, vol. 88, no. 1, pp. 37–44, 1966.

[151] B. Von Schlippe and R. Dietrich, "Shimmying of a pneumatic wheel," Tech. Rep. TM-1365, NACA, 1954.

[152] P. Thota, B. Krauskopf, and M. Lowenberg, "Shimmy in a nonlinear model of an aircraft nose landing gear with non-zero rake angle," in *Proceedings of the 6th European Mechanics Society Nonlinear Dynamics Conference*, European Mechanics Society, 2008.

[153] P. Thota, B. Krauskopf, and M. Lowenberg, "Interaction of torsion and lateral bending in aircraft nose landing gear shimmy," *Nonlinear Dynamics*, vol. 57, no. 3, pp. 455–467, 2009.

[154] M. Goman, G. Zagainov, and A. Khramtsovsky, "Application of bifurcation methods to nonlinear flight dynamics problems," *Progress in Aerospace Sciences*, vol. 33, no. 9, pp. 539–586, 1997.

[155] S. Sharma, E. B. Coetzee, M. H. Lowenberg, S. A. Neild, and B. Krauskopf, "Numerical continuation and bifurcation analysis in aircraft design: an industrial perspective," *Phil. Trans. R. Soc. A*, vol. 373, no. 2051, p. 20140406, 2015.

[156] C. Howcroft, B. Krauskopf, M. H. Lowenberg, and S. A. Neild, "Influence of variable side-stay geometry on the shimmy dynamics of an aircraft dual-wheel main landing gear," *SIAM Journal on Applied Dynamical Systems*, vol. 12, no. 3, pp. 1181–1209, 2013.

[157] P. Eret, J. Kennedy, and G. J. Bennett, "Effect of noise reducing components on nose landing gear stability for a mid-size aircraft coupled with vortex shedding and freeplay," *Journal of Sound and Vibration*, vol. 354, pp. 91–103, 2015.

[158] J. T. Gordon and H. E. Merchant, "An asymptotic method for predicting amplitudes of nonlinear wheel shimmy," *Journal of Aircraft*, vol. 15, no. 3, pp. 155–159, 1978.

[159] J. Zhou and L. Zhang, "Incremental harmonic balance method for predicting amplitudes of a multi-dof non-linear wheel shimmy system with combined coulomb and quadratic damping," *Journal of Sound and Vibration*, vol. 279, no. 1, pp. 403–416, 2005.

[160] E. Doedel, H. B. Keller, and J. P. Kernevez, "Numerical analysis and control of bifurcation problems (i): bifurcation in finite dimensions," *International journal of bifurcation and chaos*, vol. 1, no. 03, pp. 493–520, 1991.

[161] E. Coetzee, B. Krauskopf, and M. Lowenberg, "The dynamical systems toolbox: Integrating auto into matlab," in *Proceedings of the 16th US National Congress of Theoretical and Applied Mechanics*, 2010.

[162] R. H. Daughterty, *A study of the mechanical properties of modern radial aircraft tires*. Citeseer, 2003.

[163] D. Takács and G. Stépán, "Experiments on quasiperiodic wheel shimmy," *Journal of Computational and Nonlinear Dynamics*, vol. 4, no. 3, p. 031007, 2009.

[164] D. Takács, *Dynamics of towed wheels: nonlinear theory and experiments*. PhD thesis, 2010.

[165] Y. A. Kuznetsov, *Elements of applied bifurcation theory*, vol. 112. Springer Science & Business Media, 2013.

[166] R. Singh, G. Kim, and P. Ravindra, "Linear analysis of automotive hydro-mechanical mount with emphasis on decoupler characteristics," *Journal of Sound and Vibration*, vol. 158, no. 2, pp. 219–243, 1992.

[167] G. Kim and R. Singh, "A study of passive and adaptive hydraulic engine mount systems with emphasis on non-linear characteristics," *Journal of Sound and Vibration*, vol. 179, no. 3, pp. 427–453, 1995.

[168] P. E. Corcoran and G. H. Ticks, "Hydraulic engine mount characteristics," Tech. Rep. 840407, SAE, 1984.

[169] G. Kim and R. Singh, "High-frequency performance characteristics of a passive hydraulic engine mount," in *Proceedings of SPIE*, pp. 1281–1281, 11th International Modal Analysis Conference, Florida, 1993.

[170] J. Colgate, C. Chang, Y. Chiou, W. Liu, and L. Keer, "Modelling of a hydraulic engine mount focusing on response to sinusoidal and composite excitations," *Journal of Sound and Vibration*, vol. 184, no. 3, pp. 503–528, 1995.

[171] M. Tiwari, H. Adiguna, and R. Singh, "Experimental characterization of a nonlinear hydraulic engine mount," *Noise Control Engineering Journal*, vol. 51, no. 1, pp. 36–49, 2003.

[172] G. Kim and R. Singh, "Nonlinear analysis of automotive hydraulic engine mount," *Journal of Dynamic Systems, Measurement, and Control*, vol. 115, no. 3, pp. 482–487, 1993.

[173] H. Adiguna, M. Tiwari, R. Singh, H. Tseng, and D. Hrovat, "Transient response of a hydraulic engine mount," *Journal of Sound and Vibration*, vol. 268, no. 2, pp. 217–248, 2003.

[174] A. Ohadi and V. Fakhari, "Effect of bell plate on vibration behavior of automotive engine supported by hydraulic engine mounts," Tech. Rep. 2007-01-2364, SAE, 2007.

[175] J. Christopherson, M. Mahinfalah, and R. N. Jazar, "Suspended decoupler: A new design of hydraulic engine mount," *Journal of Advance in Acoustics and Vibration*, vol. 2012, 2011.

[176] Y. Q. Zhang and W. B. Shangguan, "A novel approach for lower frequency performance design of hydraulic engine mounts," *Computers and Structures*, vol. 84, no. 8, pp. 572–584, 2006.

[177] B. Barszcz, J. T. Dreyer, and R. Singh, "Experimental study of hydraulic engine mounts using multiple inertia tracks and orifices: Narrow and broad band tuning concepts," *Journal of Sound and Vibration*, vol. 331, no. 24, pp. 5209–5223, 2012.

[178] T. Chai, J. T. Dreyer, and R. Singh, "Time domain responses of hydraulic bushing with two flow passages," *Journal of Sound and Vibration*, vol. 333, no. 3, pp. 693–710, 2014.

[179] T. Chai, J. T. Dreyer, and R. Singh, "Nonlinear dynamic properties of hydraulic suspension bushing with emphasis on the flow passage characteristics," *Proceedings of the Institution of Mechanical Engineers, Part D: Journal of Automobile Engineering*, vol. 229, no. 10, pp. 1327–1344, 2015.

[180] J. Riordan and C. E. Shannon, "The number of two-terminal series-parallel networks," *Studies in Applied Mathematics*, vol. 21, no. 1-4, pp. 83–93, 1942.

[181] R. W. Fox, A. T. McDonald, and P. J. Pritchard, *Introduction to fluid mechanics*, vol. 5. John Wiley & Sons New York, 1998.

[182] H. S. Bean, *Fluid meters: Their theory and application*, vol. 2. American Society of Mechanical Engineers, 1971.

[183] R. Fan and Z. Lu, "Fixed points on the nonlinear dynamic properties of hydraulic engine mounts and parameter identification method: experiment and theory," *Journal of Sound and Vibration*, vol. 305, no. 4-5, pp. 703–727, 2007.